THE NEW CONCEPT OF GRACE GRADIOMETRY AND THE UNRAVELLING OF THE MYSTERY OF STRIPES

ATHINA PEIDOU

A DISSERTATION SUBMITTED TO
THE FACULTY OF GRADUATE STUDIES
IN PARTIAL FULFILLMENT OF THE REQUIREMENTS FOR THE DEGREE OF

DOCTOR OF PHILOSOPHY

GRADUATE PROGRAM IN EARTH AND SPACE SCIENCE
YORK UNIVERSITY
TORONTO, ONTARIO

March 2020

Abstract

For nearly two decades, the Gravity Recovery and Climate Experiment (GRACE) and GRACE-Follow On (GRACE-FO) missions have been widely used to quantify mass transfers within the Earth.

We perform analysis on the on-board measurements, and we find an interesting correlation between space weather dynamics and disturbances of the on-board measurements. An innovative idea for bringing the two GRACE spacecraft into a differential mode is introduced to fully capture the impact of charged particles on the instrumentation. The idea of differential mode is advanced to a method named ‘gradiometer mode’ that leads to the estimation of gravitational gradients using GRACE Level 1B measurements. GRACE gradiometer mode is shown to be able to capture geophysical signals at multiscale resolution between [8, 128] spherical harmonics.

Both GRACE and GRACE-FO suffer from a disturbing artifact, commonly known as “longitudinal stripes”, whose origin is yet to be determined. The presence of stripes in GRACE gravity models conceals geophysical signals and degrades the capability of the mission to quantify smaller scale mass transfers (< 200 km). In an effort to discover the origin of stripes, we scrutinize the mission’s instrumentation, twin-spacecraft configuration and orbital characteristics, to conclude that the GRACE spatial sampling pattern is responsible for the stripe artifacts.

GRACE sampling characteristics are quantified and used to prove that the stripes are sub-Nyquist (pseudo-moiré) artifacts. We show that the stripes are the result of oversampling the low frequency geoid along the east-west (latitudinal) direction. The low-frequency geoid modulates the total sampled gravitational signal with a frequency near $\frac{m}{n} f_s$, where f_s is the sampling frequency of the GRACE ground track ‘bundles’ along the parallels, and *m* and *n* are mutually prime integers, with $2m \leq n$. GRACE effective latitudinal sampling frequency is shown to be $\Delta_s = 1.14^{\circ}$. We generate synthetic stripes using moiré theory and by means of rigorous spectral analysis, it is shown that their spectral and spatial characteristics are very similar to the observed ones.

Dedication

τὸ θαυμάζειν: οὐ γὰρ ἄλλη ἀρχὴ φιλοσοφίας ἢ αὕτη […]

ἡ μὲν γὰρ τούτου γνῶσις σοφία καὶ ἀρετὴ ἀληθινή, ἡ δὲ ἄγνοια ἀμαθία καὶ κακία ἐναργής

Σωκράτης, Θεαίτητος, 369 π.Χ.

philosophy begins in wonder […]

For to know this is true wisdom and virtue, and ignorance of this is manifest folly and vice

Socrates, Theatetus, ca 369 BC

Translated by Benjamin Jowett (1871)

Στήν γιαγιά μου Περιστέρα Πεΐδου

στόν θεῖο μου Παῦλο Μανουσαρίδη

καί στήν προγιαγιά μου Μαρία (Μίκρη) Ἀθανασιάδου-Πεΐδου

Acknowledgments

Concluding a delightful research odyssey, it is a great pleasure to have the opportunity to thank those who made my journey unforgettable.

First and foremost, I am deeply thankful to my supervisor, Dr. Spiros Pagiatakis, whose role in my academic journey is nonesuch. He is a rare type of mentor, an authentic daskalos, defined by the virtues of passion, humbleness, diligence, patience, delicacy, inspiration, fairness, respect and openness. Thank you, Spiros, for believing in me from the first moment we took this journey. Thank you for sharing with me your passion for research. Although you ruffled my feathers with our endless late evening discussions, I am so grateful for all the research challenges we shared. I will be always indebted for the verbal and non-verbal lessons you gave me. The projection of your example in research and teaching on me, will always benefit and guide me. Thank you for being my daskalos and my friend. It was an honor and a lifechanging experience to collaborate with you.

I am deeply grateful to Dr. Sunil Bisnath, for his encouraging and critical feedback, for always posing the right questions and for the many discussions we shared all these years. Many thank you to Dr. Mike Daly, whose suggestions and constructive feedback were always very helpful. George Vukovich is also thanked for his contributions to this research and above all for always being an example of humbleness. Thank you to Dr. Matthew Kyan and Dr. Mark Gordon for their great feedback while reviewing this thesis. Thank you, Dr. Michael Sideris, for the very useful and thoughtful comments. I am also grateful to Dr. Frank Flecthner and Dr. Srinivas Bettadpur for the many useful discussions. Special thanks to my teachers from the Aristotle University of Thessaloniki who taught me the core concepts of geodesy and inspired my scientific steps.

My peers, past and current from the Space Geodesy Laboratory are thanked for making the work environment a memorable experience. A deep thank you to my dear friend, Sinem Ince, for the research discussions we shared and for her friendship. My good friend Panagiotis Vergados is also thanked for his support and encouragement in the final stages of this research. Thank you to Kristen Cote and to Patrick, Evangelos and Myrto for being a wonderful company.

Special thanks to my Canadian Rockies, Glykeria Martou, Tasos Papalazarou, Effie Karageorgos and Myrto Piperidou. Thank you also to Judith Elliott and Katie Irwin for being good friends all these years. Thank you, Katerina and Christina Pagiatakis for being great friends, though miles away. Thank you, Ms. Roula, for all the funny moments we shared and for your motherly caring all these years.

Thank you to my dear friend, Alex Harvey, for being a great constant and a precious friend. You were always there for me since my very first days in Canada. Thank you to John Orfanides for the amazing times we spent in Boston throughout these years. My littles, Kosmas and Konstantinos, added a note of joy in my life and cheered up my days with their smiles.

Thank you to Ioulia and Afroditi for always believing in me, supporting me and inspiring me. Your guidance and patience led me to achieve goals that surpassed my potentials. I can't thank you enough for all the things you have done for me and for believing in me even when I did not believe in myself. Thank you, Katerina, for your endless care, support and patience and for being a great constant these past few years.

I will be always grateful to my lifelong friends Ioannis Athanasiadis, Eirini Liaptsi, Angeliki Kargopoulou, Marina Paschoula, Ioannis Vazaios and Athina Mpoumpoulentra, for their unconditional love and their constant presence in my life all these years. You made the big ocean that separates us seem like a small ditch.

This research was generously supported by Onassis Foundation, which is gratefully acknowledged. Funding support was also provided by York University and QEII Graduate Scholarships in Science and Technology, and by two grants held by my supervisor, the Natural Sciences and Engineering Research Council Discovery grant and the Lassonde Innovation Fund.

Finally, I owe my deepest thank you to my parents, Charalampos and Anna and my sister Peristera. The lessons you taught me benefited me more than you can actually perceive. Thank you for everything. My dear father you inspired in me the love for knowledge. Peristera words cannot describe your significance in my life. Above all, thank you to my mother, Anna, for her many sacrifices that have gotten me where I am today. You always inspire me for the better.

Co-Authorship

The thesis "The New Concept of GRACE Gradiometry and the Unravelling of the Mystery of Stripes" is a product of research conducted by the author, Athina Peidou. Chapter 4 and parts of Chapter 5 (Sections 5.5 and 5.6) are unabridged versions of the original research articles, *"Gravity Gradiometry with GRACE Space Missions: New opportunities for the Geosciences*" published in JGR: Solid Earth and *"Stripe mystery in GRACE geopotential models revealed"* published in Geophysical Research Letters, respectively. The published research articles are co-authored by Dr. Spiros Pagiatakis who supervised the research work and provided scientific discussion and editorial assistance.

Peidou, A. and Pagiatakis, S., 2019. Gravity Gradiometry with GRACE Space Missions: New opportunities for the Geosciences. *Journal of Geophysical Research: Solid Earth*, **124**(8), pp.9130-9147.

Peidou, A. and Pagiatakis, S., 2020. Stripe mystery in GRACE geopotential models revealed. *Geophysical Research Letters*, **47**, doi:10.1029/2019GL085497.

Contents

List of Tables

List of Figures

List of Abbreviations

ACC	Accelerometer
ACE	Advanced Composition Explorer
AOCS	Attitude and Orbit Control System
CFRP	Carbon Fiber Reinforced Plastic
CHAMP	CHAllenging Minisatellite Payload
CM	Common-Mode
CME	Coronal Mass Ejections
CoM	Center of Mass
CWT	Continuous Wavelet Transformation
DLR	Deutsche Forschungsanstalt für Luft und Raumfahrt
DM	Differential-Mode
GFZ	GeoForschungsZentrum (German Research Centre for Geosciences)
GGT	Gravity Gradient Tensor
GM	Gradiometer-Mode
GOCE	Gravity-field and steady-state Ocean Circulation Explorer
GRACE	Gravity Recovery And Climate Experiment
GRACE-FO	Gravity Recovery And Climate Experiment Follow-On
GPS	Global Positioning System
GRF	Gradiometer Reference Frame
GSE	Geocentric Solar Ecliptic
EFRF	Earth-Fixed Reference Frame
ENU	East-North-Up
EICS	Equivalent Ionospheric Currents
ESA	European Space Agency
IMF	Interplanetary Magnetic Field
IMU	Measurement Unit
ITRF	International Terrestrial Reference Frame

LEO	Low Earth Orbiter
LORF	Local Orbital Reference Frame
LOS	Line-of-sight
LRI	Laser Ranging Interferometer
LRR	Laser Retro Reflector
NASA	National Aeronautics and Space Administration
POD	Precise Orbit Determination
SECS	Spherical Elementary Current System
SH	Spherical Harmonics
SNR	Signal-Noise Ratio
SRF	Satellite Reference Frame
SST	Satellite-to-Satellite Tracking

List of Symbols

α	Parameters of the force model
$\mathbf{a}$	Non-gravitational accelerations along the three axes
$\mathbf{a}_{\boldsymbol{d}}$	Vector of differential mode accelerations
$\mathbf{a}_{\boldsymbol{c}}$	Vector of common mode accelerations
$\mathbf{B}$	Vector of Interplanetary Magnetic Field
$\mathbf{E}$	Vector of Electric field
ε	Low frequency modulating signal
$\mathrm{f_s}$	GRACE latitudinal sampling frequency
f_i	The frequency of the i-th original cosinusoidal travelling wave
G	Gravitational constant
$g(x)$	Sampled signal
θ_i	The angle between the travelling wave and the horizontal axis
K_p	Standardized K index (Geomagnetic storm index)
l	Degree of spherical harmonic coefficients
ℓ	Length of a series
Λ	Difference in the longitude between the Greenwich meridian and the longitude of the ascending node
μ	Gravitational parameter of the central body
M	The Earth's mass
m	Order of spherical harmonic coefficients
m	Number of oscillating waves within an envelope
n	Degree of spherical harmonic coefficients
n	Number of modulating envelopes in sub-Nyquist theory
P	3D position (geodetic coordinates)
$\mathbf{q}$	Quaternions (q_0, q_1, q_2, q_3)
$\boldsymbol{r}$	Position vector of the satellite
R	The Earth's mean radius

R	3 by 3 rotation matrix
σ	Standard deviation
S	Poynting vector
t	Time
u	Argument of latitude of the satellite in the orbit plane
u	Cartesian coordinate (cosine component) of the vectorial sum $\boldsymbol{f}$
v	Cartesian coordinate (sine component) of the vectorial sum $\boldsymbol{f}$
V_{xx}	Gravitational field gradient measured along the satellite track
V_{yy}	Gravitational field gradient measured cross satellite track
V_{zz}	Gravitational field gradient measured in the radial direction
V_{xy}	Gravitational field gradient measured via transversal acceleration
V_{xz}	Gravitational field gradient measured via transversal acceleration
V_{yz}	Gravitational field gradient measured via transversal acceleration

1

Introduction

1.1 Motivation and Problem Statement

The Earth is a dynamic system, constantly changing and shifting. Over the centuries, observing and modeling the Earth's parameters was usually done in a rather comprehensive way, employing various geoscience disciplines. Discussions for interdisciplinary Earth science research are well underway, and the need for new approaches for perceiving the Earth as a dynamic system has emerged.

Earth observation satellites can have a substantial contribution in connecting different geoscience disciplines, leading eventually to a deeper understanding of the Earth system. These satellites carry different sensors and instruments and usually fly in Low Earth Orbit (LEO), in order to study different areas of the geosciences.

The dynamic behaviour of the Earth system is manifested by many phenomena that occur within the Earth, one of them being the process of mass redistribution. Mass transfer events of the Earth refer to mass movements from one location and the subsequent deposition to another location. Detecting and monitoring mass transfers of hydrosphere, atmosphere, cryosphere and solid Earth created the need for a continuous measuring approach with a global coverage. At the beginning of the twenty first century, the first generation of dedicated satellite gravity missions was realized, namely the Challenging Minisatellite Payload (CHAMP) mission launched in 2000 and the Gravity Recovery and Climate Experiment (GRACE) mission launched in 2002 that mapped the Earth's dynamic gravitational field. These missions were followed by the Gravity field and steady-state Ocean Circulation Explorer (GOCE) mission, launched in 2009. Figure 1.1 displays schematically the three missions. Each mission followed different principles to recover the Earth's gravitational field and had markedly different goals. The CHAMP mission (orbit at ~450 km) was a single spacecraft mission, used to recover the first derivative of the static part of the gravity potential, i.e., the gravitational force vector; the dynamic part of the gravity field was captured by the twin-spacecraft mission GRACE (orbit at ~500 km), while GOCE (orbit at ~250 km) was yet another single spacecraft mission that measured the second derivatives of the gravity field, i.e., the gravitational gradient tensor. A detailed description of the three LEO satellite gravity missions is presented in Section 2.1.

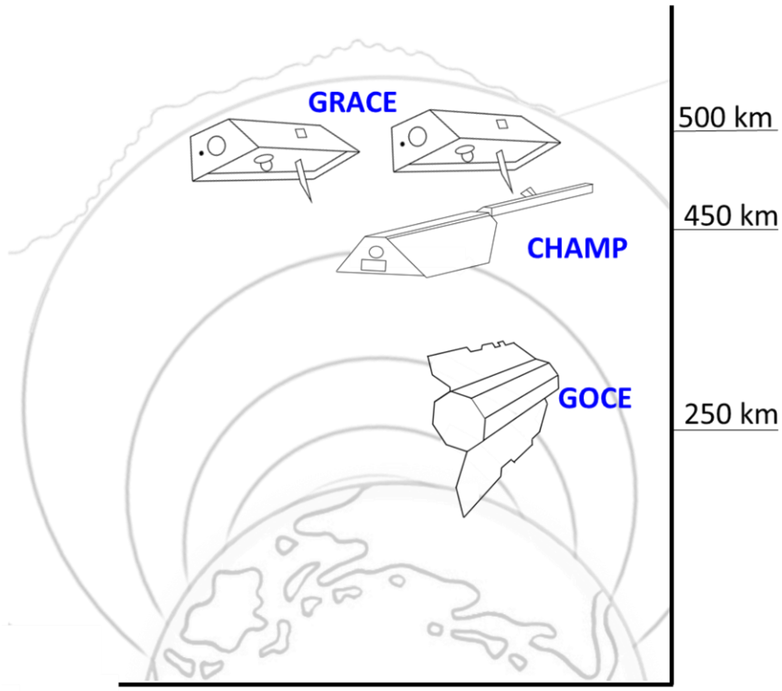

Figure 1.1: Schematic representation of the three LEO satellite gravity missions: CHAMP, GRACE and GOCE.

In this research, we focus on the GRACE mission, which was the only mission designed to map both the Earth's static and dynamic gravitational field (Tapley et al., 2004). The success of the GRACE mission (2002-2017) led to the launch of its follow-on (GRACE-FO) on May 22, 2018, with a primary goal to continue tracking the Earth's mass in motion (Flecthner et al., 2016).

The GRACE mission has been extensively studied over the last two decades, resulting in nearly 200 monthly and 60 static global gravity field models[1] and leading to thousands of original research articles that have moved us to better understanding of the Earth's mass transfer dynamics.

[1] A global gravity field model, also known as global geopotential model, is a mathematical function that describes the Earth's gravitational field in the 3D space (Barthelemes, 2014). Note that in many research articles the models are called gravity field models for simplicity, however when the centrifugal is not considered the right term to describe them is gravitational field models (Barthelemes, 2014).

However, there are still longstanding questions that need to be answered and new data processing methodologies that can be followed to expand the mission's contributions to a wider spectrum of geoscience applications.

Since the release of the first GRACE monthly models in 2002, a dominant systematic artifact, appearing as negative to positive patches, contaminated all gravity field solutions, such as gravity anomalies (see Figure 1.2). This systematic error, usually referred to as "longitudinal stripes" (Swenson and Wahr, 2006) is predominantly structured in the north-south direction, it extends globally and is observed in the shorter wavelength band of the gravity field spectrum. GRACE monthly models were initially made available up to degree and order (d/o) 120 spherical harmonic expansion[2] (translates approximately to 165 km spatial resolution at the Equator), however the impact of the stripes on these solutions was so dominant that they obscured geophysical signals (Swenson and Wahr, 2006). Though the impact of the longitudinal stripes is high, the main cause of their presence is yet to be discovered.

The primary goal of this research is rooted in the improvement of the performance of GRACE gravity field models. Hence, it is necessary to discover the origin of stripes on GRACE models and open new avenues for stripe-free models, that will eventually allow mapping of geophysical processes in higher spatial resolution and expanding the number of geoscience applications that can benefit from GRACE data.

GRACE stripes have always been considered as aliasing artifacts, partially eliminated by means of filtering either in space or frequency domain (see, e.g., Seo et al., 2008; Kusche et al., 2009). To fully capture the mechanism that drives the stripes requires a thorough analysis of all GRACE mission characteristics, from its orbit parameters and payload to data post-processing methodologies.

While investigating the performance of the instrumentation, preliminary findings revealed an interesting correlation between perturbations of GRACE on-board measurements and space weather dynamics.

---

[2] The Earth's gravity potential is usually expressed by n number of spherical harmonics. That is the degree n and the order m, define the number and the geometry (zonal, tesseral and sectorial) of the spherical harmonics that describe the Earth's potential.

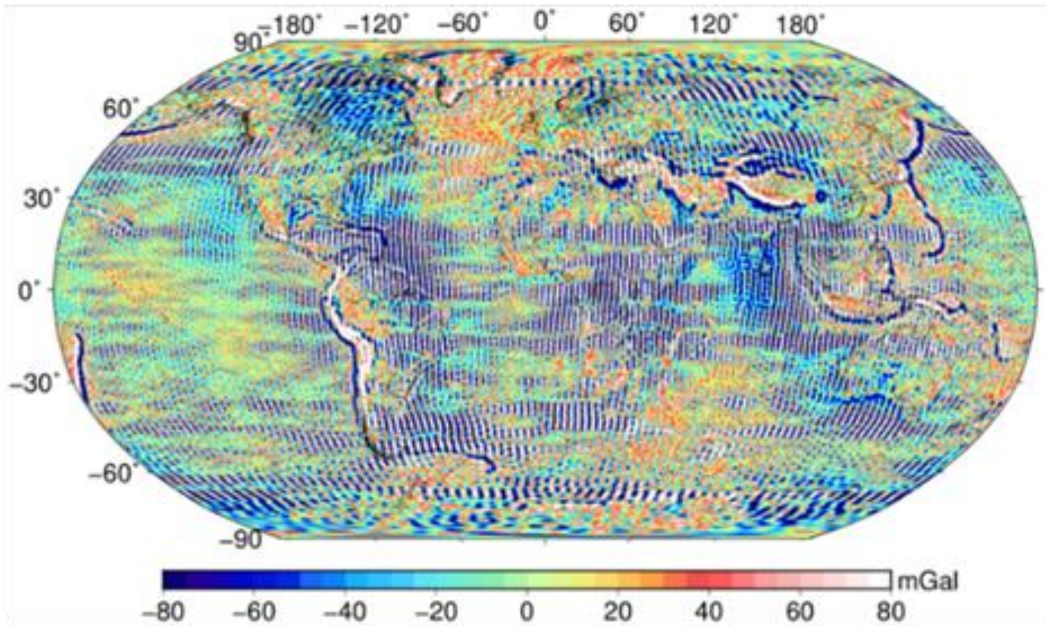

(a)

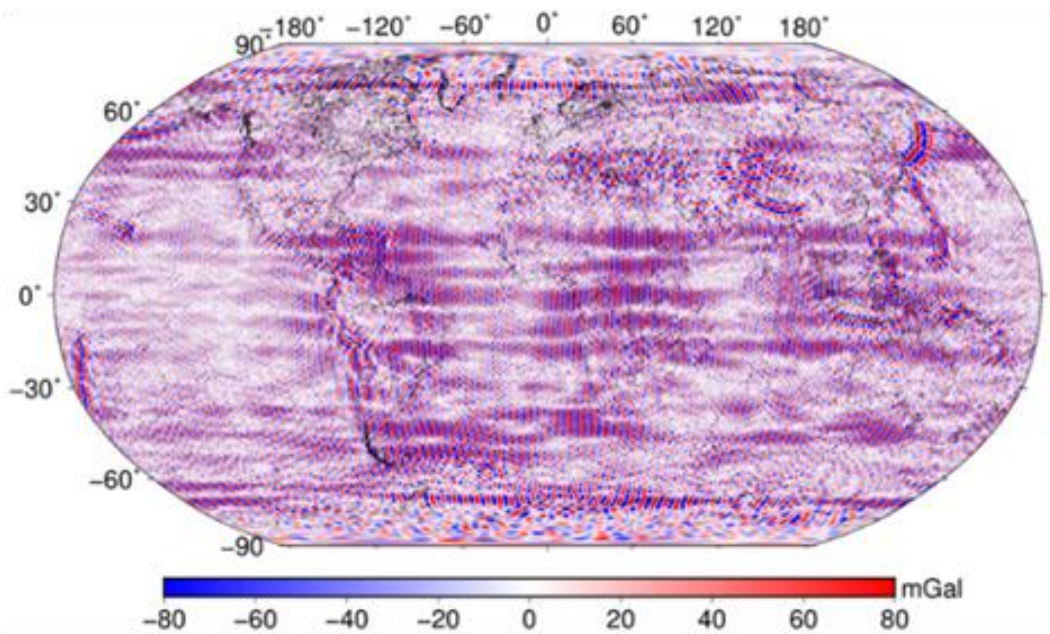

(b)

Figure 1.2: a) Gravity anomalies estimated from GRACE model GGM03s up to d/o 180 (Tapley et al., 2007). Note the negative to positive linear interchanges across the latitudes; b) Stripes on GGM03s gravity anomalies are estimated using spherical harmonic expansion between d/o 100 and 180.

LEO satellites are subject to dynamics occurring in the vicinity of the spacecraft environment, and recent studies of the GOCE mission reveal a strong connection between instrumentation disturbances and space weather dynamics (Ince and Pagiatakis, 2016; 2017). The space weather environment of the spacecraft has also been studied in the past, where focus was placed on extracting thermospheric density models and neutral wind speeds using all three dedicated satellite gravity mission measurements (Doornbos and Klinkrad, 2006; Bruinsma et al., 2006) and employing accelerometer disturbances by means of data inversion (Doornbos et al., 2008). Although GRACE is also a LEO mission and is subject to intense ionospheric dynamics due to its orbit and the lack of drag-compensation in the along axis (x-axis i.e., follows a direction from south to north), the response of GRACE to various ionospheric conditions has not yet been studied.

To fill this gap, we undertook analysis of GRACE Level 1B[3] measurements response to geomagnetic storms. Results indicate a strong match between disturbances of GRACE on-board instrumentation and magnetic field disturbances. Though disturbances in satellite motion are expected due to kinetic energy exchange between neutral particles and the spacecraft, the impact of charged particles (plasma flux) on GRACE accelerometers is yet to be assessed. To decipher the origin of the perturbations (i.e., neutral or charged particles), a new approach of processing Level 1B data was required. Interestingly, an elegant combination of Level 1B data from both GRACE satellites that puts the two-spacecraft in a 'differential mode' was created. This new data processing methodology revealed for the first time the impact of plasma flow on the accelerometer measurements.

The possibility of deriving differential accelerations using GRACE Level 1B data, opened new avenues to explore a totally innovative data processing concept: derive gravitational gradients from non-gravitational acceleration measurements and spacecraft precise orbit and attitude determination using GRACE. The GRACE mission was designed to provide the first derivatives of the Earth's gravitational field, by measuring the inter-satellite accelerations, the total acceleration from precise orbit determination and the non-gravitational accelerations. The only

[3] Level 1B: The Level 1B data consist of: SuperSTAR accelerometer, Global Positional System (GPS) Receiver Assembly, Star Camera Assembly, K-Band Ranging System (KBR), Laser Retro Reflector (LRR); and provide all the measurements required to derive monthly solutions of the Earth's gravitational field.

mission ever designed to measure gravitational gradients was GOCE, a single spacecraft mission that orbited the Earth (at almost half the GRACE altitude) at ~250 km and carried a gradiometer. GOCE's near polar orbit did not allow for covering the Earth's polar regions and provided static solutions of the gravitational field for nearly five years. In the post-GOCE era, deriving gravitational gradients from GRACE opens a wide spectrum for new geoscience applications. Keller and Sharifi (2005) attempted to estimate the gravitational gradient along the GRACE orbit, however the distance of 220 km between the two spacecraft proved not very useful for practical applications (Cassotto and Fantino, 2007; Sneeuw et al., 2008). The idea introduced in this research is conceptually different from any other suggested method, and results in the estimation of the full gravitational gradient tensor (GGT) using purely Level 1B data. The method called "GRACE Gradiometer Mode" or GRACE-GM (Peidou and Pagiatakis, 2019), has been tested over regions with known geophysical signatures and has been validated employing the GOCE mission gradiometric measurements. Some of the contributions of GRACE-GM include the detection of geophysical signals, such as the Indian depletion basin and the Juan de Fuca ridge.

Finally, focus is placed on the artifact of stripes on GRACE geopotential models. This artifact conceals geophysical signals that extend less than approximately 400 km full wavelength and deteriorate the accuracy of the final products. GRACE accuracy was originally targeted to reach up to ~2 cm on the geoid, but the presence of stripes did not allow for such a high accuracy.

With the main aim of this research being to understand the nature and the origin of disturbances that deteriorate the performance of GRACE products, we were able to explain the mechanism that drives stripes in GRACE-based models. By applying thorough analyses on the behaviour of GRACE on-board instrumentation measurements and by creating the "GRACE differential method" concept, we were provided with insights into the impact of plasma flux (charged particles) on GRACE accelerometer measurements. Advancing the idea of differential mode to GRACE-GM, led to the estimation of gravitational gradients that surprisingly did not suffer from stripes. Additionally, we noticed that stripes are present in models from other LEO missions such as Swarm and CHAMP. On the other hand, the GOCE mission provided stripe-free gradients and gravitational models. Combining GOCE's different orbit characteristics (i.e., sun-synchronous orbits), along with extensive studies of GRACE orbit resonances (Klokočník et al., 2008) and the structure of stripes that resembles moiré fringes similar to interferometric synthetic aperture radar

(InSAR) fringes, it was evident that the cause of stripes was some sort of artifact arising from the combination of orbital geometry and the way that GRACE sampled the low frequency geoid. Employing advanced sampling and moiré theories, it was shown for the first time in GRACE literature, that the stripe effect is in fact a sub-Nyquist artifact that resonates on the mission's sampling characteristics (Peidou and Pagiatakis, 2020).

1.2 Research Objectives

The core idea of this research is to attain better performance for GRACE mission products. This idea dictates the direction of our research, that is understanding the nature and the behaviour of disturbances on GRACE mission products. To achieve this goal, we first need to address the disturbances of GRACE on-board measurements and final products that have not been fully understood up till now. Additionally, the concepts created to assess the disturbances of GRACE mission products can be further advanced to provide for the first time, the raw second derivatives of the gravitational field (i.e., gravitational gradients). In more detail, the individual tasks undertaken in this research deal with a) unravelling the origin of the "longitudinal stripes" artifact on GRACE-based gravity field models; b) understanding perturbations of GRACE instrumentation induced by dynamics occurring on the spacecraft environment and c) creating new ideas and concepts to assess perturbations of the instrumentation and to estimate gravitational gradients. These three tasks shape the research objectives as follows:

1) Assess the impact of space weather dynamics on GRACE mission instrumentation.
2) Estimate gravitational gradients using GRACE mission Level 1B data.
3) Investigate the origin of longitudinal stripes on GRACE mission gravity models.

1.3 Original Research Contributions

This research resulted in a number of original contributions to the field of geodesy, with emphasis on satellite gravimetry. The objectives answer longstanding questions in the GRACE literature. In particular, the presence of the longitudinal stripes and the space-weather related disturbances on GRACE products are studied and a new concept that leads to the estimation of gravitational gradients using GRACE on-board measurements is created.

Questions emerging from this research are summarized as follows:

1) What is the impact of space weather dynamics on the instrumentation of the GRACE mission?
2) Can GRACE mission measurements provide us with a full gravitational gradient tensor?
3) What drives the presence of stripes in GRACE gravity field models?

Answers to research questions comprise the original contributions of this research. These questions are briefly answered as follows:

1) Dynamics in the upper ionospheric layers (space weather dynamics) result in disturbances of GRACE on-board instrumentation close to the auroral and polar regions. Findings suggest that GRACE accelerometers are affected not only by the kinetic energy exchange between the uncharged particles and the spacecraft, but also by the interaction of charged particles with the electrostatic structure of the accelerometer.
2) GRACE mission can be used as a “gradiometer mission” using the concept of GRACE-GM. This concept allows us to derive multi-resolution gravitational gradients from Level 1B measurements.
3) The stripes on GRACE models are sub-Nyquist (pseudo-moiré) artifacts driven by the amplitude modulation between the geoid and the sampled signal. In fact GRACE ground tracks sample the very low frequency geoid in a “dangerous” sampling neighbourhood leading to the stripe artifact.

1.4 Thesis Outline

In Chapter 2 the GRACE satellite gravity mission is introduced. LEO space gravity missions are briefly presented, while focus is placed on GRACE payload and orbital characteristics. The basic principles for recovering the Earth’s gravitational field using GRACE measurements are explained. Finally, data processing applied to all measurements used for this research are shown.

In Chapter 3, the impact of space weather on GRACE on-board instrumentation is assessed. An introduction to the fundamentals of space weather dynamics is followed by GRACE Level 1B measurements response during days of high space weather activity. To validate that the perturbations on GRACE accelerometers are induced by space weather dynamics, geomagnetic activity data provided by external sources are employed.

The GRACE mission was designed to estimate only the first derivates of the Earth's gravitational potential via a combination of precise orbit determination and non-gravitational acceleration measurements. A new innovative method that allows for the estimation of the full gravitational gradient tensor using GRACE Level 1B measurements is presented in Chapter 4. The method called "GRACE Gradiometer Mode" or GRACE-GM, is tested over regions with known geophysical signal signatures and is validated by employing GOCE mission gradiometer measurements. Chapter 4 heavily reflects the content published in Journal of Geophysical Research: Solid Earth (Peidou and Pagiatakis, 2019).

In Chapter 5, the origin of GRACE stripes is described. A thorough analysis on the stripe spatiotemporal structure is performed and their spectral and geospatial characteristics are estimated. A combination of GRACE sampling characteristics with moiré and sampling theories shows that the stripes are sub-Nyquist artifacts, driven by oversampling the low frequency geoid in the critical neighbourhood $\frac{m}{n} f_s$, with m and n being integers and f_s being GRACE spatial sampling frequency. Chapter 5 heavily reflects the content from the manuscript published in Geophysical Research Letters (Peidou and Pagiatakis, 2020).

Finally, Chapter 6 discusses the results of this research and suggests plans for future work.

2

Exploring GRACE Mission

2.1 LEO satellite gravity missions

The Challenging Minisatellite Payload (CHAMP) mission (2000-2010) was the first dedicated satellite mission to measure the Earth's gravitational field (Reigber et al., 2002). CHAMP was a single spacecraft mission that followed a near polar orbit at approximately 450 km altitude and its payload included various instruments some of them being a magnetometer instrument assembly, a 3-D accelerometer, a stellar compass, a GPS receiver and a laser retro reflector. CHAMP measurements were particularly useful for mapping the Earth's gravitational and magnetic fields and for ionosphere modeling. In particular, the mission has been proven exceptionally useful for extracting thermospheric density models and neutral (consisted of uncharged particles) wind speeds (Doornbos and Klinkrad, 2006).

Along with the CHAMP mission, the Gravity Recovery and Climate Experiment (GRACE) dual-spacecraft mission (2002-2017) was specifically designed to monitor the time variability of the Earth's gravitational field (Tapley et al., 2004). Throughout its mission lifetime, Precise Orbit Determination (POD), inter-satellite range measurements and non-gravitational accelerations observed by GRACE (Touboul et al., 2004) have been used to model the Earth's gravitational field and detect and monitor time-varying mass changes. GRACE has contributed to the detection and monitoring of various mass transfer events of the cryosphere, hydrosphere and the solid Earth with applications such as monitoring of ice mass loss (Velicogna and Wahr, 2005); monitoring of hydrological cycles and detection of mega-earthquakes (Matsuo and Heki, 2011), to name a few.

The Gravity field and steady-state Ocean Circulation Explorer (GOCE) mission (2009-2013) on the other hand, was a single spacecraft that orbited the Earth in a nearly-polar sun-synchronous dusk-dawn orbit (Rummel et al., 2002), designed to cross the Equator at 18:00 hours (ascending node) and at 06:00 hours (descending node). GOCE was the first mission to measure the gradients of the Earth's gravitational field. The mission's ultimate goal was to determine the Earth's static gravity field with 1 cm accuracy in geoid height and 1 mGal in gravity anomalies at 100 km spatial resolution. The core scientific instrument was a 3D gradiometer that measured the Earth's gravitational gradient tensor (GGT) (Rummel et al., 2011; Stummer et al., 2012). A large number of geoscience applications in solid Earth, oceanography, seismology, glaciology and aeronomy have benefited from GOCE (Fuchs et al., 2013; Knudsen et al., 2011). The GOCE gradiometer was designed and mounted on the payload such that it could measure gravitational signals directly. To eliminate the non-gravitational forces acting on the spacecraft the mission was equipped with an along the orbit drag-compensation system.

All three LEO satellite gravity missions had different aims and consequently instrumentation and principles akin to each mission were designed appropriately to fulfill the CHAMP, GRACE and GOCE objectives. The only mission of the three that resulted in a follow-on mission was GRACE, as the nearly 15 years of continuous mass transfer information it provided was considered critical for monitoring the Earth system processes and ultimately the Earth's changing climate. Discussions for the upcoming era of satellite gravity missions have been initiated. New missions, such as the mass variation observing system by high-low inter-satellite links have been suggested and new configurations and concepts for high-accuracy gravity field maps are currently being examined (see e.g., Hauk and Pail, 2019). Some of the configurations suggested include the in-line formation, pendulum, cartwheel and bender formations (see e.g., Wiese, 2011). A good discussion on the various configurations, payloads and concepts suggested so far can be found on Cesare et al. (2016).

A brief overview of the GRACE mission follows, where the orbital characteristics and the mission's on-board instrumentation are briefly addressed. Note that the description and characteristics of GRACE apply also to GRACE-FO, as the two missions are nearly identical.

2.2 Recovering the Earth's gravitational field using GRACE

The GRACE mission was a joint partnership between the US National Aeronautics and Space Administration (NASA) and the German Aerospace Centre (Deutsche Forschungsanstalt für Luft und Raumfahrt (DLR)). The twin GRACE satellites were launched on 17 March 2002, to an initial altitude of approximately 485 km. The spacecraft orbit decayed by approximately 30 m/day. The mission followed a near-polar, non-sun-synchronous orbit (non-repeat ground track) with inclination of $89^o \pm 0.05^o$ and realized a full revolution around the Earth within approximately 94.5 minutes. The two spacecraft were separated by 220 km±50 km along orbit and over the GRACE lifetime, several orbit maneuvers (switch between heading and trailing spacecraft) were applied.

Recovering the Earth's gravitational field from space gravity measurements can be accomplished by two different approaches i.e., spacewise and timewise. Spacewise approaches model the gravitational field by projecting the measurements along the satellite's orbit to a mean orbital sphere. Timewise approaches follow a totally different concept that perceives the measurements along the orbit as timeseries and requires numerical integration of the equations of motion of the spacecraft (see, e.g., Darbeheshti et al., 2018). Both approaches are applicable to modeling the gravitational field using GRACE mission measurements. A good description of the two approaches can be found in Naeimi and Flury (2017).

Spacewise gravitational field models use range and range rate measurements at various altitudes and they project them on a mean orbital sphere. Spacewise approaches are usually realized by means of the energy balance approach (range) and the acceleration approach (range rate). On the other hand, timewise approaches employ the equations of motion for both GRACE spacecraft and the intersatellite range measurements. Several timewise approaches have been developed over the course of the GRACE lifetime, such as the classical approach, the celestial mechanics approach and the short arc approach. Usually, recovery of the gravitational field by means of timewise approaches is computationally demanding. Of note is that the different strategies and the tuning of parameters to recover the Earth's gravitational field from satellite measurements may result in significant variations in the final solutions (Darbeheshti et al., 2018). In their work, Darbeheshti et al. (2018) provide a detailed discussion on the formulation of the GRACE Level 1B data to derive spherical harmonic coefficients using an observation equation.

The core concept of the GRACE mission can be described as follows: The two spacecraft are in free-fall motion, they both measure the total acceleration of each spacecraft via GPS precise orbit determination (POD) and the non-gravitational accelerations (e.g., atmospheric drag, solar radiation pressure, etc.) acting on each spacecraft (see Equation (2.1)) via the on-board 3-D accelerometers. Additionally, the distance between the two spacecraft is continuously measured and considered to recover the Earth's time-variable component of the gravitational field. Combining the range change between two spacecraft and the POD solutions, recovery of the Earth's gravitational field is achieved.

POD is used to estimate the total acceleration induced by the Earth's gravitational and non-gravitational accelerations. Global Positioning System-Satellite to Satellite Tracking (GPS-SST) has been proven to perform the best over other techniques due to the continuous 3-dimensional tracking by LEO satellites (Kang et al., 2003). Orbit determination can be achieved by: a) kinematic orbit determination, which employs only the geometric information of GPS observations; b) dynamic orbit determination which requires the use of force models along with the geometric information; and c) reduced dynamic orbit determination that weights the force model and the geometric information in an optimal sense.

The accelerations measured by the 3D accelerometers mounted at the center of mass (CoM) of each spacecraft are free from the rotational accelerations and comprise all the non-gravitational accelerations acting of the spacecraft, due to the spacecrafts free-fall motion (Hofmann-Wellenhof and Moritz, 2006).

Overall, the acceleration estimated by each GRACE POD is given in Equation (2.1). Note that the equations of motion of each spacecraft are identical.

$$\ddot{\vec{r}} = \vec{f}_g + \vec{f}_{ng}, \tag{2.1}$$

where $\ddot{\vec{r}}$ denotes the total acceleration estimated by POD; $\vec{f}_g$ denotes the gravitational accelerations and $\vec{f}_{ng}$ stands for the non-gravitational accelerations measured by the accelerometers. The first releases of gravity field solutions (RL01-RL04) also required an additional term, the empirically modeled forces, to account for deficiencies in the force models. Release 5 (RL05) solutions did not require the use of any empirical force models (Dahle et al., 2013).

Of note is that the removal of the higher frequency temporal variations of the Earth's gravity field, was required, as the undersampling introduces aliasing (Han et al., 2004). Aliasing occurs as the spacecraft passes over nearly the same location every few days, and every time it passes it gets very different estimates of the gravity field, due to changes that occur in short periods (high frequency). These high frequencies fold-over the lower frequencies and introduce artifacts in the recovered gravity field. Mass transfers that have a period of less than a month might be induced by a variety of reasons, such as tides, hydrology and atmosphere. A good discussion on the impact of these short-period signals on GRACE models can be found in Thomspon et al. (2004); however, their elimination still poses challenges (Sheard et al., 2012) and a residual aliasing may still exist (Han et al., 2004). In Chapter 5, we examine the sampling artifacts induced by undersampling or oversampling of gravitational signals and a detailed discussion on aliasing in GRACE models takes place.

The mission's objective to map the Earth's gravitational field every month required (aside from the spacecraft equations of motion), the measurement of the inter-satellite range change (between the leading and the trailing spacecraft, hereafter referred to as GRACE-A and GRACE-B, respectively). The range change was measured by a K-band microwave tracking system (KBR) on-board GRACE, while on-board GRACE-FO, a laser ranging interferometer (LRI) system was added to the existing KBR to increase the accuracy of the measured distance. The orbits of the two spacecraft were subject to different attraction induced by the Earth's masses, as areas of larger mass concentration would result in a slightly stronger gravitational acceleration and would pull the leading satellite away from the trailing satellite, thus increasing the intersatellite distance. Accordingly, as the satellites continue along the orbit, the trailing satellite is pulled toward the lead satellite when it passes over the gravity anomaly, thus reducing the intersatellite distance. The differential of the range estimates amplifies the high frequency part of the gravitational information, leading to higher resolution gravitational maps (Kim, 2000). Figure 2.1 displays the GRACE mission concept.

Overall, a typical 30-day span of non-repeating orbits was required to create a monthly map of the Earth's gravitational field. Extreme cases in which the orbit configuration resulted in poor ground geometry and consequently in ground track resonance have been reported throughout the GRACE lifetime and their effect led to significant accuracy degradation of the gravity models (Klokočník et al., 2008; Gooding et al., 2007).

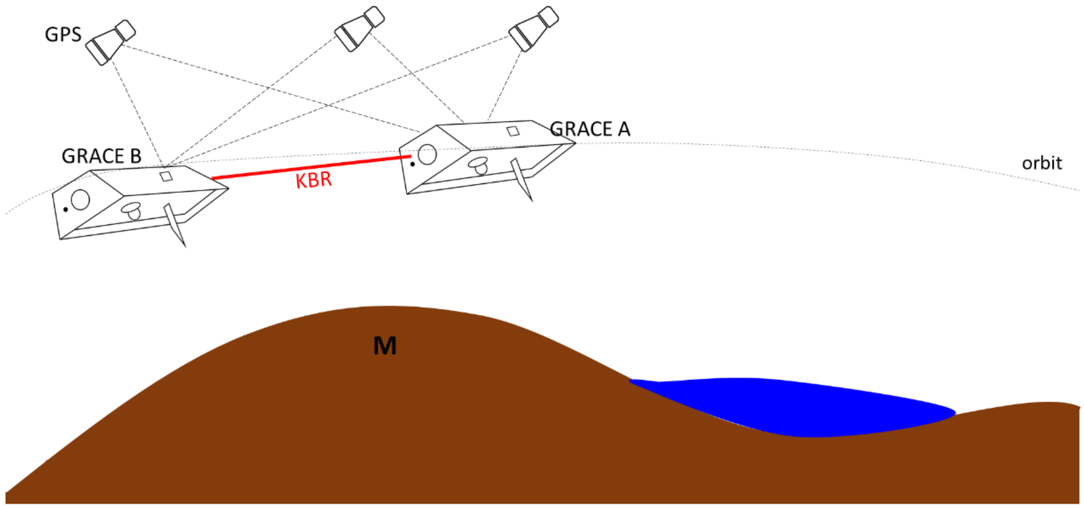

Figure 2.1: Mapping the Earth's gravitational field with GRACE mission.

Of note is that the maximum spherical harmonic degree and order (d/o) expansion of the monthly models depends on the ground track resonance (Klokočník et al., 2008). An ideal geopotential resolution requires that the maximum d/o (L_{max}) of the model is less than half the nodal revolutions of the satellite (β) (see Equation (2.2)), as indicated in Klokočník et al. (2008) and Wagner et al. (2006). In theory, GRACE's long-repeat periods[4] over a month lead to negligible changes of the ground track density for $\beta \geq 250$ and therefore the maximum resolution can be $L_{max} = 120$ (Bettadpur et al., 2004). However, in practice it was shown that the optimal maximum resolution should not exceed $L_{max} = 96$ (Dahle et al., 2014) and therefore GRACE's latest releases (RL05, RL06) are given up to d/o 96.

$$L_{max} < \frac{\beta}{2}. \tag{2.2}$$

2.3 GRACE sensors and products

To recover the Earth's gravitational field, specific science instruments are required to be an essential part of the payload. GRACE Science Data System (SDS) products consist of Level 0; Level 1A; Level 1B; and Level 2 data (Case et al., 2010). Recently, Level 3 products have been available (*Science Data System, GFZ; 2019*).

---

[4] Long-repeat periods occur when the satellite orbit experiences "weak resonances". It depends on the orbit condition (mean motions of perigee, node and mean anomaly). The interested reader is referred to Wagner et al. (2006)

Table 2.1: GRACE Science Data System products

Products	Description
Level 0	The Mission Operation System (MOS) receives and collects the raw data and stores them in the Level 0 archives. Two tracking antennas are used by the MOS to receive the science instrument and housekeeping data, twice per day for each spacecraft.
Level 1A	Science instrument binary encoded data are converted to engineering units by applying the sensor calibration factors.
Level 1B	Level 1A data are corrected for glitches in the time-tagging of the file and the sampling rate of various high-rate instruments is reduced to allow the large datasets to be manageable.
Level 2	Spherical harmonic coefficients of the Earth's gravity potential are included in Level 2 products. Recently, an alternative way of representing the Earth's gravitational field, namely the mass concentration solutions (mascons) has been decided to be part of the Level 2 products (Watkins et al., 2015; Save et al., 2016).
Level 3	Spherical harmonic coefficients are used to calculate gridded geopotential functionals (e.g., gravity anomalies, geoid, etc.). Ancillary data, such as time-series of geocentre motion are also part of Level 3 products, to allow for better geophysical interpretation of the Level 2 products.

So far only Level 1B, Level 2 and Level 3 products have been available to the public[5]. Among them, Level 1B carries all the information required to recover the Earth's gravitational field using GRACE measurements. Level 1B data comprise the main output of the science instrumentation and have the following two characteristics (Case et al., 2010):

1) All the various instrument measurements are time-registered in GPS time (defined as seconds past January 1, 2000, 12:00:00) and are provided as daily files with the following format:
   PRDID_YYYY_MM_DD_S_RL
   PRDID: product identification label (i.e., what instrument was used for this file)
   YYYY= year

[5] GRACE-FO products available to the users include Level 1A measurements.

MM= month

DD= day of month

S= GRACE satellite identifier (A or B)

RL= data product version number

2) GRACE initial data products are referenced in various coordinate systems. All Level 1B measurements are referenced in the Satellite Reference Frame (SRF), which is the local (body) reference frame for the GRACE spacecraft. (See, the Appendix for the full description of the reference frame). The other reference frames used in Level 0 and Level 1A include: the satellite frame (SF) and the accelerometer frame (AF) as defined in Case et al. (2010). The SRF is used herein and its definition is given in Table 2.2.

Table 2.2: GRACE Satellite Reference Frame

Axis	Name	Description
$\mathbf{X_{SRF}}$	Along axis	Points to the other spacecraft towards KBR phase center
$\mathbf{Y_{SRF}}$	Cross axis	Forms a right-handed triad with X_{SRF} and Z_{SRF}
$\mathbf{Z_{SRF}}$	Radial axis	Nadir
*** The origin of the SRF is within 0.1 mm from the CoM**		

The two GRACE spacecraft were identical, having length of 3.122 m and a trapezoidal cross section (height = 0.72 m; bottom width = 1.942 m and top width = 0.693 m). The outside material of the spacecraft was Carbon Fiber Reinforced Plastic (CFRP), a material that exhibits a low coefficient of thermal expansion and therefore provided the dimensional stability necessary for precise range rate measurements between the two spacecraft. To stabilize the spacecraft, an Attitude and Orbit Control System (AOCS) of non-science sensors and actuators was used. The sensors of the AOCS included: a) a Star Camera Assembly, b) a Coarse Earth Sun Sensor, c) a Magnetometer and d) an Inertial Measurement Unit (IMU), and the actuators comprised a cold gas system and three magnetorquers. The key instruments to recover the Earth's gravitational field were the GPS receivers, the K-band microwave tracking system and the accelerometers that each spacecraft carried. A more detailed description of the instrumentation and the Level 1B products follows. The GRACE Level 1B products are given in SRF coordinates and consist of the following sensors:

SuperSTAR Accelerometer

The ultra-sensitive GRACE accelerometers were located at the center of mass of each spacecraft to measure all the non-gravitational accelerations ($\vec{f}_{ng}$) that the spacecraft experienced. The accelerometer system generally consists of a) a proof mass; b) a position detection mechanism that detects changes in the position of the proof mass and c) a servomechanism that drives the proof mass back to its nominal position (Frommknecht et al., 2003). The SuperSTAR accelerometers consisted of a Sensor Unit, an Electromagnetic Excitation Unit, an Interface Control Unit and a harness (Touboul et al., 2004). The sensor unit consisted of a metallic proof mass that was servo-controlled using capacitive sensors, suspended inside an electrode cage of gold-coated silica. GRACE was not equipped with a drag-compensation system resulting in intense perturbations induced by non-gravitational forces (especially air-drag) along the x-axis. Each of the GRACE accelerometers had an unknown scale and bias in each direction. Therefore, calibration was applied to the measured acceleration. The calibration equation is as follows:

$$\boldsymbol{a_{cal}} = \boldsymbol{S a_{meas}} + \boldsymbol{b}, \qquad (2.3)$$

where $\boldsymbol{a_{cal}}$ denotes the calibrated non-gravitational accelerations along the three axes of SRF; $\boldsymbol{a_{meas}}$ denotes the non-gravitational accelerations measured (can be found in the ACC1B files); $\boldsymbol{S}$ is a 3×3 scale factor and $\boldsymbol{b}$ the 3×1 bias vector.

The bias and scale were estimated simultaneously with the spherical harmonics. The accelerometers measured the 3D accelerations with a sensitivity of $10^{-10} m/s^2\sqrt{Hz}$ along the *x* and *z* axes, and the least sensitive acceleration was along the cross-axis ($a_{y_{SRF}}$) (Touboul et al., 2004). GRACE accelerometers were designed to behave linearly within the frequency band of $10^{-4} \sim 10^{-1}$ Hz (Touboul et al., 1999). In this study, all the accelerometer measurements used were subject to a Gaussian bandpass filter[6] whose bandwidth matched that of the accelerometers. More details on the characteristics of the Gaussian filter are given in Section 2.4.

GRACE accelerometer measurements suffered from spikes (also referred to as 'twangs'); an effect initially observed on CHAMP mission accelerometer measurements. Spikes were attributed to heater on-off switching (see e.g., Bock et al., 2000) occurring every few seconds, and

[6] Gaussian filter prevents the Gibbs phenomena at the edges of the signal due to the absence of side lobes

appropriate measures (i.e., use of a very stiff material for GRACE platform) were taken to overcome this effect in GRACE-FO. Several studies suggest that GRACE spikes, which were particularly strong on the radial component, are attributed to vibrations in the multi-layer insulation (MLI) of the satellite (Touboul et al., 2004; Frommknecht, 2007). The frequency of spikes is therefore high and a low-pass filter can be used to eliminate them. The impact of spikes, especially in case they leak in lower frequencies is expected to be negligible for GRACE-FO spacecraft, as the bottom of the GRACE-FO spacecraft is made of rigid materials instead of foils (Flechtner et al., 2016). Level 1B accelerometer data provide the linear and angular non-gravitational accelerations along the three axes; and the 3D linear acceleration residuals, all for each day, at 1 Hz rate. We note that the accelerometer measurements are available at a 10 Hz rate in Level 1A products. Additionally, within the process of converting Level 1A to Level 1B data, data gaps shorter than 10 s are filled with quadratic interpolation when at least 2 points per side are known. Finally, the accelerometer data were accompanied by the AHK1B accelerometer house keeping data.

GPS Flight and Navigation Data Format

The GPS observations were a significant component of GRACE final gravitational field solutions. The GPS receivers had a capacity of 16 channels, 12 of which were used for POD and the remaining four for occultation measurements (Kang et al., 2006). The GPS high-low SST data were stored in GPS1B data files that collect all the measurements from GRACE GPS receivers. These files include the carrier phases, the pseudoranges, the receiver channels and all the parameters required to derive POD information. GNV1B files provide the final coordinates and their errors in the International Terrestrial Reference Frame (ITRF) derived from the processed GPS1B data, and the 3D velocity vector and the errors associated with it are also provided.

K-band Ranging System (KBR)

The KBR was key instrument in GRACE mission and provided continuous ultra-precise (within 10 μm) measurements of the distance between the two satellites measuring therefore the variations in gravity (Kim and Lee, 2009; Kroes et al., 2005).

The acceleration measured by the KBR is subject to corrections to account for the light time rate and the antenna offset rate as given in Equation (2.4).

$$\ddot{r}_{cal} = \ddot{r}_{meas} + light_{corr} + antenna_{corr}, \qquad (2.4)$$

where $\ddot{r}_{cal}$ is the corrected range acceleration; $\ddot{r}_{meas}$ is the range acceleration; $light_{corr}$ is the light time acceleration correction; and $antenna_{corr}$ is the antenna offset acceleration correction. All the parameters of Equation (2.4) can be found in KBR1B files.

The KBR consisted of an ultra-stable oscillator, a microwave assembly, a horn, an instrument processing unit (used for sampling both the K-Band carrier phase signal and the GPS antenna and the star cameras measurements) and a measurement processing unit. The KBR measurements required both spacecraft to transmit a carrier signal and measured the phase of the carrier generated by the other spacecraft. The sum of the phases measured is proportional to the range between the satellites, and the phase variations are cancelled out due to long-term instability in each clock (Dunn et al., 2003). The GRACE K-band had a radio frequency of approximately 24 GHz and a Ka-band frequency nearly 32 GHz generated by an ultra-stable oscillator. Ionospheric corrections were also applied through measurement of the phase changes at the two frequencies. Overall, KBR1B files provide both the range rate and the range acceleration between GRACE A and B at a 0.2 Hz rate (every 5 seconds)[7].

Laser Range Interferometer (LRI)

One of the most notable differences between the nearly identical GRACE and GRACE-FO is the use of LRI in GRACE-FO as an additional instrument to improve the accuracy of the SST measurements (Flechtner et al., 2016). The LRI system was designed by the Max-Planck Institute for Gravitational Physics. To achieve the highest possible accuracy, an optimal laser beam path had to be found, which for GRACE-FO was challenging because the LRI instrumentation was added to the existing platform. The LRI was not added to replace the KBR, but rather its purpose was to supplement the existing range measurements.

[7] More information on the KBR structure can be found a https://earth.esa.int/web/eoportal/satellite-missions/g/grace.

Star Camera Assembly (SCA)

Each GRACE spacecraft carried two-star cameras mounted close to the accelerometer to provide the attitude of the spacecraft. Both star cameras had a 45º angle sky view with respect to the zenith, on the port and starboard sides. With the main goal being to reach an accuracy of $0.1\ \mathrm{mrad}$, the SCA determined the spacecraft attitude with an accuracy $< 0.3\ \mathrm{mrad}$. To derive Level 1B quaternions, a reference quaternion was computed using the line-of-sight (LOS) between the two spacecraft and the data were corrected for time glitches. Star camera Level 1A products comprised the data obtained by the two-star cameras, namely the one camera provided the primary (1 Hz) data and the other camera the secondary (0.2 Hz) data. If the primary star camera experienced gaps shorter than 10 s, then a quadratic interpolation was applied to fill the gap, provided that at least 2 points per side of the gap were available. Data gaps longer than 10 s were not filled. No interpolation was applied to the secondary star camera quaternions. Finally, by combining the primary and the secondary quaternions employing weighted summation, the final quaternions were derived and provided in the SCA1B files in 0.2 Hz. The information of SCA1B files is particularly useful for determination of the attitude angles (roll, pitch and yaw) and for the transformation of all Level 1B measurements from the SRF to the International Celestial Reference Frame J2000.0 (ICRF).

Laser Retro Reflector (LRR)

The LRR was mounted on the bottom of each spacecraft and consisted of four prisms and served as an external calibration instrument for the on-board GPS receiver and as an independent measurement for more accurate POD solutions. The LRR constrained the estimation of the orbit solution of the spacecraft by measuring the distance of the spacecraft from terrestrial laser tracking networks with an accuracy of 1~2 cm.

Tables 2.3 and 2.4 summarize the science and non-science instruments, respectively. Additionally, the vector offset files for GPS Backup Navigation Antenna (VGB1B); Center of Mass solution from calibration maneuvers (VCM1B); GPS main antenna (VGN1B); GPS Occultation Antenna (VGO1B); KBR phase centers (VKB1B); SLR Corner cube reflector (VSL1B), are available in Level 1B data products.

Table 2.3: Science Instrumentation Description

Science Instrumentation	Level 1B data file	Description
Accelerometer	ACC1B	Provides the non-gravitational accelerations along the 3-axes
GPS	GPS1B	GPS flight data (code and phase) consisted of three range and three phase measurements (CA, L1, L2)
	GNV1B	Navigation solution (ITRF)
K-band ranging system	KBR1B	Provides the distance (range) rate of change ($\dot{r}$) and the range acceleration ($\ddot{r}$) between the two spacecraft
Laser Range Interferometer	LRI1B	Supplement KBR in distance rate ($\dot{r}$) and distance acceleration ($\ddot{r}$) measurements towards higher intersatellite distance measurement performance
Star Camera Assembly	SCA1B	Spacecraft attitude determination

Table 2.4: Non-Science Instrumentation Description

Non-Science Instrumentation	Level 1B data file	Description
Magnetometer	MAG1B	Magnetic torque rod activation data and magnetometer data
Thruster	THR1B	Thruster activation data
Star Cameras	QKS1B	Quaternion used on board to point the KBR phase center of the trailing spacecraft
	QSA1B	Alignment Quaternion from Star Camera Frame into SRF
	QSB1B	Quaternion from Satellite Body Frame into SRF (not used)

2.4 GRACE data processing

In this section, the filtering and the transformation parameters employed in the data processing are discussed.

2.4.1 Filtering

In Section 2.2.2, the sensors and the data products (see Tables 2.3 and 2.4) of GRACE were introduced. In many cases, the data arranged in daily files in Level 1B require additional processing to provide the highest accuracy and the best overall performance. GRACE accelerometers measured the non-gravitational accelerations of each spacecraft, as opposed to GOCE gradiometer that consisted of accelerometer pairs mounted off the CoM and measured directly gravitational accelerations (Rummel et al., 2011).

The GRACE accelerometer measurement bandwidth was $10^{-4} \sim 10^{-1}$ Hz that corresponds to 10-10000 seconds; that is wider bandwidth than the GOCE gradiometer bandwidth (i.e., $5 \sim 100$ mHz). Within this bandwidth, the instrument performed linearly, providing the highest precision. To isolate the useful signal from the non-linear responses, a bandpass Gaussian filter is applied. The Gaussian filter is preferred among other filters to avoid the Gibbs phenomenon at the edges, because the Gaussian window maintains its form in the frequency domain (Canuto et al., 2006). The Gaussian function is given in Equation (2.5), and the Fourier transform of the function in Equation (2.6).

$$\mathrm{g(x)} = \frac{1}{\sigma_x\sqrt{2\pi}} e^{-(x^2)/2\sigma_x^2}, \tag{2.5}$$

$$\mathrm{G}(f) = e^{-(f^2)/2\sigma_f^2}, \tag{2.6}$$

with σ_x and σ_f being the standard deviations in time and frequency domain, respectively and x being the distance from the origin. The size of the Gaussian window in the time domain is represented by $7\sigma_x$ and σ_x is a function of the cut-off frequency.

The pass-band of the Gaussian filter is set to $[10^{-4} \sim 10^{-1}]$ Hz based on the half-amplitude point principle (i.e., the frequency at which the output decreases by half of its peak at approximately -3 dB).

Figure 2.2 displays the amplitude spectral density – (ASD), which is the square root of power spectral density of GRACE A linear accelerations along the 3-axes in the SRF (a_x, a_y, a_z) for a random day. All three accelerometer components exhibit similar behaviour within the interval $[4 \cdot 10^{-3} \sim 7 \cdot 10^{-2}]$ Hz and the orbital ($1.74 \cdot 10^{-4}$ Hz) and semi-orbital ($3.55 \cdot 10^{-4}$ Hz) frequencies are displayed with purple dashed lines. The filtered ASD of GRACE A linear accelerations is shown in Figure 2.3. In Figure 2.4 we show the ASD of the difference between the original and the filtered accelerations. The y-axis appears to be the most affected by the filtering process.

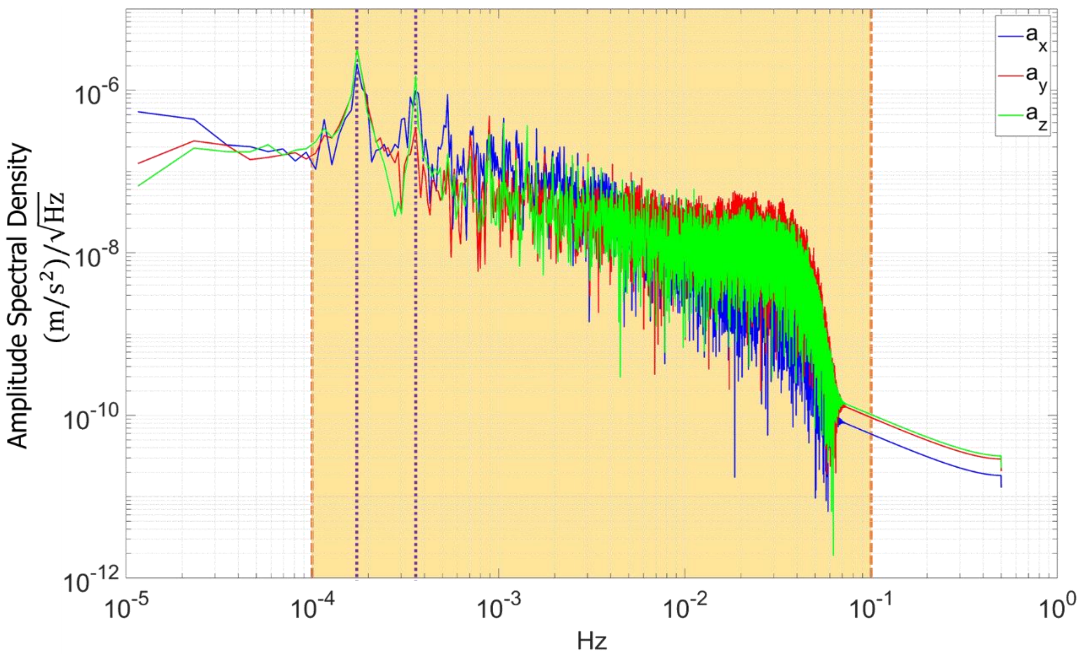

Figure 2.2: Amplitude Spectral Density (ASD) of the non-gravitational accelerations as measured on March 5th 2010. The orange area denotes the instrument bandwidth and the purple dashed lines represent the orbital ($1.74 \cdot 10^{-4}$ Hz) and semi-orbital ($3.55 \cdot 10^{-4}$ Hz) frequencies.

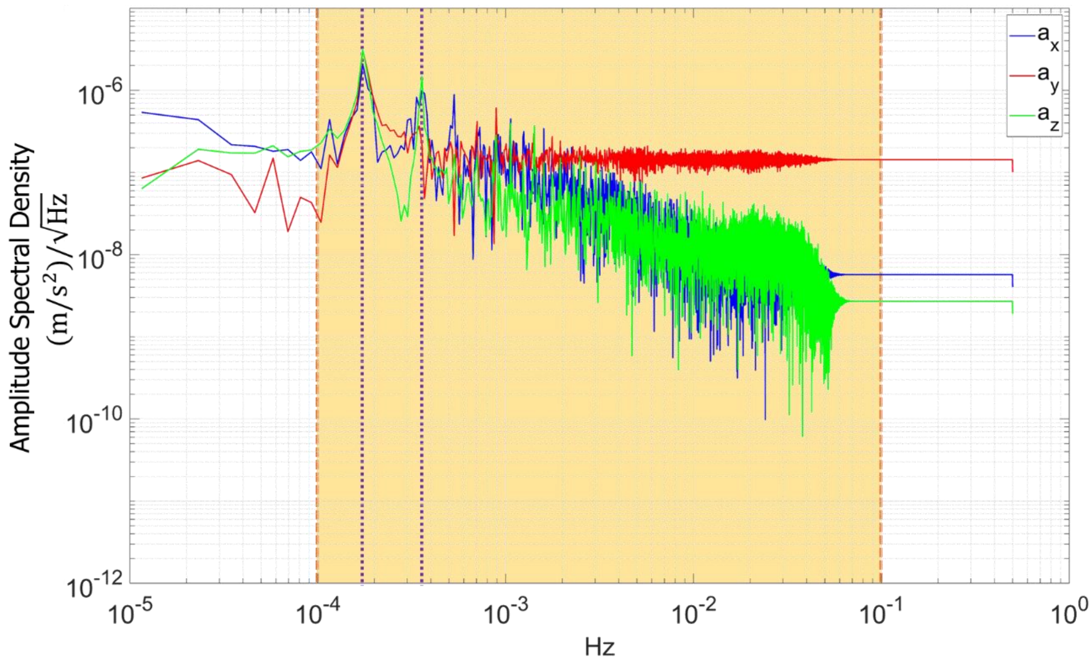

Figure 2.3: Amplitude Spectral Density (ASD) of the filtered non-gravitational accelerations as measured on March 5th 2010. The orange area denotes the instrument bandwidth and the purple dashed lines represent the orbital ($1.74 \cdot 10^{-4}$ Hz) and semi-orbital ($3.55 \cdot 10^{-4}$ Hz) frequencies.

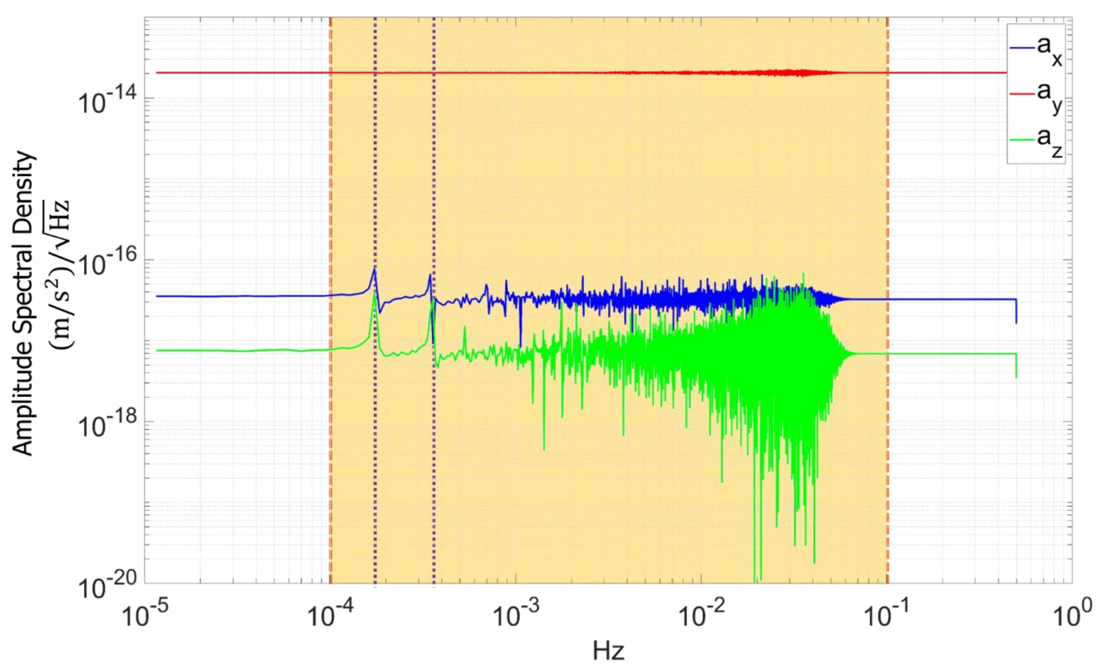

Figure 2.4: Amplitude Spectral Density (ASD) of the difference between the filtered and the original non-gravitational accelerations as measured on March 5th 2010. The orange area denotes the instrument bandwidth and the purple dashed lines represent the orbital ($1.74 \cdot 10^{-4}$ Hz) and semi-orbital ($3.55 \cdot 10^{-4}$ Hz) frequencies.

2.4.2 Transformations

An essential part of the GRACE measurement processing and validation for this research, is the transformation of measurements from one reference frame to another. GRACE on-board instrumentation uses various reference frames, but the end-user has access only to Level 1B measurements, all referenced to the SRF. The definitions of all the coordinate systems used in this research are as follows:

Satellite Reference Frame (SRF): The SRF is the coordinate system that all GRACE Level 1B products are referenced to. The SRF is a satellite body-fixed frame with origin within 0.1 mm at the accelerometer frame origin (that coincides with the CoM). Details of the SRF can be found in Table 2.2.

Accelerometer frame (AF): The accelerometer frame (AF) origin is at the center of mass (CoM) of the spacecraft. The AF coordinate axes are directed as shown in Figure 2.5.

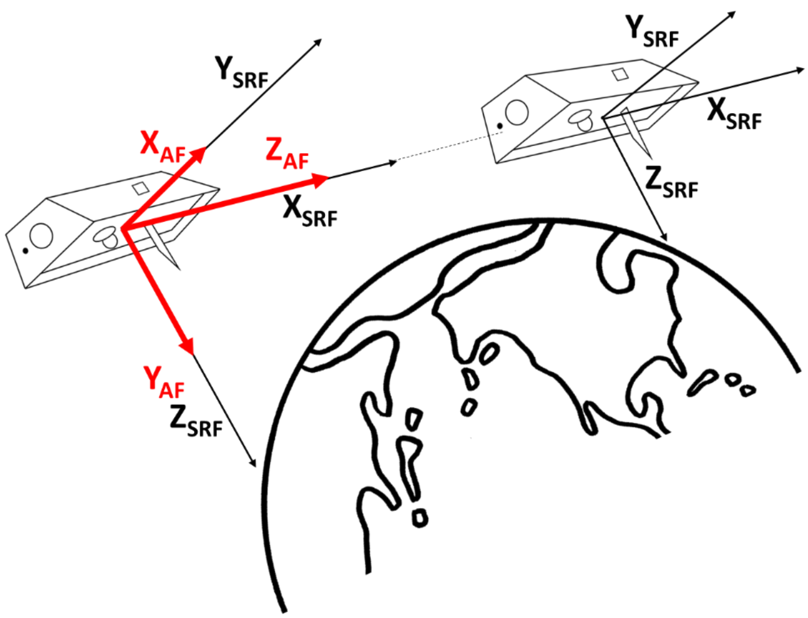

Figure 2.5: Satellite body-fixed frames; The AF is denoted with red colour and the SRF with black.

International Celestial Reference Frame (ICRF): The inertial frame ICRF is realized by the J2000.0 equatorial coordinates of extragalactic radio sources measured from Very Long Baseline Interferometry (VLBI). It is a modern reference frame and as such it incorporates in its very definition the fourth dimension, i.e., time. ICRF is an equatorial system with origin at the barycenter of the solar system. The *xy*-plane (i.e., the principal plane) is very close to the mean Equator of J2000.0; The x-axis (reference direction for the right ascension) is fixed on the mean Equator and is pointing very close to the dynamical equinox of J2000.0. The reference pole is defined by the z-axis that is perpendicular to the principal plane (*xy*-plane) and the y-axis defines the right-handed system. The time scale is the barycentric coordinate time. More details on the ICRF definition can be found in Petit and Luzum (2010) and in McCarthy (1996).

International Terrestrial Reference Frame (ITRF): ITRF is an Earth-Fixed Reference Frame and realizes the International Terrestrial Reference System (ITRS) by providing three dimensional coordinates in a specific coordinate system. ITRF is a geocentric frame, with the center of mass defined for the whole Earth. The *xy*-plane coincides with the mean equatorial plane of BTS84, within about 0.005”.The z-axis is perpendicular to the equatorial plane and the x and y-axes define the terrestrial equatorial plane, with y-axis completing the right-handed system (Petit and Luzum, 2010).

East North Up (ENU): ENU is a local (topocentric) coordinate system aligned to the direction of the geodetic reference ellipsoid normal at the measurement point. The origin of ENU is at the measurement point (P). The Up-axis is directed outwards of the reference ellipsoid along the ellipsoid normal; the North-axis is perpendicular to the Up-axis and points towards the ellipsoidal north (i.e., along the meridian of longitude) and the East-axis completes a right-handed Cartesian system. Note that some institutions and agencies use a left-handed cartesian system, that is north-east-up (NEU) systems or north-east-down (NED) systems (Jannsen, 2009).

Geocentric Solar Ecliptic (GSE): GSE serves as a coordinate system for various space applications and is defined as follows: The origin of this system is the geocentre. The x-axis points towards the Sun centre, the z-axis coincides with the Earth’s spin axis (to the north), and the y-axis completes a right-handed Cartesian system (chosen to be on the ecliptic plane pointing towards dusk). A visual representation of the GSE reference frame can be seen in Figure 2.6. The transformation parameters applied in this research can be found in Appendix I.

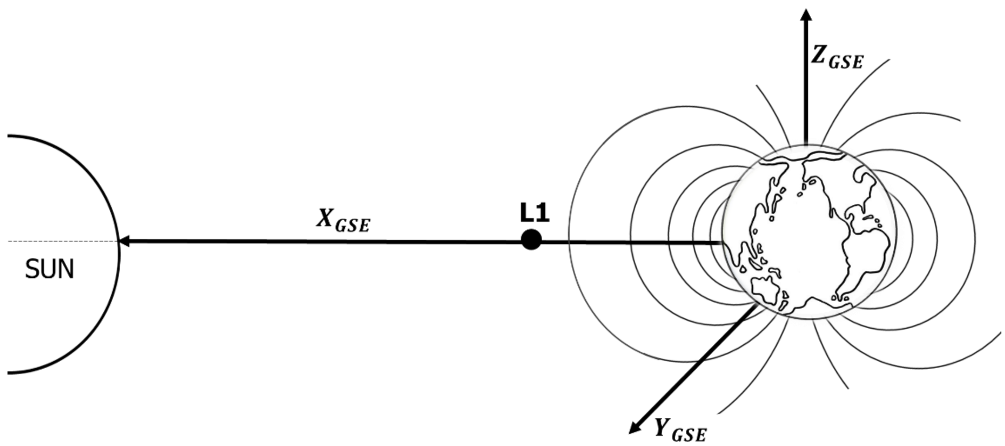

Figure 2.6: GSE coordinate system definition. L1 resembles the Lagrange point 1.

2.5 Summary

In this chapter, GRACE mission payload and data processing were presented. Overall, this chapter introduced the reader to GRACE mission, by describing a) the concept of the mission; b) the on-board instrumentation; c) the data products of the mission; d) the filtering of the data, and e) the reference frames used in this study. The core GRACE instruments used in this study are the accelerometers, the GPS receivers and the star camera assembly, that measure the non-gravitational acceleration, the position and the attitude angles, respectively.

3

Space weather dynamics and GRACE

Improving the accuracy of GRACE models requires a deep understanding of GRACE instrumentation. While analyzing GRACE on-board measurements, we found an interesting correlation between disturbances of the measurements and space weather affecting the spacecraft. In Section 3.1, we introduce the fundamental concepts related to space weather and in Section 3.2, focus is placed on geomagnetic storms and discuss their impact on GRACE instrumentation. In Section 3.3 the concept of GRACE differential mode (DM) is presented and in Sections 3.4 and 3.5, the input datasets of electromagnetic energy, namely the ACE mission measurements, the vertical and horizontal electric currents and Poynting flux estimates are explained. We present the impact of various scale geomagnetic storms on GRACE DM estimates and we further perform coherence analysis between these estimates and ACE/Poynting flux estimates.

3.1 Space weather

Space weather is a rather complex term that describes various conditions of the Earth's surrounding space (Cade and Chan-Park, 2015). In this study we refer to space weather to describe the dynamics occurring in the Earth's upper ionospheric layers (Cade and Chan-Park, 2015). This correlation is not unknown to LEO space gravity missions, as the GOCE mission experienced very similar disturbances (Ince and Pagiatakis, 2016). At the first stages of this research, a thorough analysis of the behaviour of GRACE instrumentation was conducted. Although it is well established that space weather dynamics influence the performance and reliability of space-borne and ground-based technological systems (Moldwin, 2008; Ince, 2016), space weather-related perturbations on GRACE have not yet been fully understood. To fill this knowledge gap, analysis of GRACE Level 1B measurement response to geomagnetic storms is undertaken. After all, although disturbances in satellite motion are expected due to kinetic energy exchange between neutral particles and the spacecraft, the impact of charged particle flow on GRACE instrumentation has yet to be assessed.

We now define the fundamental concepts and terms that describe the spacecraft environment (i.e., space weather). All the physical dynamics occurring in the upper ionospheric layers (>80 km) are called space weather, and in this research, focus is placed on phenomena such as geomagnetic storms, rather than other non-gravitational forces that also belong to space weather (i.e., solar radiation etc.). Of note is that the physical dynamics of the Earth's upper atmospheric layers (space weather) are proportional to the Sun's activity (Moldwin, 2008).

The Earth's atmosphere consists of various layers, each of them having different properties in the composition of the layers and extending to a different altitude above the Earth. The atmospheric layers of the Earth and the associated temperatures and plasma density profiles (Kelley, 2009) are shown in Figure 3.1. The temperature profile shows a smooth temperature gradient between the troposphere and the mesosphere. On the other hand, at approximately 90 km altitude, radiation cooling sharply reduces temperature. Note the rapid increase in the temperature above the mesosphere, induced by the high energy solar photons (Kelley, 2009).

LEO satellites orbit the Earth at an altitude covered by the layer of ionosphere (ionosphere altitude ranges between nearly 60-2000 km). The ionosphere consists mostly of ionized gas and overlaps with the upper portion of the neutral atmosphere (consists of neutral gas). The ionosphere is subdivided in different regions, namely the D (60-90 km), E (90-120 km) and F (>150 km), the latter being further divided into F1 and F2. In each region the electric field-driven currents are formed in different directions (Kelley, 2009). Generally, the electric currents in each region depend on the local time, the latitude and the season. However, in the F region (the region of interest for LEO satellites), the currents show the weakest variability with respect to the time (Kelley, 2009).

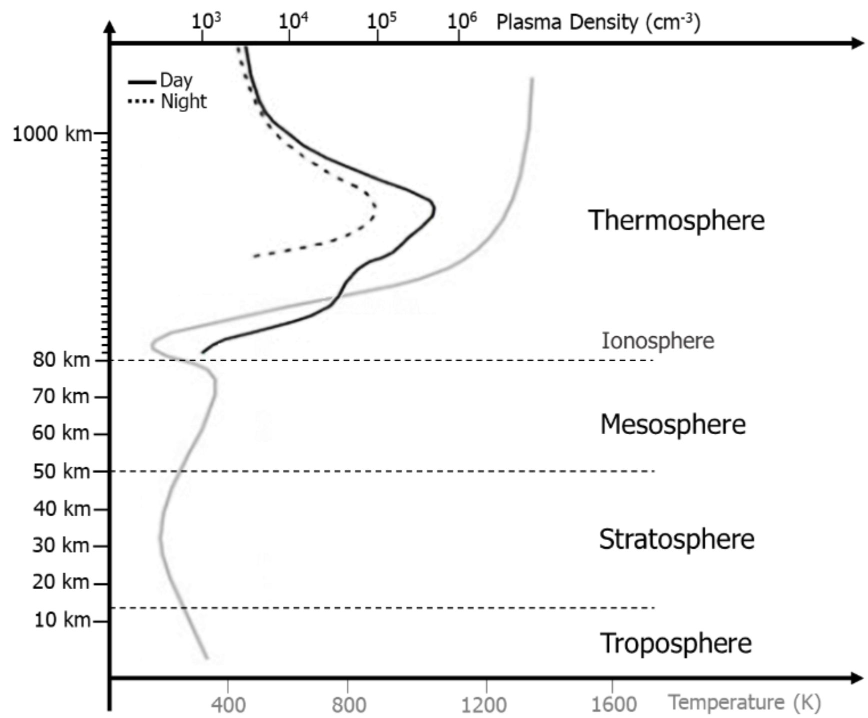

Figure 3.1: Profiles of neutral atmospheric temperature and ionospheric plasma density for the various layers of the atmosphere. The profiles are estimated for mid-latitudes (modified from Kelley, 2009).

Solar winds can be described as magnetized plasma (ionized gas consisting of nearly the same amount of protons and electrons) that move supersonically away from the Sun and carry with it the Sun's magnetic field (Moldwin, 2008). The part of the Sun's magnetic field that is propagated out of the heliosphere by the solar wind is called interplanetary magnetic field (IMF). The velocity of a solar wind highly depends on the Sun's activity and the location of the solar source from which the winds are emitted (Richardson and Paularena, 1998). The Earth's magnetic field is supressed when subject to solar winds (see Figure 3.2). Solar winds affect the magnitude of the velocity, and the density of neutral winds and plasma flux. When solar wind pressure decreases, the magnetosphere expands. The main components of the Earth's magnetosphere affected by solar winds are plasma flux (consisting of charged particles) and neutral winds (consisting of neutral particles). The interaction of plasma flux and neutral winds results in changes to the satellite environment, and, consequently, it causes perturbations of the on-board instrumentation. These perturbations are yet to be identified and quantified for GRACE and GRACE-FO missions.

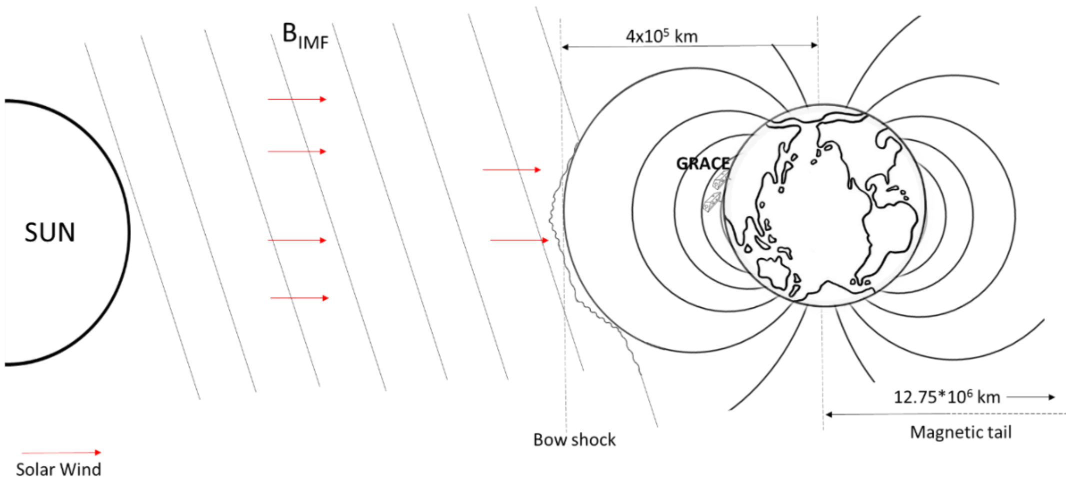

Figure 3.2: The Earth's Magnetic field and solar winds. Bow shock is the boundary where solar winds encounter the Earth's magnetopause.

Intermittently, the energy input of the Sun to the Earth's magnetosphere increases rapidly and the phenomena behind this extensive energy transfer are corona mass ejections (CMEs), solar flares, and solar energetic particles (SEPs). The geomagnetic storms lead to significant variations of the currents, plasma, and electric fields in the Earth's magnetosphere. The number of storms depends on the solar activity that typically changes a few times per month. In the case of solar sunspot maxima, both the number and the intensity of the storms increase rapidly. Solar winds that result in geomagnetic storms persist from a few to many hours with wavelengths usually exceeding several hundred kilometers (Zhang et al., 2003) and have three phases: sudden storm commencement (SSC), main phase, and recovery. Some of the currents induced, called auroral currents or auroral electrojets, produce large magnetic disturbances. Overall, geomagnetic storms impact the ionosphere and eventually cause extra drag in LEO satellites.

The index measuring the overall variability of the Earth's magnetic field due to geomagnetic disturbance is called the K_p index. The K_p index is provided in a logarithmic scale and ranges between 0 and 9 with the average K_p level being approximately 3. The index is given in three-hour intervals in Universal Time (Rostoker, 1972). Disturbance sources may be attributed to any geophysical current system including magnetopause currents, field-aligned currents, and auroral electrojets (Gonzalez et al., 1994). In case of geomagnetic storms, currents and energetic particles amplify the energy in the form of heat and consequently the density of the electrons in the ionospheric layers increases.

3.2 Geomagnetic perturbations on GRACE instrumentation

In early November 2004, the Sun was very active and generated many strong interplanetary and magnetospheric disturbances (Yermolaev et al., 2008). In that period, an intense geomagnetic storm occurred resulting in a magnetospheric disturbance from 8-10 November, 2004. The response of GRACE instrumentation to these very intense space weather conditions is investigated.

The GRACE accelerometers measured the non-gravitational accelerations acting on the spacecraft. Therefore, the impact of a geomagnetic storm on the acceleration of the satellites was measured by the accelerometers. At the beginning of our analysis, we wish to quantify the response of the accelerometer to extreme geomagnetic storms. We compare the instrumentation response during a day with very low K_p index and during an intense geomagnetic storm, such as the one that occurred on November 2004.

Non-gravitational accelerations along the track (a_x) during a day of low space weather activity (Figure 3.3; left panel) and during a day of intense geomagnetic storm (Fig 3.3; right panel) show the magnitude of disturbance that the spacecraft experienced as measured by the accelerometer. Additionally, we notice that the measurements are highly disturbed (signal-to-noise ratio is roughly 15 dB) near the auroral and polar regions (Fig 3.3b). Of note is that the accelerometer measurements at the North Pole tend to be more disturbed than the South Pole. Although this behaviour is not fully explained, it might be associated with the thermospheric mass density, which is denser closer to the North Pole and less dense closer to the South Pole (Liu et al., 2014). The non-gravitational accelerations along the track, measured during the days of low geomagnetic activity and high geomagnetic activity are shown in Figure 3.4a and Figure 3.4b, respectively.

The GRACE attitude system consisted of cold-gas thrusters mounted symmetrically around its centre of mass and of the magnetic torquer rods. The main attitude actuator consisted of the magnetic torquers and the thrusters that were used in pairs to rotate the spacecraft with respect to the centre of mass. The tanks were loaded with ~16 kg of propellant. The GRACE attitude system was activated approximately 600 times per day (Flury et al., 2008) and could use up to 1 million thruster actuation cycles (Schelkle, 2000). Enough fuel was stored in the tanks for GRACE to reach almost triple its design lifetime without exhausting its fuel (Bandikova, 2016).

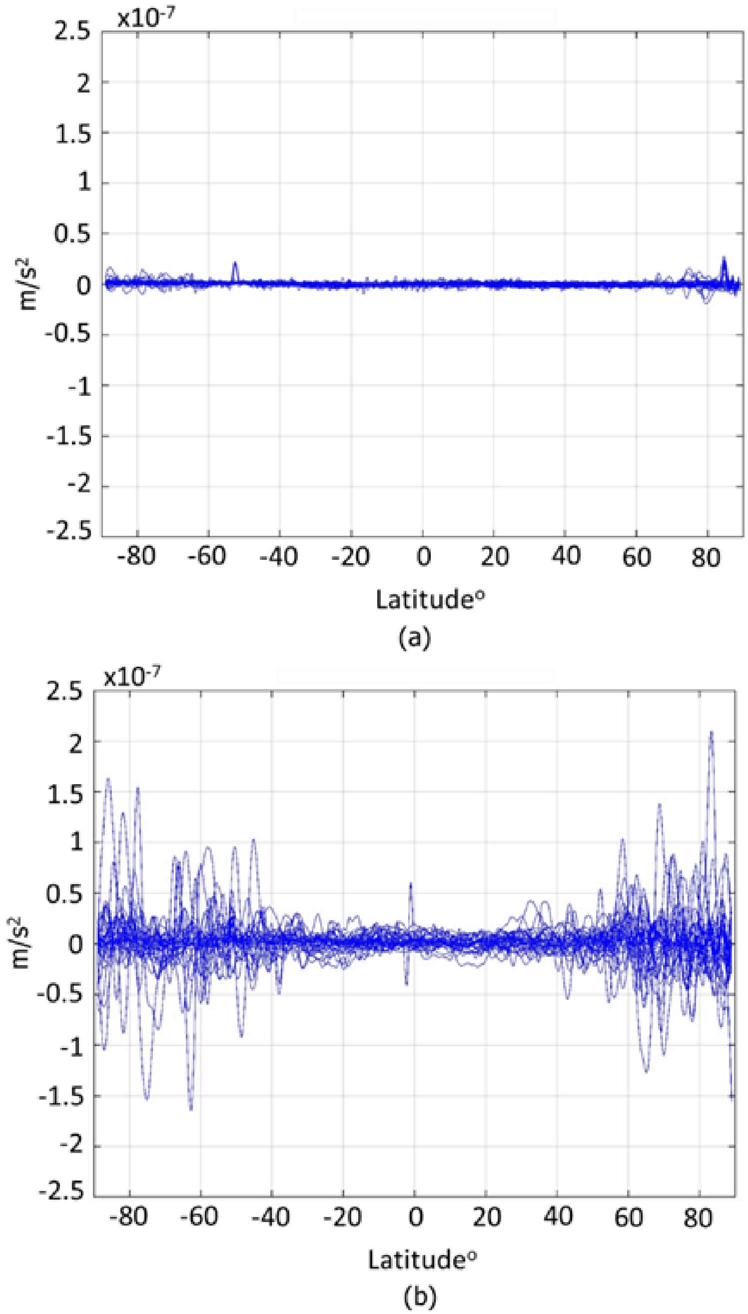

Figure 3.3: a) Accelerations along the x-axis (a_x) during November 5, 2004 (K_p <5); b) a_x during November 10, 2004, when an intense geomagnetic storm disturbed the upper layers of the ionosphere (K_p index ranged between 8 and 9).

Due to dynamics occurring in the satellite environment, the attitude control system activated the cold-gas thrusters to maintain the satellite attitude and the pointing requirements of the K-Band inter-satellite ranging (KBR) system (Schelkle, 2000; Frommknecht, 2007).

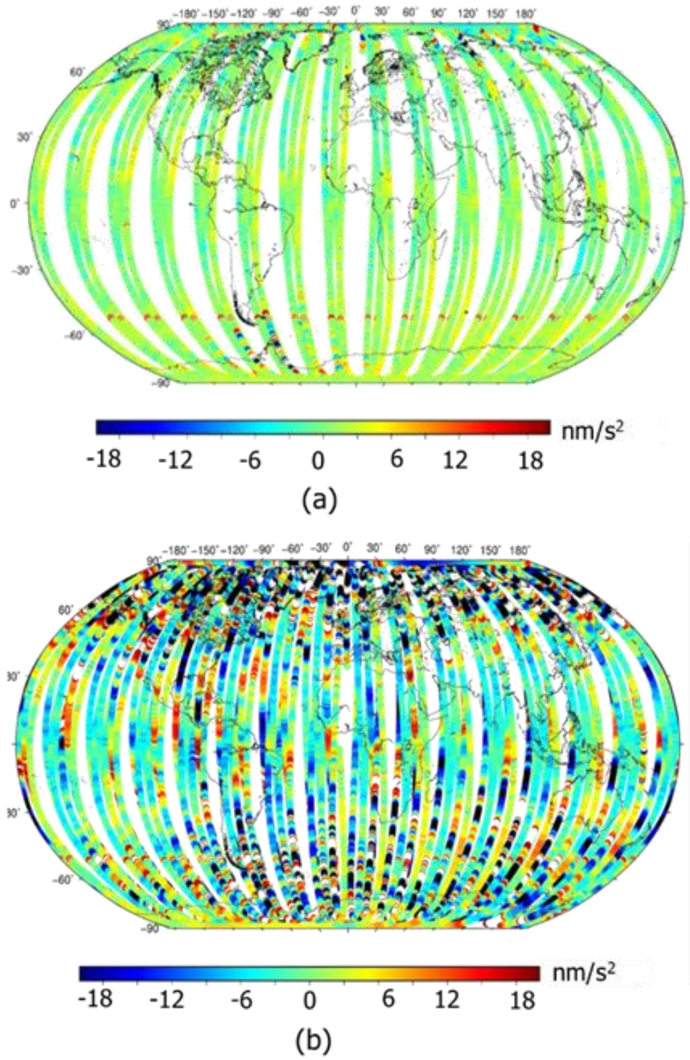

Figure 3.4: a_x during Nov 5-7, 2004 (K_p <5); b) a_x during Nov 8-10, 2004 (K_p ranged between 8 and 9).

Figure 3.5 displays the thruster activity on a day of low geomagnetic activity (left panel) and on a day of very intense geomagnetic activity (right panel). Undesirable disturbances in the satellite environment caused by space weather trigger the activation of the attitude control system. The firing of thrusters impacts the accelerometer as it creates residual linear accelerations in the form of spikes (Bandikova, 2016). Although, improvements in the data processing have been suggested and applied, there are still perturbations evident in the accelerometer measurements (Klinger and Mayer-Gürr, 2016). In this study, we assume that the impact of thrusters on the accelerometer is not the major cause of the perturbations shown in the signal and we further proceed on characterizing the source of the disturbance.

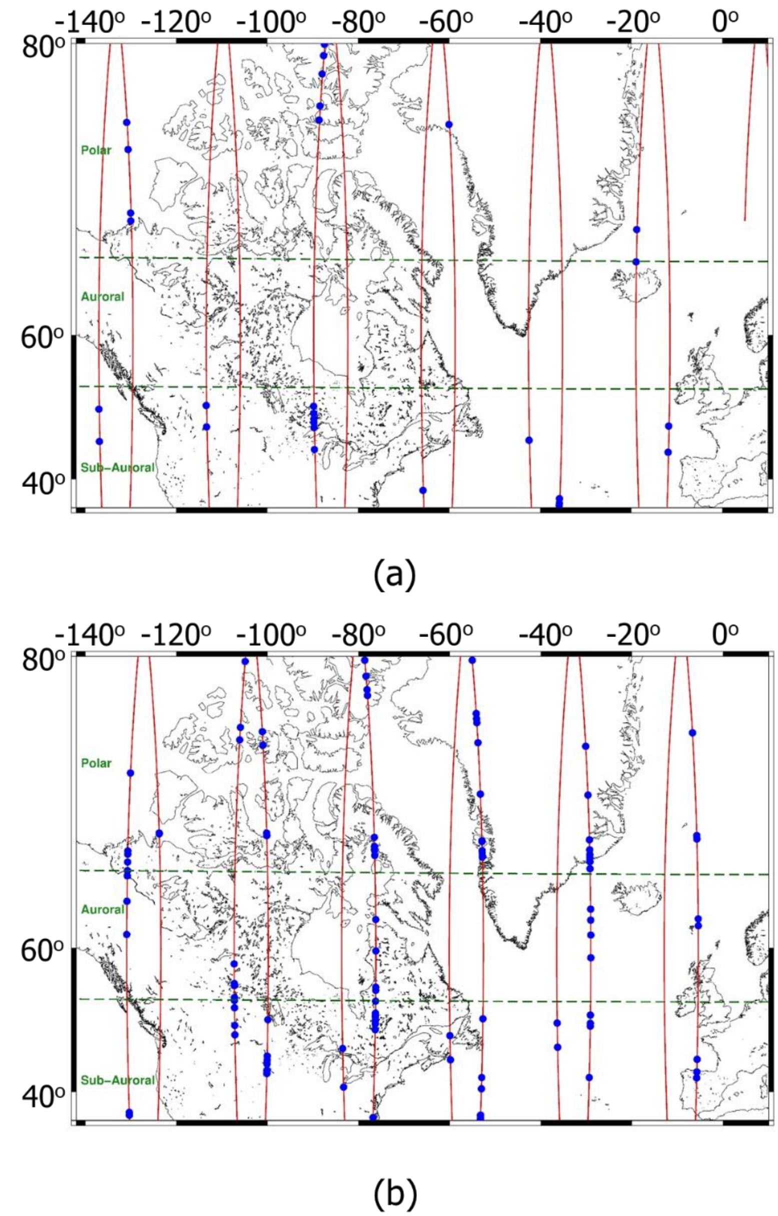

Figure 3.5: (a) Thruster activity on November 5, 2004 (K_p<5); (b) Thruster activity on November 10, 2004 (K_p ranged in [8, 9]). Red lines denote the ground tracks during the days of interest; blue dots denote the region where the attitude control system was activated.

Our analysis of the attitude behaviour of the spacecraft showed that the attitude angles typically do not exceed 3 mrad, however, in days of geomagnetic storms the magnitude of the roll, pitch and yaw angles showed a rapid increase by nearly 40 times.

3.3 The concept of GRACE Differential Mode

From the analysis presented in Section 3.2, it appears that the spacecraft is subject to disturbances due to space weather dynamics. Arguably, GRACE accelerometers were dedicated to measure these forces and eliminate their contribution from the final gravity field solution by subtracting them from the POD solution (cf., Equation (2.1). The question then arises: Are all the instruments affected when subjected to geomagnetic storms? If the accelerations derived from the GPS antennas are affected by the disturbance on the motion of the spacecraft, is this disturbance proportional to the disturbance measured by the accelerometers? As discussed in Section 3.1, the flow of geomagnetic storms consists of two main parts, the flow of uncharged and charged particles, which when interacting with the spacecraft lead to kinetic and electromagnetic energy exchange, respectively. Klinger and Mayer-Gürr (2016) study the impact of temperature deviations on the accelerometer and discuss the need for parametrization of scale factors and biases to calibrate the accelerometer measurements and improve the C_{20} (C_{20} spherical harmonic, also known as Earth's dynamic oblatenss, expresses the flatenning of the Earth). The driving force of the deviations of temperature is attributed to the solar and geomagnetic activity (Klinger and Mayer-Gürr, 2016). Therefore, the electrostatic structure of the accelerometer is expected to interact with charged particles (plasma flux) perhaps in a non-linear sense. This interaction has also been implied in the work of Ince and Pagiatakis (2016), where GOCE gradiometer measurements, although derived from differencing the accelerometer measurements, still suffered from unwanted signatures related to the plasma flux. There is a need to better understand the magnitude of the accelerometer disturbances on the final gravitational acceleration solutions. Additionally, we need to show that these accelerometer disturbances are driven by the Earth's geomagnetic acitivity.

Better understanding of the source of disturbance (i.e., kinetic energy exchange or electromagnetic energy exchange) would be feasible if the GRACE mission carried the appropriate instrumentation to derive differential measurements, as with the GOCE mission. The idea is that differential accelerations would cancel out any perturbation related to the motion of the spacecraft, as in GOCE gradiometer measurements, and therefore any other perturbations not related to the motion (such as plasma flux) would still be visible.

The GRACE mission did not carry a gradiometer and no differential accelerations are available. Therefore, a new data processing methodology is required to allow for the estimation of differential accelerations. This need led to a new idea that is, perceiving the twin GRACE spacecraft as one fictitious satellite with two accelerometers in order to derive differential accelerations.

To generate differential type 'measurements' from GRACE, we use the original generic accelerometer measurements from both satellites. This can be achieved by computing the time Δt the trailing satellite (hereafter B) takes to be as close as possible, position-wise, to where A was Δt seconds earlier, which will essentially mean that A(t) and B(t+Δt) will be at a very short distance that reaches up to maximum of a few kilometres. This process is followed by a transformation of the accelerometer measurements of B(t+Δt) into the accelerometer frame of A(t) via the attitude angle differences that occur in the time interval Δt, according to Bandikova and Flury (2014). A great discussion of the behaviour of the star cameras and the different transformations required to process GRACE measurements, can be found in Bandikova (2016).

The transformation of GRACE B(t+Δt) accelerations from SRF of B to ICRF is done using quaternions derived from the star cameras of GRACE B. Later, using the quaternions of the star cameras mounted on GRACE A we transform the accelerations to the SRF of GRACE A. These transformations are described in Equations (3.1) and (3.2).

$$\begin{bmatrix} \mathrm{X}_{\mathrm{ICRF}}^{\mathrm{B(t+\Delta t)}} \\ \mathrm{Y}_{\mathrm{ICRF}}^{\mathrm{B(t+\Delta t)}} \\ \mathrm{Z}_{\mathrm{ICRF}}^{\mathrm{B(t+\Delta t)}} \end{bmatrix} = \mathbf{R}_{\mathrm{QB}}^{-1} \begin{bmatrix} \mathrm{X}_{\mathrm{SRF}}^{\mathrm{B(t+\Delta t)}} \\ \mathrm{Y}_{\mathrm{SRF}}^{\mathrm{B(t+\Delta t)}} \\ \mathrm{Z}_{\mathrm{SRF}}^{\mathrm{B(t+\Delta t)}} \end{bmatrix}, \tag{3.1}$$

$$\begin{bmatrix} \mathrm{X}_{\mathrm{SRF}}^{\mathrm{A(t)}} \\ \mathrm{Y}_{\mathrm{SRF}}^{\mathrm{A(t)}} \\ \mathrm{Z}_{\mathrm{SRF}}^{\mathrm{A(t)}} \end{bmatrix} = \mathbf{R}_{\mathrm{QA}} \begin{bmatrix} \mathrm{X}_{\mathrm{ICRF}}^{\mathrm{B(t+\Delta t)}} \\ \mathrm{Y}_{\mathrm{ICRF}}^{\mathrm{B(t+\Delta t)}} \\ \mathrm{Z}_{\mathrm{ICRF}}^{\mathrm{B(t+\Delta t)}} \end{bmatrix}, \tag{3.2}$$

where **R** is the 3×3 rotation matrix as given in Equation (30) in the Appendix; and the subscripts $_{\mathrm{QA}}$ and $_{\mathrm{QB}}$ denote the quaternions derived from GRACE A and B, respectively.

The concept of differential mode is schematically displayed in Figure 3.6. The formulation of the new method and further considerations are presented in Section 4.2.

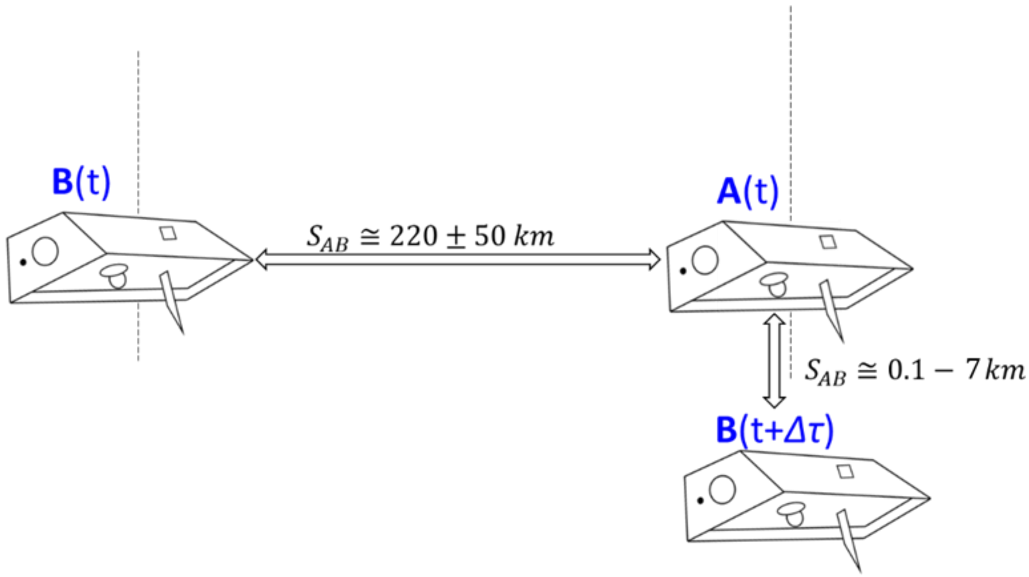

Figure 3.6: GRACE Differential mode concept.

The use of the attitude angles in the estimation of differential accelerations implies that the DM accelerations include gravitational and non-gravitational signals (see Section 4.2 for more details). Additionally, as both spacecraft are nearly in the same position within the 20-40 s time interval, the non-gravitational forces acting on each spacecraft are nearly the same (Zhang et al., 2003) and therefore the differential acceleration measurements should ideally cancel out the geomagnetic storm-related peaks of the accelerometers. If this cancellation is not observed, then the instrumentation experiences disturbances that need to be further studied, similar to those that perturbed GOCE measurements (Ince and Pagiatakis, 2016). We will perform an analysis in which data from both missions (GRACE and GOCE) will be used to assess the impact of geomagnetic perturbations on GRACE instrumentation.

We derive longitudinal profiles of DM linear accelerations along the x-axis (a_{dx}) for the two days of interest (i.e., 5th and 10th of November), displayed in Figure 3.7. It is evident that when at differential mode, the disturbances do not cancel out, but rather they seem to aggregate. A similar behaviour was observed on GOCE GGT measurements (Ince and Pagiatakis, 2016). This behaviour may be attributed to the interaction of charged particles with the electrostatic structure of the accelerometers. If disturbances on the accelerometer measurements were driven by perturbations on the motion of the spacecraft, then the differential mode approach would have cancelled them out, instead of aggregating them. In this study the errors of the estimated DM accelerations are not considered, and conclusions are drawn using only the estimated DM accelerations. A more detailed analysis is needed in the future to account for the instrumentation errors.

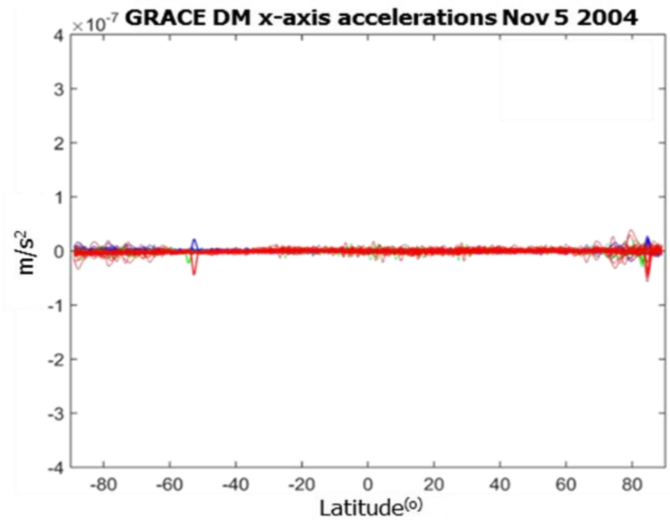

(a)

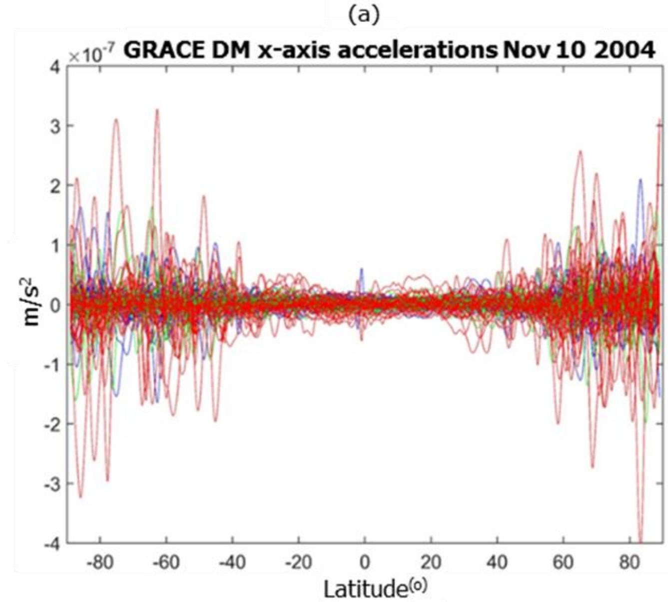

(b)

Figure 3.7: a) GRACE-A and B a_x and their difference a_{dx} (DM) on November 5th; b) GRACE-A and B a_x and their difference a_{dx} on November 10th. Blue line denotes a_x derived from GRACE-A; green line a_x derived from GRACE-B and red line the a_{dx}.

3.4 GRACE and Advanced Composition Explorer B-field

In the previous sections we showed that the GRACE accelerometer measurements appear to be affected by the plasma flux. Similar findings are drawn by Klinger and Mayer-Gürr (2016), who analyzed the temperature-dependent behaviour of the accelerometer scale factors and biases. In our study, we wish to make use of the GRACE Differential Mode (DM) method to investigate its capability to assess the impact of charged particles on GRACE accelerometers by analyzing a wide range of ionospheric conditions that the satellite experienced. Namely, we look at the DM signal and we compare it with the B-field measurements. Afterwards, the DM accelerations are compared with interplanetary magnetic field and plasma flux signatures to identify any similar behaviour.

Our analysis employs more than 200 orbits during geomagnetic storms of varied intensity characterized by the K_p index. In this study, electromagnetic field estimates provided by both satellite and terrestrial measurements are employed to assess any similar behaviour between GRACE DM and magnetic field disturbances.

Similar analyses of the GOCE mission Gravitational Gradient Tensor (GGT) disturbances showed that the Laplace equation (that is the sum of the second derivatives of the potential is zero outside the Earth's masses, i.e., $\Delta V = 0$) is not satisfied ($\Delta V \neq 0$) during geomagnetic storms (Ince and Pagiatakis, 2016). The trace of the GGT (i.e., $V_{xx} + V_{yy} + V_{zz}$) should be nominally zero, however as the quantities are measured and therefore suffer from errors, this condition is violated. In their work, Ince and Pagiatakis (2016) noticed that when GOCE was subject to geomagnetic storms the magnitude of the tensor peaked, which indicated that the gradiometer was highly affected by space weather disturbances.

At the initial stage of our analysis, we employ the Advanced Composition Explorer (ACE) solar mission interplanetary magnetic field (IMF) measurements. The ACE mission (1997~present) is dedicated to observing energetic particles coming from the Sun and other sources (Stone et al., 1998). Interplanetary magnetic flux density (magnetic induction) $\mathbf{B}$ is retrieved from various sensors on-board ACE. Although ACE provides global coverage, the orbit of the mission (1.5 million km away from the Earth) could reduce the correlation between ACE and GRACE (~500 km away from the Earth). Thus, initial focus is placed on the disturbance signatures in the GRACE measurements rather than the actual values measured. To assess the impact of the disturbing magnetic field on accelerometers, the ACE **B**-field estimates are transformed into the GRACE satellite reference frame (SRF), i.e., the local frame to which all GRACE Level 1B data are referenced. The process includes the transformation from the Geocentric Solar Ecliptic Coordinate System (GSE) to the International Terrestrial Reference Frame (ITRF) and then to the International Celestial Reference Frame (ICRF) (Hapgood, 1992). Finally, the **B**-field values are transformed to the SRF using orientation angles (Bandikova and Flurry, 2014). The formulation of the transformations applied is presented in the Appendix.

We analyze all the orbits of GRACE during November 10 and results indicate that the measurements that were mostly affected by the geomagnetic storm are located in the auroral region of North America. GRACE accelerometer measurements are processed according to Section 3.3 to generate differential acceleration (α_{dx}) estimates along the three axes, and are subsequently low-pass filtered and decimated to 16 s sampling interval to match the spacing of the ACE **B**-field sampling rate. Figure 3.8a displays α_{dx} and IMF estimates along the x-axis. α_{dx} estimates follow the ACE **B**-field measurements, especially in the auroral zone between 60°~75°. This intense space weather condition affected GRACE acceleration measurements and disturbed them in the range [-400, 400] nm/s^2. Subsequently, the α_{dx} and B_x signals are analyzed using continuous wavelet transformation (CWT) (Mallat, 1998). The CWT provides wavelet coefficients that are functions of scale and position by multiplying the integral of the signal with a scaled and shifted wavelet function, over the time/space domain. Let $f(t)$ be a signal. The CWT of $f(t)$ is given as follows:

$$W_{\psi}f(a,k) = \frac{1}{\sqrt{|a|}}\int_{-\infty}^{\infty}\bar{\psi}\left(\frac{t-k}{a}\right)f(t)dt, \tag{3.3}$$

where a is the scale of the wavelet function, k is the translation value, t is time and ψ is the mother wavelet that is a continuous function of time and frequency, and $\bar{\psi}$ is the dual function of ψ.

The cross wavelet applied to assess the similarity between two signals, x and y is given as follows:

$$W_{xy}f(a,k) = S(W_x^{*}f(a,k)W_y(a,k)), \tag{3.4}$$

where $W_x(a,k)$ and $W_y(a,k)$ are the CWT of the input signals x and y, respectively. W_x^{*} is the complex conjugate of W_x and S is a smoothing operator in time and scale expressed as:

$$S(W) = S_{scale}(S_{time}(W_n(f(a,k))), \quad (3.5)$$

where S_{scale} is the smoothing along the wavelet scale axis and S_{time} the smoothing in time. Note all these transformations are valid under the condition that the input signals are continuous and equally spaced. This is the reason the α_{dx} estimates need to be low-pass filtered, so that they match the time-spacing of ACE mission measurements.

Finally, the magnitude of the wavelet coherence that quantifies the correlation of the two-input series in the frequency domain is given as (Mallat, 1998):

$$C = \frac{\left|S(W_x^* f(a,k) W_y(a,k))\right|^2}{S(|W_x(a,k)|)^2 S(\left|W_y(a,k)\right|)^2}. \quad (3.6)$$

Figure 3.8b demonstrates nearly 85% coherence between the DM accelerations along the x-axis (α_{dx}) and B_x for various levels of decomposition in auroral and polar zones. This feature is clearly seen in the [16, 64] s interval. The arrows superposed on the coherence wavelet represent the local phase difference between the series and exhibit various characteristics. The arrows rotating from north to west and gradually towards south indicate a phase lead of B_x over GRACE trace. In our case the local phase delay in the area of interest is approximately 2.7^o.

In the sequel, we employ other external datasets that describe the dynamics of the magnetic field and we analyze the relationship between the two datasets (i.e., GRACE DM accelerations and magnetic field measurements).

3.5 GRACE and Poynting flux

A detailed analysis of the impact of the electromagnetic dynamics on GRACE is realized by employing electromagnetic currents captured by ground stations, distributed irregularly over North America and Greenland. A technique called spherical elementary currents systems (SECS) (Amm, 1997; Amm and Viljanen, 1999) transforms magnetic disturbance observations to equivalent ionospheric currents (EIC) provided by Weygand et al. (2011). EIC are electrical current linear densities in the horizontal direction expressed in Ampere per km (A/km), while spherical elementary currents (SEC) are electrical current surface densities in the vertical direction expressed in Ampere per squared km (A/km^2).

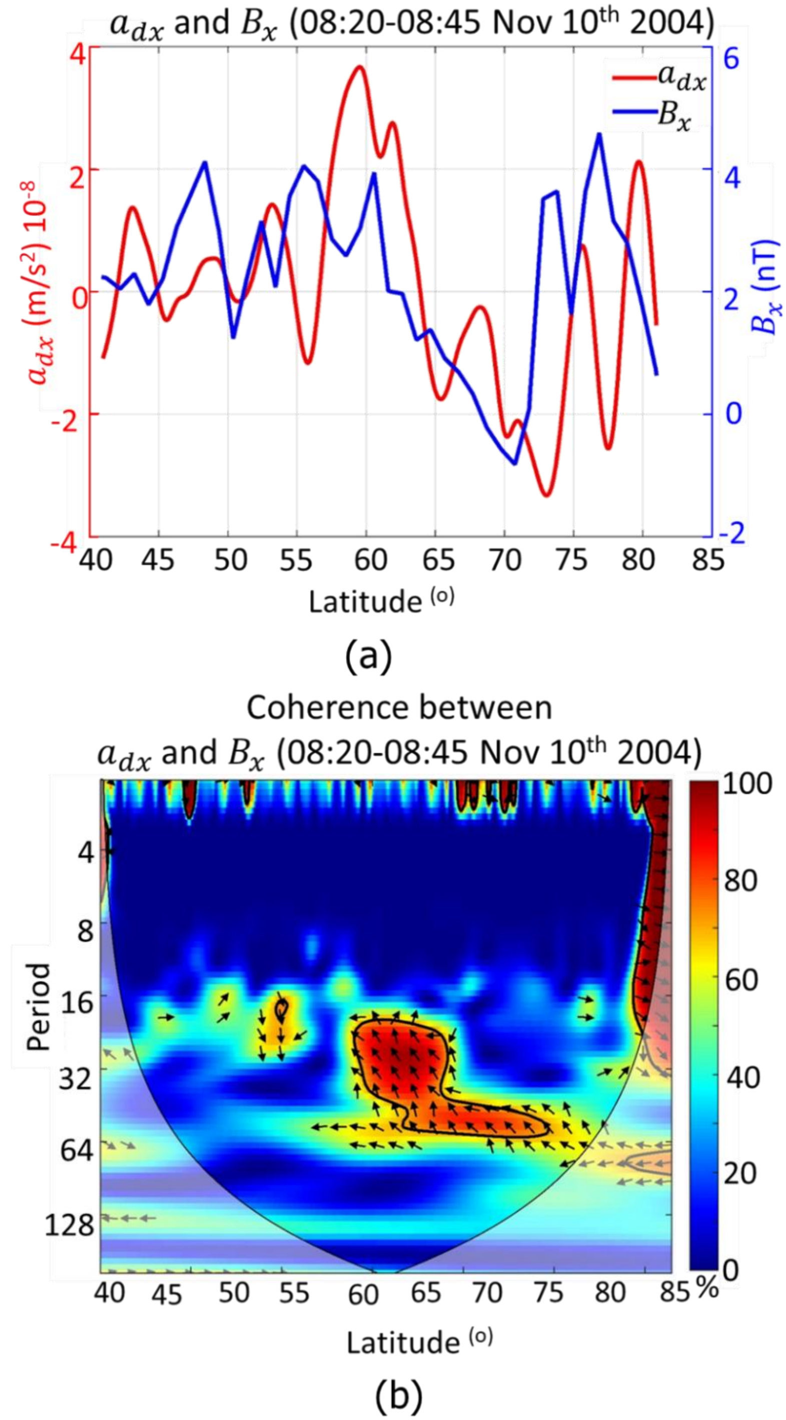

Figure 3.8: a) Red line indicates the longitudinal profile ($\lambda \approx 230^{\circ}$) of GRACE α_{dx} on November 10th 2004 at [08:20 08:45] UTC. Blue line shows the B_x derived from ACE in nT; b) CWT coherence between $\alpha_{dx}$and B_x. The arrows indicate the phase angle between the two-time series. The shaded area shows the cone of influence where edge effects become significant at different frequencies (scales).

The EIC and SEC values do not follow a regular spacing and are given at an altitude of 110 km at 10 s intervals; hence, a spatiotemporal interpolation is required to refer them to GRACE horizontal position (latitude and longitude). The choice of the interpolation technique is critical since the error in the gridded values can reach up to 15% in the vicinity of ground stations, when spacing is of more than a few hundred km (Amm and Viljagen, 1999). To avoid poorly gridded values, we examine the GRACE tracks over areas of dense ground station coverage (see Amm and Viljagen, 1999; Ince and Pagiatakis, 2016). Finally, we estimate the magnitude and direction of the electromagnetic energy flow described by the Poynting vector (**S**), which is the cross product of SECS ($\boldsymbol{E}$) and EIC ($\boldsymbol{H}$) and is given by Equation (3.7) (e.g., Kelley, 2009).

$$\boldsymbol{S} = \boldsymbol{E} \times \boldsymbol{H}. \tag{3.7}$$

The Poynting vector is the result of ionospheric electrical currents (moving charged particles) and not of neutral winds. Hence, in our analysis, we assess the impact of the electromagnetic energy input to GRACE accelerometers and not the impact of neutral wind kinetic energy exchange with the spacecraft.

Another lower scale geomagnetic storm (K_p= 6) occurred on October 11th, 2008. GRACE accelerometer measurements are used to create DM estimates. During this storm, the axis demonstrating the highest disturbance is the along-track axis (x-axis), which might be due to the direction of the currents (i.e., north to south direction), as illustrated in Fig 3.9b. In this case, a_{dx} has a phase lag of approximately 300 s in the time domain, however the signature of the disturbance is not very similar to the signature of the Poynting flux (see Figure 3.9c).

What follows is a case referring to a geomagnetic storm that began on March 10th, 2011 and lasted for approximately one day. That day, the ionosphere was disturbed by a geomagnetic storm of K_p= 6. Figure 3.10a visualizes GRACE differential accelerations along the x-axis and the Poynting flux. In this case, GRACE disturbances occur in the auroral and polar zones, which agrees well with findings from GOCE GGT response to geomagnetic storms (Ince and Pagiatakis, 2017). Additionally, the signature of the disturbance is very similar to the Poynting flux signature.

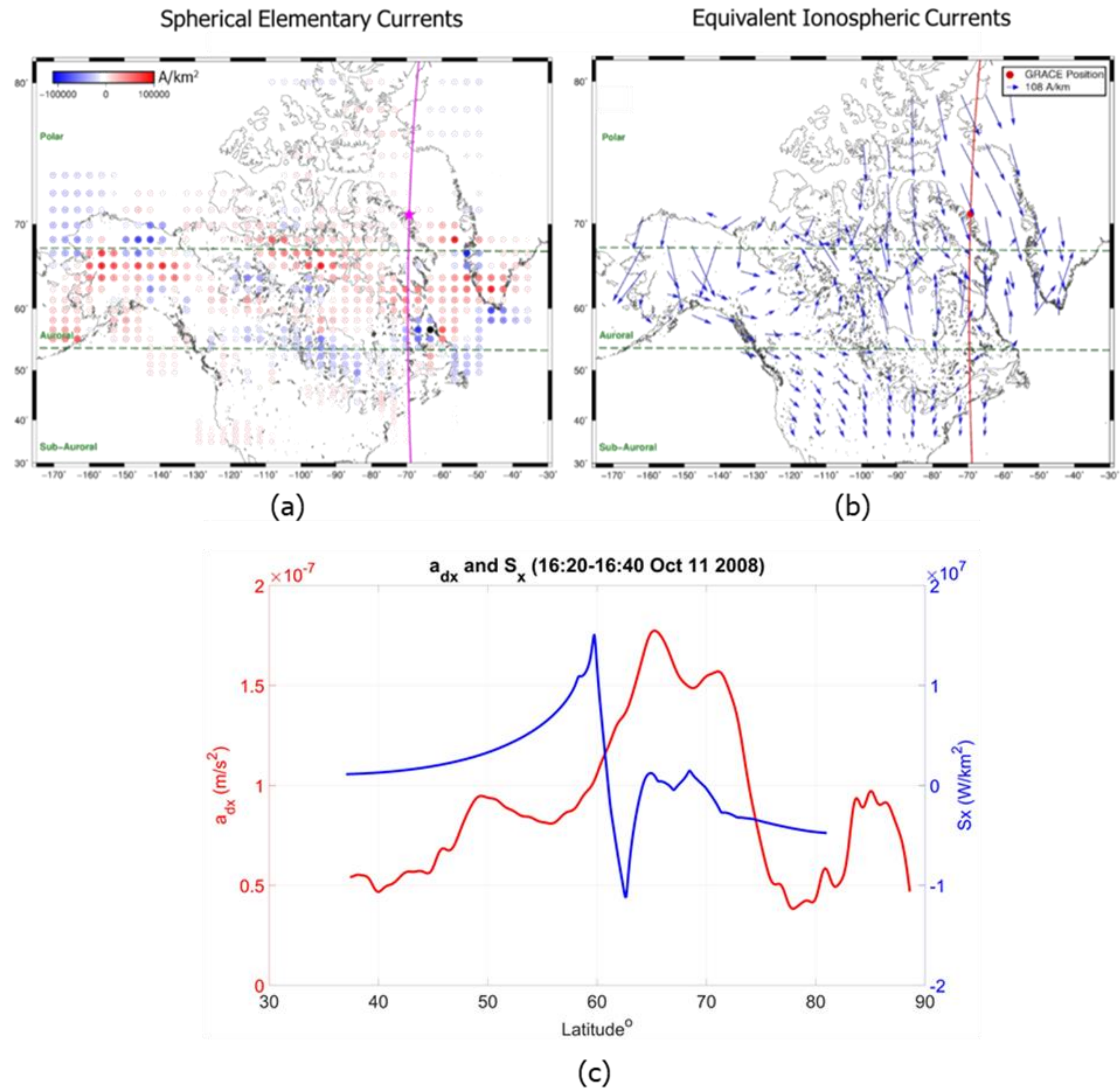

Figure 3.9: a) SEC estimates and GRACE ground track during October 11th 2008 at 13:15 UTC; b) EIC estimates and GRACE ground track during October 11th 2008 at 13:15 UTC; c) GRACE α_{dx} on October 11th 2008 at 13:15 UTC and Poynting flux estimates.

Finally, the magnitude of the disturbance ranges within ±400 nm/s^2. Notably, the wavelength of the disturbance is roughly half of Poynting flux wavelength. A strong coherence that reaches nearly 80%, between GRACE α_{dx} and Poynting flux is observed at medium to high latitudes (see Figure 3.10b).

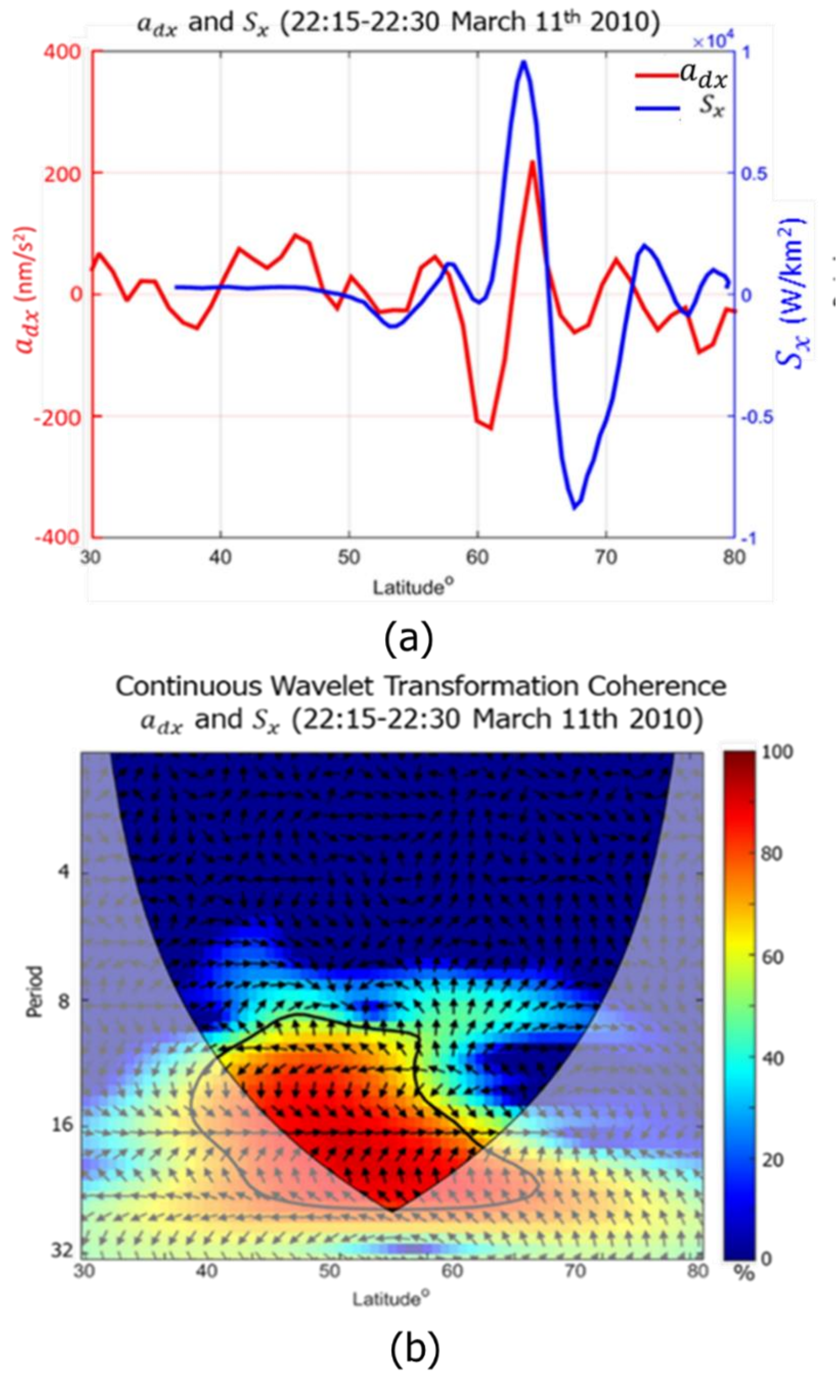

Figure 3.10: a) GRACE α_{dx} and Poynting vector (S_x) on March 11th 2011; b) CWT Coherence between GRACE $\alpha_{dx}$and Poynting flux. The arrows superposed indicate the phase angle between the two-time series. Black curve shows the cone of influence where edge effects become significant at different frequencies (scales).

Considering the analysis done with GRACE and Poynting flux estimates, it seems that the response of GRACE to geomagnetic storms is non-linear, as for each case phase (time lag) and the signature of the disturbance seem to follow a rather random pattern. Further analysis is required to validate the preliminary analysis conducted herein and in order to assess further the impulse response relationship between geomagnetic storms and GRACE instrumentation.

Other orbits have been also been investigated and, in many cases, there is a very low correlation between GRACE disturbances and the magnetic field disturbances. We therefore consider necessary further analysis in the topic of space weather dynamics and GRACE instrumentation response to these dynamics, to better capture their relationship.

3.6 Summary

In this chapter we assessed the impact of geomagnetic storms on GRACE on-board instrumentation. A new method that uses GRACE accelerometer measurements to estimate differential mode accelerations was introduced in order to get a better picture of the impact of neutral winds and charged particles on the mission's instrumentation. In Chapter 4, we will show that the idea of GRACE differential mode can be used in an innovative approach, that is, to derive gravitational gradients using GRACE Level 1B data.

4

GRACE-FO in gradiometer mode

In Chapter 3 we introduced a new technique called the “GRACE Differential Mode” to derive differential mode accelerations using GRACE on-board instrumentation. We now expand the concept of GRACE Differential Mode, aiming to derive gravitational gradients using GRACE. This Chapter is an unabridged version of the original research article *“Gravity Gradiometry with GRACE Space Missions: New opportunities for the Geosciences”* published in JGR: Solid Earth (Peidou and Pagiatakis, 2019), with minor edits to account for the different numbering of sections, equations, figures and tables, and with the addition of more results in Sections 4.2 and 4.3.

4.1 Introduction

In this Chapter, we address the question of how GRACE and GRACE-FO mission objectives may be enhanced by looking at the data processing methodologies and mathematical modelling from a different perspective. New methodologies may lead to discoveries, such as the detection of the Juan De Fuca ridge and increase the chance of breakthroughs in climate research. To this end, we attempt to develop a method that uses GRACE accelerometer, attitude and POD data as proxy for GRACE to derive gravitational gradients, similar to those of GOCE via a series of spatiotemporal transformations. Interestingly, an innovative, yet simple combination of Level 1B data from both GRACE satellites, named ‘gradiometer mode’ or ‘GRACE-GM method’ is shown to produce common and differential mode accelerations (CM and DM, respectively) as well as gravitational gradients that are directly comparable to those of GOCE.

The concept of satellite gradiometry using GRACE was initially suggested by Keller and Sharifi (2005). However, the suggested “gradiometer” was not used in practice (Casotto and Fantino, 2007), as it consisted of two accelerometers 220 ± 50 km apart (ibid, 2005) and only in one direction, namely, along the orbit. This long baseline violates the definition of the gradient and hence the estimated gradient cannot provide useful geophysical information. GRACE-GM surpasses this limitation by simply bringing the trailing spacecraft as close as possible to the leading spacecraft, a process described in Section 4.2. Moreover, the Keller and Sharifi (2005) method was developed to estimate only the first gradient of the GGT, while GRACE-GM can estimate the full GGT. Other proof-of-concept studies followed that used the theoretical "gradiometer" concept for the design of flight missions, but none of them has been practically applied due to the long baseline restrictions (Sneeuw et al., 2008).

GOCE DM accelerations and gravitational gradients (Level 1B) are used to validate GRACE-GM-derived equivalents for a period when the two missions were operating simultaneously, namely, in 2010. Analysis of the DM accelerations and gravitational gradients reveals the strong impact of the Earth's main magnetic field on both Low Earth Orbit missions. The two missions are subject to disturbances from the Earth's magnetic field, expressed through the magnetic field inclination and North and South Pole magnetic fluctuations.

In this contribution, emphasis is placed on showing the effectiveness and potential of the GRACE-GM concept for estimating gravitational gradients. Differentiating ourselves from GOCE-like follow-on missions currently being contemplated, we develop the GRACE-GM as an alternative methodology that will allow the recently launched GRACE-FO mission to be used in a dual mode perhaps without the need of a GOCE-FO or alternate missions. This study aims to provide a proof-of-concept of this original, yet very simple methodology, with the anticipation of improvements in the near future that will advance this method to be fully operational.

4.2 The concept of GRACE gradiometer mode

GRACE accelerometers measured the non-gravitational accelerations acting on the spacecraft. The accelerometers were located at the center of mass of each spacecraft to eliminate angular accelerations produced by attitude changes. In this study, Level 1B data, specifically found in GNV1B, ACC1B, and SCA1B data files (Case et al., 2010), are used to retrieve information about POD, non-gravitational accelerations, and spacecraft attitude. Acceleration measurements are band-pass filtered in the design band of the instrument (10^{-4}~10^{-1} Hz) with a Gaussian filter.

The differencing of the accelerations at a particular point in space is achieved by computing the time Δt the trailing satellite (hereafter B) takes to be in the closest distance, position-wise, to where A was Δt seconds earlier. The minimum distance is calculated using the Vincenty's formula, that is the minimum distance on the ellipsoid. Later, Δt is calculated using the minimum distance between the two spacecraft on the ellipsoid. This means that A(t) and B(t+Δt) will be in a very close position. Subsequently, we compute the separation vector between A(t) and B(t+Δt) from the POD. We then transform the accelerometer measurements of B($t + \Delta t$) into the accelerometer frame of A(t) via the attitude angle differences that occur in the time interval Δt, as described in Section 3.3. Once the accelerations of B(t+ Δt) are in the reference frame of A(t), they can be differenced along all three directions; the transformation of the frame of B to that of the identical satellite A adds the gravitational difference between A(t) and B($t + \Delta t$). The following four equations represent, the vector common and differential modes, the gradient of the gravitational potential in the x direction, and the cross-gradient of the gravitational potential in the xy direction, respectively. All quantities in the equations are referenced to the leading satellite A(t) (accelerometer) reference frame (SRF):

$$\boldsymbol{\alpha}_c(t) = \frac{1}{2}(\boldsymbol{a}_B(t + \Delta t) + \boldsymbol{a}_A(t)), \quad (4.1)$$

$$\boldsymbol{\alpha}_d(t) = \frac{1}{2}(\boldsymbol{a}_B(t + \Delta t) - \boldsymbol{a}_A(t)), \quad (4.2)$$

$$V_{xx}(t) = -2 \lim_{\Delta x \to 0} \frac{\alpha_{d_x}(t)}{\Delta x(t)}, \quad (4.3)$$

$$V_{xy}(t) = -2 \lim_{\Delta x \to 0} \frac{\alpha_{d_y}(t)}{\Delta x(t)} - 2 \lim_{\Delta y \to 0} \frac{\alpha_{d_x}(t)}{\Delta y(t)}, \quad (4.4)$$

where $\boldsymbol{\alpha}_c(t)$ and $\boldsymbol{\alpha}_d(t)$ denote the common and differential mode accelerations, respectively, $\boldsymbol{a}_A(t)$, $\boldsymbol{a}_B(t + \Delta t)$ represent the linear accelerations observed by A(t) and B(t+Δt), respectively, and where Δx and Δy are the distances between the two satellites along the x-axis and the y-axis, respectively. Other gradients are similarly defined (Stummer et al., 2012). The full tensor is defined as follows:

$$V = \begin{bmatrix} \frac{\partial^2 V}{\partial x^2} & \frac{\partial^2 V}{\partial x \partial y} & \frac{\partial^2 V}{\partial x \partial z} \\ \frac{\partial^2 V}{\partial x \partial y} & \frac{\partial^2 V}{\partial y^2} & \frac{\partial^2 V}{\partial y \partial z} \\ \frac{\partial^2 V}{\partial x \partial z} & \frac{\partial^2 V}{\partial y \partial z} & \frac{\partial^2 V}{\partial z^2} \end{bmatrix} = \begin{bmatrix} V_{xx} & V_{xy} & V_{xz} \\ V_{yx} & V_{yy} & V_{yz} \\ V_{zx} & V_{zy} & V_{zz} \end{bmatrix}. \quad (4.5)$$

The idea of GRACE-GM is valid under the following realistic assumptions:

a) The distance between A(t) and B(t+Δt) is very small, essentially approaching zero at the limit, compared with the size of the orbit. The distance between GRACE-A and GRACE-B doesn't exceed few km and therefore the assumption is clearly achievable and satisfies the definition of the derivative of a function (cf., Equation (4.3)).

b) Satellite B is Δt≈26 s on average behind A during which time the gravitational field does not change. Thus, the principle of Equation (4.2) is not violated and differencing the acceleration measurements between A(t) and B(t + Δt) at the position of A(t), results in realistic differential mode accelerations. The same assumption holds true when estimating common mode accelerations (cf., Equation (4.1)).

c) The dynamic regime in the thermosphere remains essentially unchanged within the 20-40 s interval between A and B and within a few to several tens of meters. The assumption is very realistic since an average spatiotemporal homogeneity of external atmospheric dynamics (i.e., neutral winds and plasma flux) is roughly 300 km in extent and lasts several minutes (Zhang et al., 2003).

d) The Earth's rotation during the time lag of Δt≈26 s corresponds to 11.96 km (estimated at the Equator). This spatial shift does not affect GRACE-GM gravitational signal as the spatial resolution of GRACE-GM is considerably lower.

Following the above assumptions, we are now in a position to describe the fundamental concept of the GRACE-GM method that allows the recovery of the gravitational signals despite the fact that each accelerometer measured only non-gravitational accelerations.

In order to understand the GM concept, the two fundamental characteristics of the GRACE constellation should be taken under consideration, namely (a) the spacecraft were identical and (b) they possessed an Attitude and Orbit Control System that provided three-axis stabilized Earth-pointing attitude control through sensors, actuators, and software (Herman et al., 2004).

According to the GRACE-GM concept, satellite B($t + \Delta t$) will be very close to A(t). However, B($t + \Delta t$) will have an attitude that will be different from that of A(t); that is, the three axes of the accelerometers of each spacecraft will not be aligned. Attitude changes of a spacecraft are introduced by torques due primarily to gravity gradients, aerodynamic drag, electromagnetic induction, and solar radiation pressure (e.g., Gerlach, 1965), among other causes. Due to assumptions (b) – (d) above, and the identical spacecraft, all non-gravitational torques will be nearly equal, except the gravity gradients at the positions of A and B. Equal gravitational gradients at each of A and B would introduce equal torques on each of the identical satellites; thus, we would observe identical attitude angles (roll, pitch, yow). By reciprocity, when rotating the axes of B($t + \Delta t$) to be aligned with that of A(t), it means that we actually add to the measured non-gravitational accelerations of B a small acceleration vector to equate the torques of A and B, leading to the alignment of the accelerometer axes of A and B. At this point, taking the difference of the accelerations along the aligned axes of the satellite frames, we estimate 3-D gravitational accelerations (DM), which when divided by their corresponding distances will provide the gravitational gradients at the barycenter between the twin satellites. In other words, by aligning the two satellite frames we create a system equivalent to GOCE in which the accelerometers are all aligned. This alignment is the necessary and sufficient step for estimating gravitational gradients.

One of course may wonder why we use only GPS precise orbits (POD) to determine the shortest distance (3-D components) of the two spacecraft and not the KBR (K-band Ranging) measurements that are more accurate. GRACE's core science instrument, namely, the KBR, measures the instantaneous 3-D distance between the two spacecraft in motion, but it cannot be used to provide gradients along each axis of the accelerometer frame of A(t). In addition, according to the differential method employed in this study, it turns out that satellite A's position is “frozen” in time, while B continues to move toward A. In this fictitious scenario, there are no KBR measurements during the time interval Δt in which satellite B is approaching A. The error introduced from the precise GPS and all the instruments employed in this method is assessed in Section 4.3.2, using the power spectrum density approach.

Figure 4.1 shows the procedure to derive gradients using GRACE Level-1B data. The input information comprises of the a) accelerometer (ACC); b) precise orbits (GNV) and c) star cameras assembly (SCA) measurements for each spacecraft (A or B). Additionally, the KBR measurements are used as a constraint for the minimum distance criterion. All the data are subject to a cubic spline interpolation that increases the sampling rate to 10 Hz. Of note is that GRACE-FO Level-1A data are given in 10 Hz intervals and therefore can be directly used without any interpolation (Wen et al., 2018). In order to find the minimum time lag (Δt) required for B to be as close as possible to A(t), the three-dimensional distance coming from GPS is used. Afterwards, all the measurements of GRACE B are transformed from SRF_B to SRF_A. Finally, the differential accelerations and the gravitational gradients are estimated and transformed from SRF_A to ENU. The mathematical formulation of this procedure is given in Equations (4.1)-(4.4).

Unlike GOCE, the GRACE-GM design does not allow for constant distance among the accelerometers. Hence, the calculation of every gravitational gradient along the orbit uses a different distance between the accelerometers. In fact, in Section 4.3.2, we argue that different distances constitute a powerful asset of GRACE-GM, as they eliminate aliasing and sample all the frequencies, providing multiscale 3-D gradients. The GOCE satellite orbited the Earth in a nearly polar, sun-synchronous dusk-dawn orbit (Rummel et al., 2002), designed to cross the Equator at 18:00 hours (ascending node) or 06:00 hours (descending node). The ascending tracks of GOCE were characterized as dusk tracks, and the descending tracks as dawn tracks. The GRACE mission also had a nearly polar orbit though, but as opposed to GOCE, it was not Sun-synchronous. Hence, ascending and descending tracks were independent of the local solar time. To be able to compare GOCE and GRACE-GM estimates, we separate all GRACE tracks into ascending and descending and we further classify them based on the local solar time of the spacecraft pass, in daytime and nighttime tracks, respectively. To achieve this classification, 24 time zones each spanning 15° (1 hr) are used. Subsequently, the GPS time and longitude of each measurement are employed to calculate the local time of the spacecraft pass.

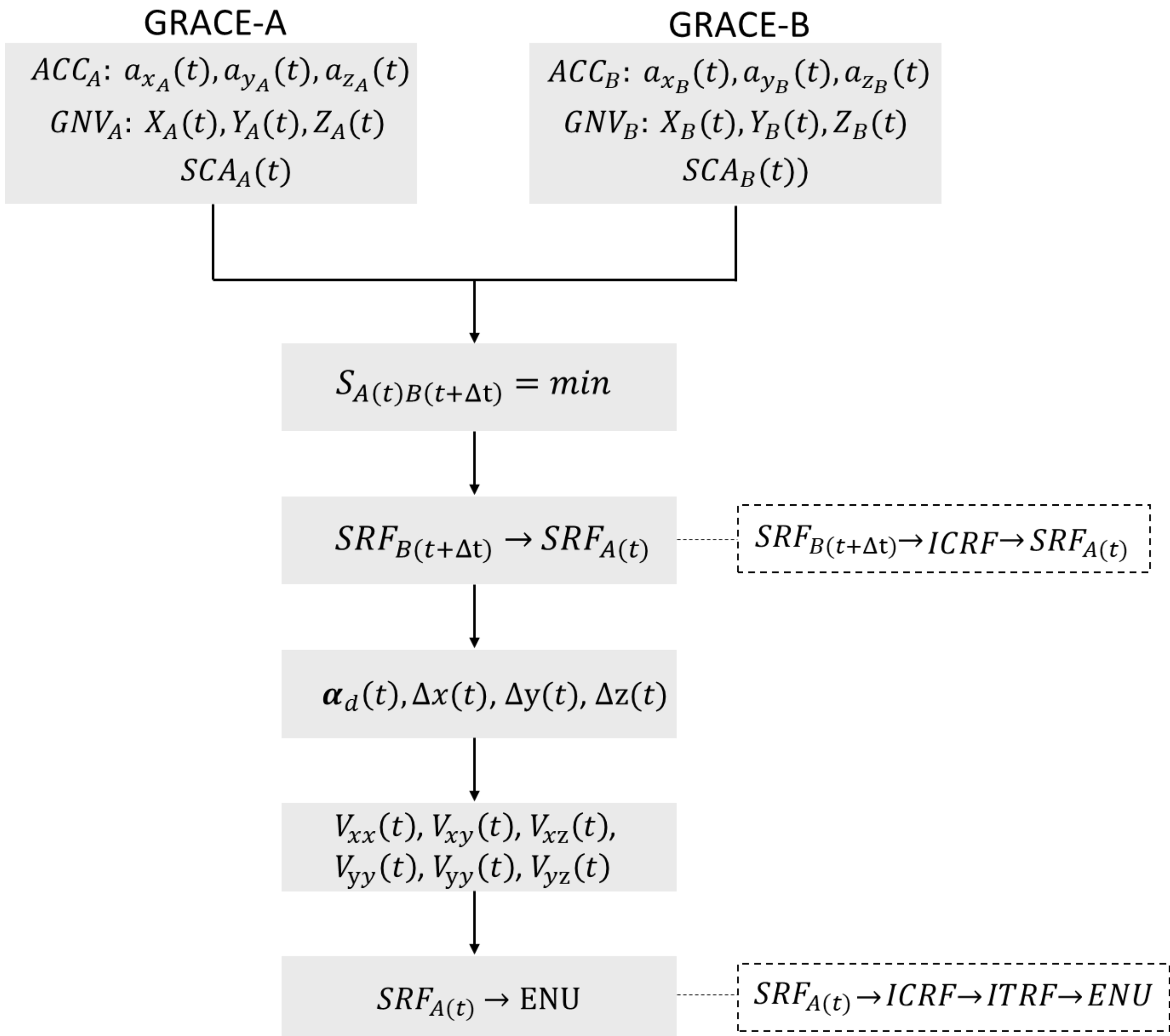

Figure 4.1: GRACE-GM methodology.

To remove any nonlinear accelerometer behaviour, GRACE accelerations are filtered in the passband of the instrument (0.1–100 mHz) and the GOCE measurements in the gradiometer's passband (5–100 mHz). Of note is the overlap of the two instrument bandwidths that is very advantageous in the inter comparisons. In both filtering processes, a simple Gaussian filter is used. Finally, to be able to compare results from the two missions, both GOCE and GRACE accelerations should be referenced to the same reference frame.

GOCE Level 1B measurements are referenced to the Local Orbital Reference Frame (ESA, 2006) and GRACE Level 1B measurements are in the so-called Satellite Reference Frame (SRF) (Case et al., 2010). Consequently, we transform both mission measurements to a common reference frame, namely, the East-North-Up system using the azimuth angle at each point of the satellite track.

GRACE differential mode (DM) accelerations are calculated using more than 5000 orbits over the period of 1 year (2010). Initially, we filter Level 1B non-gravitational accelerations, and afterwards we apply the GRACE-GM method as described in Section 4.2 and then we use GOCE East-North-Up Level 1B gradiometer measurements for the same period to validate the newly introduced method.

4.2.1 GRACE CM accelerations

Common mode accelerations (*cf.*, Equation (4.1)) are derived by averaging the non-gravitational accelerations to provide valuable information on the behaviour and the structure of these accelerations. We calculate common mode accelerations for the year of interest and we further investigate the non-gravitational sources that dominate the CM signal. GRACE CM accelerations reveal the strong fluctuations of the magnetic field over the North and South poles (see Figure 4.2). This finding agrees well with the results showed in Chapter 3, where the impact of geomagnetic storms on GRACE accelerometers was investigated. GRACE CM accelerations carry information on the non-gravitational forces acting on the GRACE system, as opposed to DM accelerations that are free from non-gravitational forces. To this end, the presence of the Earth's magnetic field on GRACE CM accelerations is expected. Previous studies addressed magnetic fluctuations in GOCE CM accelerations (Ince and Pagiatakis, 2016). These fluctuations (also known as magnetic ripples (Nakanishi et al., 2014)) are perpendicular to the geomagnetic field and have a spatiotemporal variability (ibid, 2014). Perturbations of these fluctuations on LEO satellites highly depend on the local time of the satellite pass (Nakanishi et al., 2014). GRACE CM accelerations demonstrate a strong presence of these fluctuations along track, which we attribute to the lack of drag compensation mechanism of GRACE. North and South Pole geomagnetic fluctuations (Figure 4.2) result in stronger perturbations in GRACE CM accelerations during daytime. The magnetic inclination is also evident in GRACE CM solutions, especially in the ascending nighttime tracks (Figure 4.2b). Additionally, the latitudinal linear feature at $\phi \approx 60^{o}$ that we attribute to Birkeland currents, peaks during ascending nighttime tracks as demonstrated in Figure 4.2b. Finally, the North and South Pole fluctuations evident in GRACE CM are also present in the cross-track measurements and mainly in the ascending GOCE CM tracks. Of note is that GOCE CM accelerations do not demonstrate any signal induced by the Earth's magnetic inclination. The different response of GOCE and GRACE CM accelerations might be attributed to technical specifications (i.e., mission's design and instrumentation) and to the different altitude of the two missions.

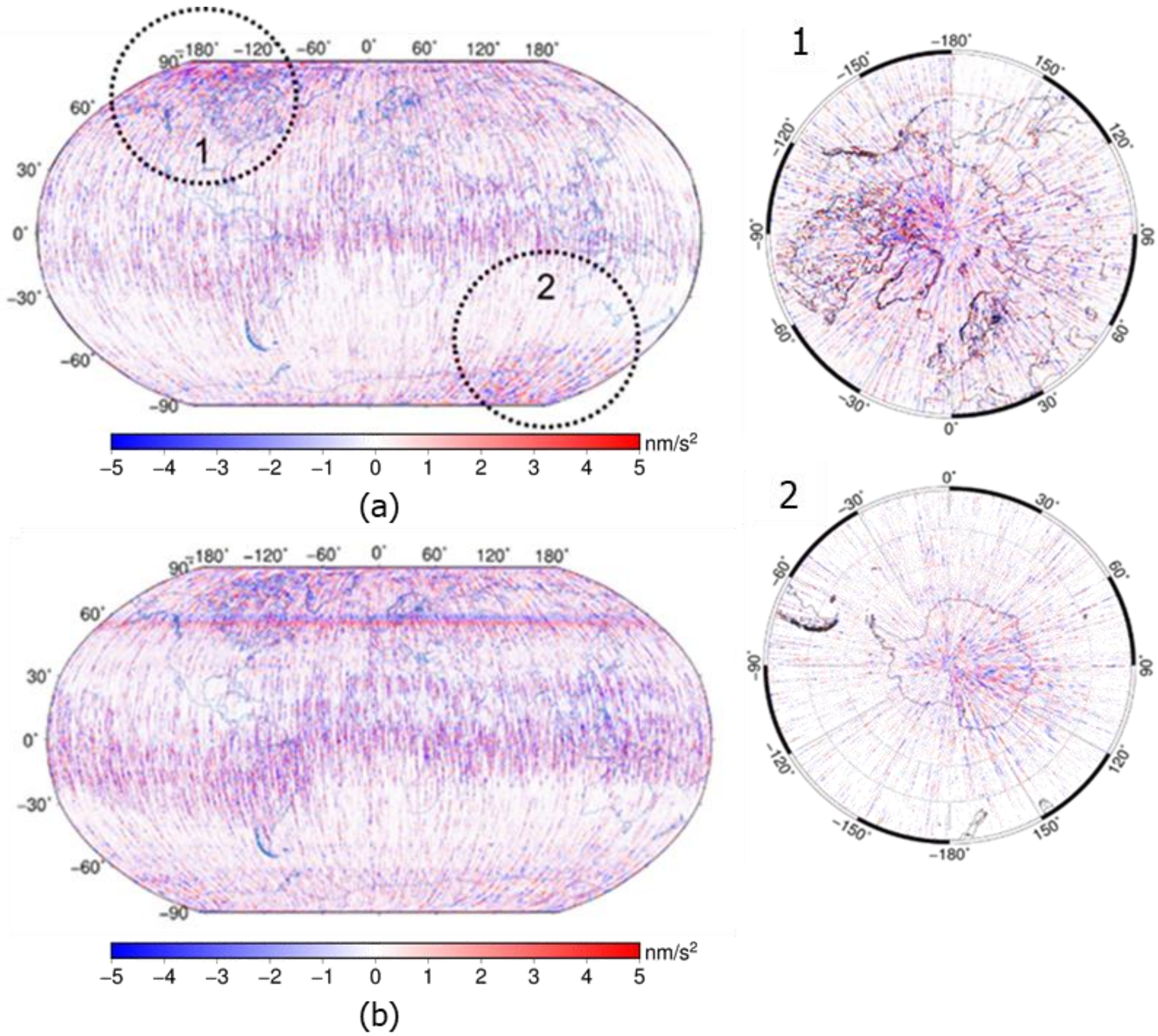

Figure 4.2: a) GRACE CM ascending daytime along the x-axis during 2010. Dashed circles indicate the areas 1 and 2 with magnetic fluctuations; b) CM ascending nighttime along the x-axis during 2010. Data have not been low pass filtered.

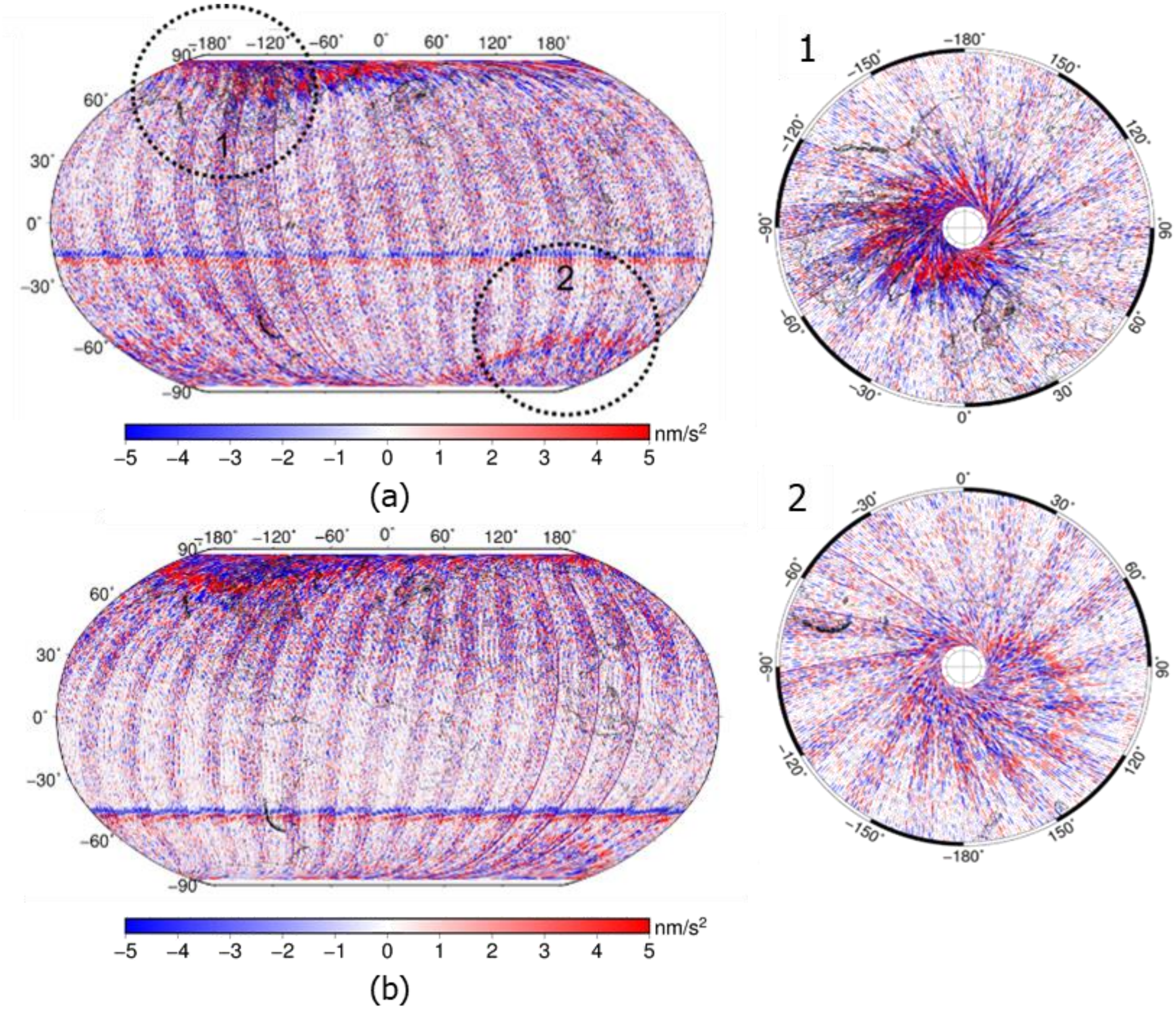

Figure 4.3: a) GOCE CM along the y-axis from ascending tracks. Dashed circles indicate the areas 1 and 2 with geomagnetic magnetic fluctuations; b) GOCE CM along the y-axis from descending tracks.

4.2.2 GRACE DM accelerations

Initially, we explore the ability to obtain differential gravitational accelerations (cf., Equation 4.2) from the non-gravitational accelerations measured by the two GRACE spacecraft during 2010. The currently available sampling rate of the data (1 Hz) is not adequate to determine the actual shortest distance between the twin satellites due to the average satellite speed of 7.6 km/s. To satisfy assumption (a), a higher sampling rate is required. For the purpose of this study, we interpolate both the position of the satellites and the accelerometer measurements to 10 Hz using cubic splines that provide minimum energy path. The same interpolation is also applied to all the measurements required by the GRACE-GM method (i.e., GNV1B and SCA1B). We emphasize that the interpolation process simply increases the sampling rate for the sole purpose of finding the minimum 3-D distance between A(t) and B($t + \Delta t$) that does not necessarily occur at integer seconds. This interpolation does not add any physical information. However, as this study serves as a proof-of-concept and focuses on validating GRACE-GM ability to estimate gravitational gradients, we apply interpolation to Level 1B measurements to find the minimum distance between the two spacecraft. GRACE-FO acceleration measurements have recently been available in 10 Hz (Level 1A) and there will not be any need for interpolation (Wen et al., 2018). Analyses of more than 5,000 orbits indicate that the typical shortest 3-D distance between the two spacecraft is within few hundred meters.

Although the magnetic field disturbances on GRACE are outside the scope of this study, we mention them briefly here because they are the "noise" and obscure the geophysical signals we are trying to identify. Derived GRACE differential mode (GRACE DM) maps along the x axis of the SRF (Figure 4.3) show the strong presence of the magnetic inclination signal over the equatorial region. Additionally, Figure 4.3b shows a negative to positive trend near $\phi = 60^{\circ}$N and $\phi = 75^{\circ}$S. This anomaly is present only in the ascending nighttime DM accelerations and appears to be highly correlated with the Birkeland currents, which are induced by the interaction of the Earth's magnetic field with solar winds (Friis-Christensen et al., 2017). The Birkeland currents become more intense when the radial component B_z of the Interplanetary Magnetic Field (IMF) becomes strongly negative (Friis-Christensen et al., 2017; Figure 1b), demonstrating high seasonal dependence (Anderson et al., 2018). We argue that the negative to positive perturbation on GRACE DM is induced by the Birkeland currents that reach their peak activity at local nighttime (Figure 4.4f). In the GRACE DM map, the trend is smooth and continuous because it shows the average annual perturbation of the currents.

As opposed to GRACE, GOCE followed a sun-synchronous dusk-dawn orbit that did not allow for ascending nighttime measurements any time after 6:00 pm, and therefore the Birkeland currents at $\phi = 60^{\circ}$N are not evident in GOCE DM accelerations. In addition, effects from the Earth's magnetic field fluctuations are also evident in all GRACE DM ascending tracks (Figure 4.4e) at the North Pole and are similar to the one seen in GOCE CM and GGM trace (Ince and

Pagiatakis, 2016; Figure 1). The above are new important discoveries arising solely from the GRACE DM and the separation of GRACE tracks into ascending and descending, as well as into daytime and nighttime tracks. Their rigorous study is currently underway and beyond the scope of this contribution.

GOCE DM accelerations also demonstrate a strong signal induced by the Earth's magnetic inclination. GOCE DM accelerations have been low-pass filtered (Bouman et al., 2011) and thus, they appear much cleaner than their GRACE equivalents (cf., Figure 4.5).

The presence of the Earth's magnetic field dominates both GOCE and GRACE DM accelerations, and as such, the geophysical signals are hardly visible. Further band-pass filtering has to be applied is addressed later. Interestingly, the magnetic inclination signal in GOCE measurements shows a latitudinal displacement between ascending and descending tracks, whereas this is not observed in GRACE. As shown in Figure 4.5, the signature of the magnetic inclination on a_{d_x} calculated from the ascending tracks is shifted nearly 30° to the north, and 30º to the south for the descending tracks, with respect to the magnetic Equator of the International Geomagnetic Reference Field model 2011 (IGRF11). Of note is that the spatial shift of the gradiometer measurements in ascending and descending tracks averages to the actual location of the magnetic inclination, to the best of our knowledge, the origin of this shift is unknown and has not been studied. On the contrary, the magnetic inclination signature of GRACE a_{d_x} appears to be consistent between the ascending and descending track, and there is not a clear distinction between positive and negative tilt of the magnetic field. Therefore, removing the magnetic inclination signal using the ratio between differential accelerations and IGRF11 will still leave minor leakages in the estimated differential accelerations, which will further contaminate the final gradients.

Additionally, as the GRACE-GM method implies the distance between the two spacecraft is highly variable and considerably longer (~100 meters on average) than that of GOCE accelerometer separation (0.5 m). As a result, GRACE DM accelerations are expected to have higher magnitude than those of GOCE, as well as possessing a rather arbitrary character due to the various distances used during the differential mode methodology (see Figures 4.4 and 4.5).

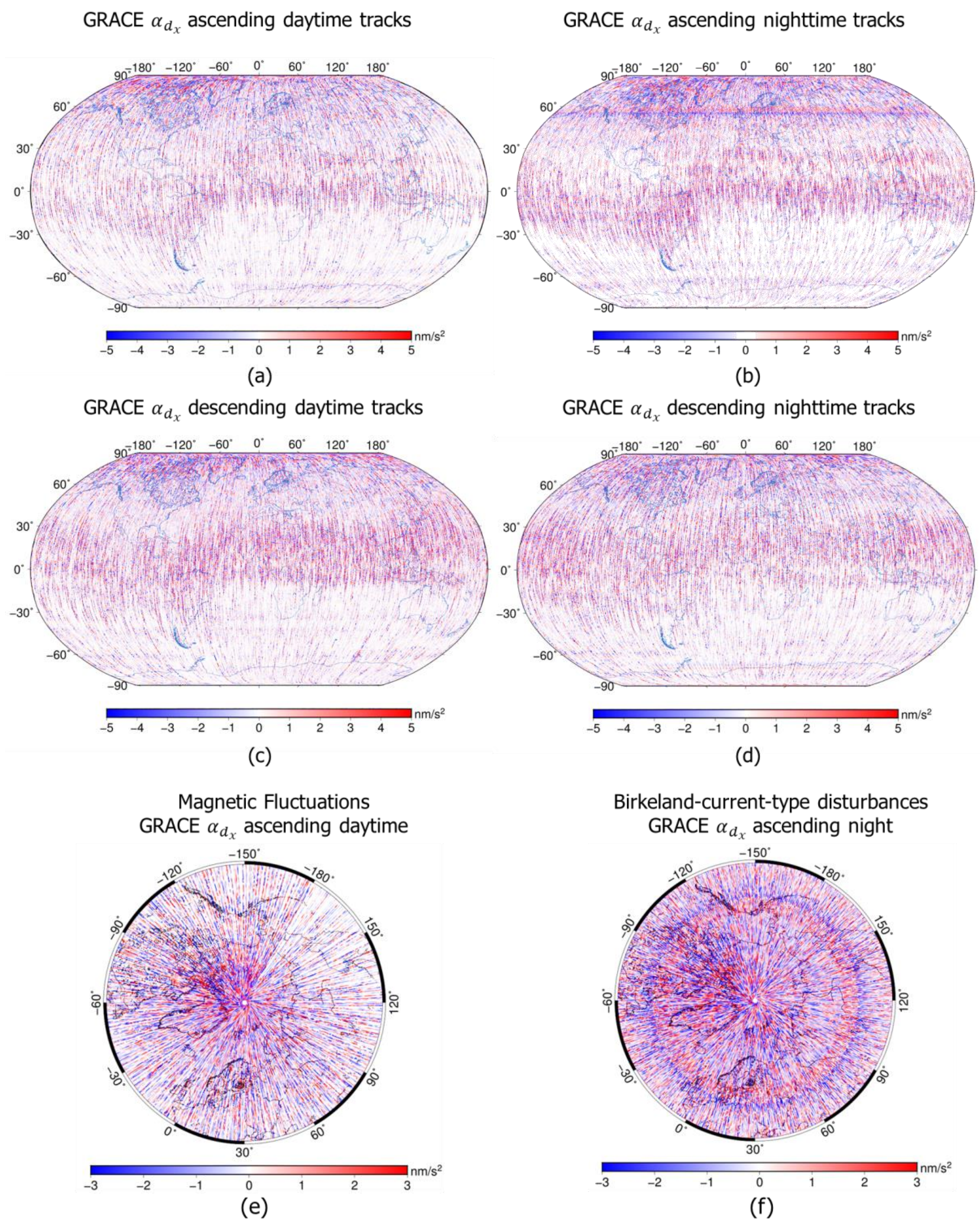

Figure 4.4: GRACE DM accelerations along the x-axis in 2010. Note the negative to positive trend at nearly $\phi = 60^{\circ}N$ (panel b). Polar plot of GRACE DM accelerations along the x-axis denotes the magnetic fluctuation disturbances (panel e). The negative to positive trend at nearly $\phi = 60^{\circ}N$ (panel f) resembles the average Birkeland currents in 2010. The x-axis denotes the along-track direction in the SRF.

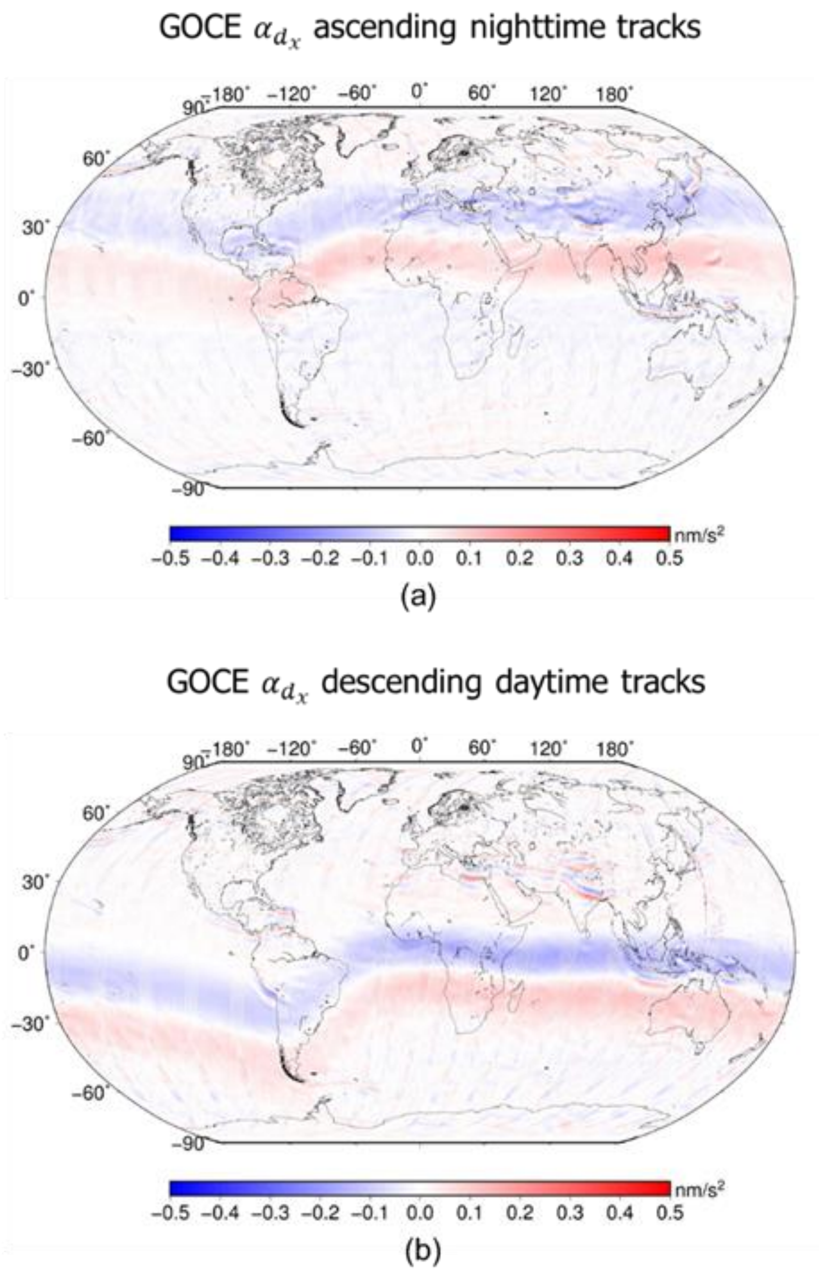

Figure 4.5: GOCE DM accelerations along the x-axis in 2010. Data used for these figures were taken from EGG_NOM_1b solutions.

4.3 GRACE gravitational gradients

Gravitational gradients represent the spatial variability of gravitational acceleration. They form the six components (i.e., $V_{xx}, V_{yy}, V_{zz}, V_{xy}, V_{xz}, V_{yz}$) of the gravitational gradient tensor (GGT), comprising the second derivatives of the gravitational potential V in the satellite (instrument) reference frame. Subscripts of V indicate the axes. The GOCE mission measured global gravitational gradients at 225–255-km altitude (Bouman et al., 2011), which have been used for regional-scale (>80 km wavelength) geophysical applications. With the end of the GOCE mission in November 2013, we are experiencing a gap of unknown duration in the availability of the global gravitational gradients. New missions, such as the mass variation observing system by high-low inter-satellite links (MOBILE), have been suggested and new configurations and concepts for high-accuracy gravitational models being examined (Hauk and Pail, 2019).

The concept of GRACE-GM can be used for estimating gravitational gradients by employing the acceleration vector $\boldsymbol{\alpha}_d$, the attitude differences between the two spacecraft and the corresponding nonstationary separation vector $\Delta\boldsymbol{r}$ between A(t) and B(t+Δt) (cf., Equation (4.3)). For the year of interest, more than 350 million points that cover the entire Earth's surface are generated. The distribution of distances over the year 2010 resembles a Gaussian-like distribution in the interval [0.01, 7.5] km comprising about 70% of the distances whereas outside this interval, the two tails are nearly uniform and comprise the rest of the distances. The mean value of the distances throughout 2010 is 3.2 km and their standard deviation is ±1.5 km. Should higher sampling rate Level 1B measurements be available, the "shortest" distances will decrease.

The abundance of GRACE-GM points leads us to believe that the concept of using GRACE-GM variable distances is analogous to multispectral imaging. In this respect, as a specific image can be seen in different spectral bands, the gravitational signal can be sensed by GRACE-GM in different multiwavelength bands. Specific results regarding these two concerns are presented in Section 4.3.2. We also present, in a first step, a qualitative or visual assessment of the results. A quantitative investigation is presented in Section 4.3.2.

One of the challenges of GRACE-GM is estimating the magnitude of the error of the final gradients. GRACE Level 2 solutions use the very accurate KBR system for measuring the distance between the two spacecraft. However, deriving the full GGT requires the use of GPS precise orbits for the distance calculation while the accuracy of GPS is at ~1 cm level (Kang et al., 2006. Additionally, the accumulated errors from the key instruments used for GRACE-GM are accumulated to the final gradients. In Section 4.3.2, we present a realistic estimate of the expected errors in the GRACE-GM gradients using frequency domain analysis of the GGT trace.

4.3.1 GRACE and GOCE GGT comparisons – Qualitative Assessment

To validate GRACE gradients, we employ the corresponding GOCE gradients after we process the gradiometer signal as described in Section 4.2. One may question the legitimacy of this comparison when the two missions had markedly different nominal altitudes, namely, 500 km of GRACE versus 250 km of GOCE. It is well known that the gravitational gradient diminishing factor with altitude is counteracted by the differentiation factor, and thus, the gravitational gradients possess a unique property compared to the other gravitational functionals in that, they are by far less attenuated with altitude, as shown in Equation (4.6) for the gravitational gradient along the z axis (see also, ESA, 1999; Equation (2.2.6)).

$$V_{zz} = \frac{\partial^2 V}{\partial z^2} = \frac{GM}{R} \sum_{n=0}^{L} \frac{(n+1)(n+2)}{R^2} \left(\frac{R}{r}\right)^{n+3} \sum_{m=-l}^{n} \sum_{k=-l}^{n} K_{nm} F_{nmk}(I) \exp[(i(ku + m\Lambda)], \quad (4.6)$$

with G being the gravitational constant, M the mass of the Earth, R being the Earth's mean radius, n the spherical harmonics degree and m the spherical harmonics order, L the truncation degree (maximum degree); K_{nm} the series coefficients in the complex form, F_{nmk} the inclination functions, I being the orbit inclination, Λ the difference in longitude between the Greenwich meridian and the longitude of the ascending node and u being the argument of latitude of the satellite in the orbit plane (Kaula, 1966). The term $\left(\frac{R}{r}\right)^{n+3}$ describes the field attenuation with respect to the altitude and the term $(n+1)(n+2)$ is known as the "differentiation factor" that counteracts with the field attenuation factor (ESA, 1999). Quantitative assessment of the attenuation of gradients is presented in Section 4.3.2.

Figure 4.6 shows the global maps of GRACE-GM gradients (V_{NN}, V_{EE}, V_{UU}) derived using measurements during 2010. The estimated gradients are highly noisy in the high frequencies, and therefore a low-pass filter is applied to supress the noise. This noise appears to be correlated with the magnetic field disturbances on GRACE instrumentation as discussed in Chapter 2. However, even after filtering the GRACE-GM maps look far noisier than GOCE especially in the zone along the latitudes ranging between $[5^\circ, 30^\circ]$S.

In order to test the efficiency of GRACE-GM to capture real signal locally, let us zoom in various areas known to have strong geophysical signals such as the Himalayas (Figure 4.7), the Indonesian ridge (Figure 4.8) and Canada (Figure 4.9). It appears that GRACE-GM performs well in zoom-in areas with known geophysical signals, albeit some regions are not very well mapped by GRACE-GM.

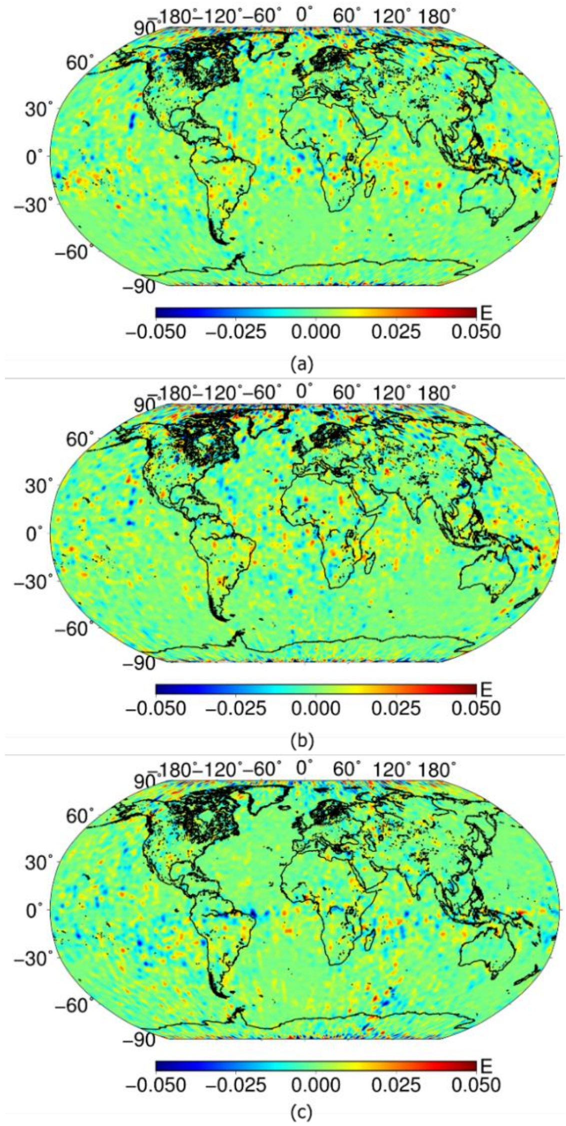

Figure 4.6: a) Global map of GRACE-GM V_{NN} component subject to a Gaussian low pass filter with 400 km half wavelength cut-off frequency during 2010; b) Global map of GRACE-GM V_{EE} component during 2010 subject to a Gaussian low pass filter with 400 km half wavelength cut-off frequency; c) Global map of GRACE-GM V_{UU} component subject to a Gaussian low pass filter with 400 km half wavelength cut-off frequency during 2010. GRACE-GM gradients have been interpolated every 0.1° using kriging interpolation.

The signals from both missions are subject to Gaussian low-pass, along-track filtering with a cut-off frequency corresponding to 400 km half wavelength to eliminate the long-wavelength magnetic inclination signal. We examine areas with characteristic geophysical signals attributed to active lithospheric regimes, namely, the Himalayan and Indonesian regions.

We juxtapose GOCE and GRACE gradients and we focus on identifying similar signatures. The results have been derived from ascending tracks. Descending tracks show very similar results and are not discussed here. Figure 4.7 displays the gradients from GOCE (left panels) and GRACE (right panels) over Himalaya.

Figure 4.7a displays GOCE V_{NN}; the geophysical signal induced by the Himalayan formation (Hetényi et al., 2016) alternates from positive to negative patches and peaks between $\phi = [25^{\circ}, 35^{\circ}]$N. A similar trend is evident in GRACE V_{NN} estimates shown in Figure 4.7b; the positive to negative patches peak between $\phi = [20^{\circ}, 30^{\circ}]$N.

Figures 4.7c and 4.7d display GOCE and GRACE V_{EE}, respectively. The distinct geophysical signal in GOCE (cf., Figure 4.7c) is evident in higher latitudes between $\lambda = [70^{\circ}, 80^{\circ}]$E and the positive to negative patches have a south-east orientation. GRACE V_{EE} demonstrates the same behaviour shifted to lower latitudes between $\lambda = [90^{\circ}, 110^{\circ}]$E. Of note is that GRACE V_{EE} geophysical signal has the same orientation (south-east) as GOCE. We attribute the spatial shift of the signals, to GOCE characteristic spatial shift between ascending and descending tracks discussed in Section 4.2.2.

Interestingly, a slightly different signature between V_{UU} components is depicted in Figures 4.7f and 4.7e. GRACE-GM depicts the underground water deficit over northern India (Rodell et al., 2009; Chen et al., 2014) (Figure 4.7f), while GOCE does not (Figure 4.7e). This finding further supports the capability of GRACE-GM in depicting gravitational gradients induced by geophysical signals. A good agreement between GOCE and GRACE V_{NE} is also demonstrated in Figures 4.7g and 4.7h, respectively. GRACE positive to negative patches show the same signature as GOCE. The signal has a south-east orientation in both cases, but GRACE displays longer wavelength.

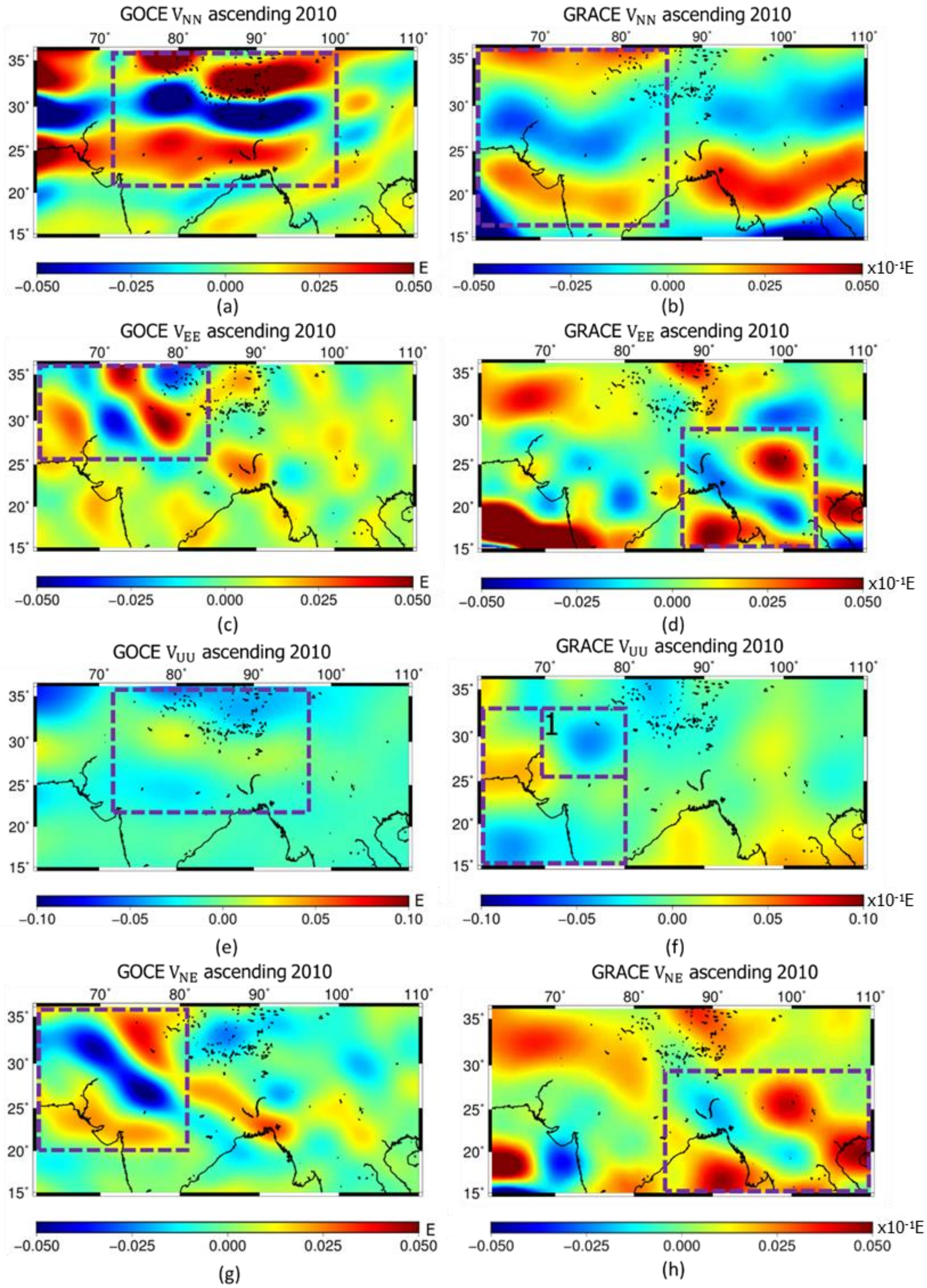

Figure 4.7: Geophysical signals from GOCE and GRACE gradients derived from ascending tracks over Himalayas. Purple dashed rectangles highlight the areas with the geophysical signal; The Indian groundwater deficit area is depicted in Area 1 of Figure 4f; GOCE and GRACE-GM gradients have been interpolated every 0.1° using kriging and have been subject to Gaussian low pass filtering with 400 km cut-off frequency.

The Indonesia region abounds with subduction processes caused by the Earth's mantle mass redistribution (Panet et al., 2014) and gravitational gradients are often used to investigate these interior processes. Figure 4.8 displays GOCE (left panels) and GRACE (right panels) gradients from ascending tracks.

Figure 4.8a displays GOCE V_{NN}. The geophysical signal induced by the subduction processes (Panet et al., 2014) in the area follows a longitudinal direction and transitions from positive to negative, dominantly for $5^{\circ} < \phi < 20^{\circ}$N. GRACE V_{NN} estimates (Figure 4.8b) depict a similar pattern. GOCE gradients are of higher spatial resolution showing shorter-wavelength signal transitions than those of GRACE, which senses only the longer-wavelength component of the geophysical signal. The difference in spatial resolution is expected due to the longer baseline of the GRACE "gradiometer". Due to the nature of the signal (east-west direction), V_{EE} does not demonstrate any particular behaviour in GOCE or GRACE-DM gradients. Nonetheless, diagonal features with positive to negative transition can be seen in both Figure 4.8c and 4.8d.

V_{UU} shows a negative to positive longitudinal pattern for GOCE and a slightly diagonal pattern for GRACE-GM. GOCE V_{NE} depicts many short wavelength negative-to-positive patches with random orientation, which agrees well with GRACE V_{NE} estimates that demonstrate a similar pattern of longer wavelength. The agreement of GOCE and GRACE gradients both in magnitude and signature offers substantial evidence that GRACE-GM can be a promising complement to GOCE mission for gravity gradient estimation.

The spatial shift of GOCE and GRACE-GM gradients is evident in almost all solutions. GOCE gradient signs and spatial shift also depend on the type of the track; however, GRACE-GM is shown to be totally independent of the orbit direction. Figure 4.9 displays the V_{NN} component of all tracks combined for the Indonesia area. GOCE V_{NN} magnitude is considerably smaller and in certain areas (e.g., see the dashed rectangle in Figure 4.9a), it changes its sign when all the tracks are combined. In fact, similar to the differential accelerations, the GOCE ascending and descending gravitational gradients counteract. On the contrary, Figure 4.9b demonstrates that GRACE-GM is less affected when combining all the orbits.

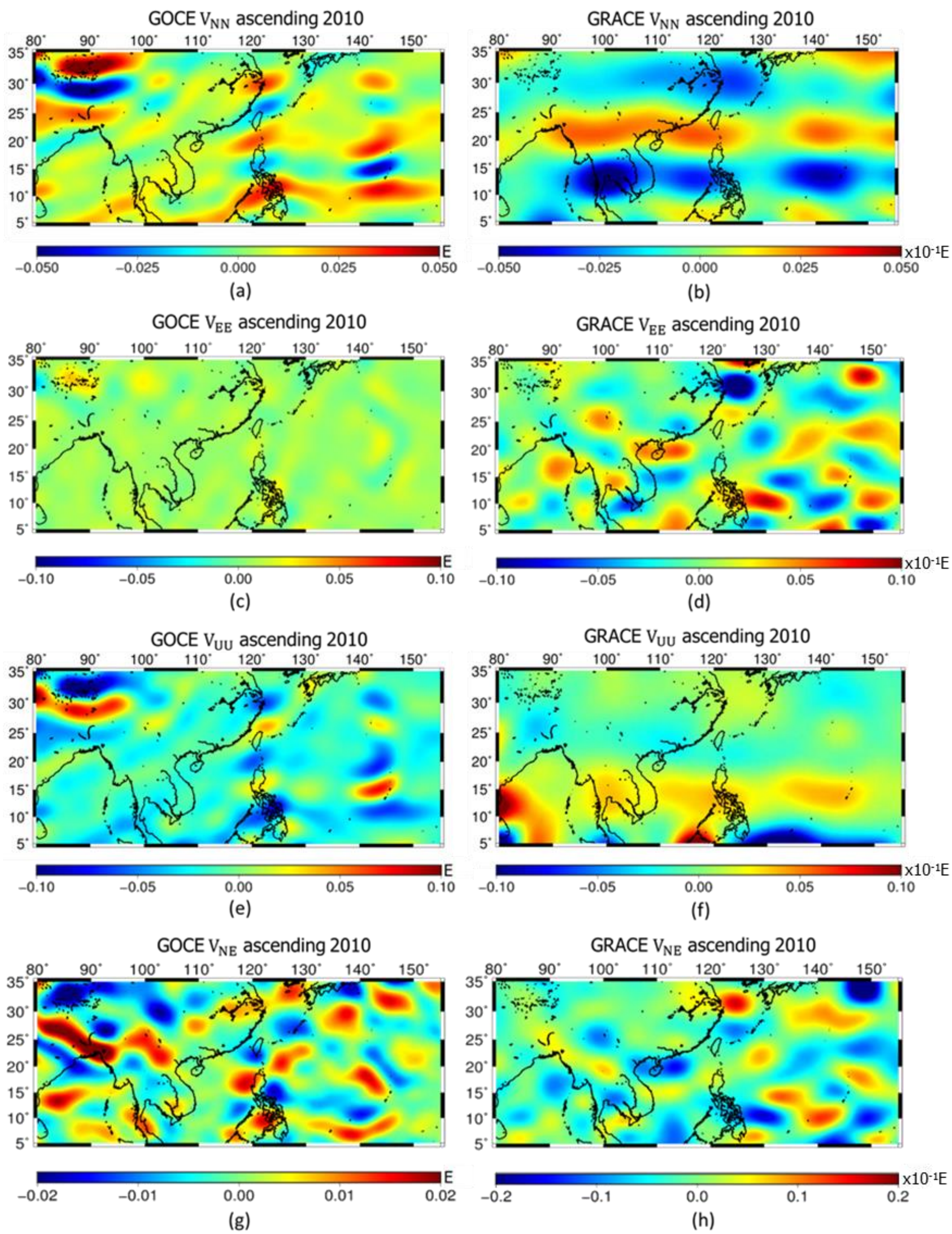

Figure 4.8: Geophysical signals from GOCE and GRACE gradients derived from ascending tracks over Indonesia. Note the different scale between GOCE and GRACE V_{NE} gradients. GOCE and GRACE-GM gradients have been interpolated every 0.1° using kriging and have been subject to Gaussian low pass filtering with 400 km cut-off frequency.

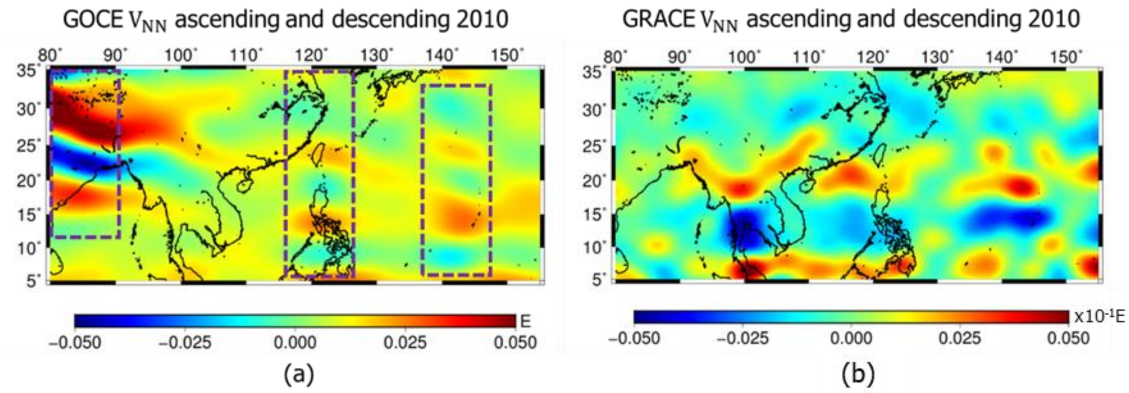

Figure 4.9: a) GOCE V_{NN} calculated using both ascending and descending tracks during 2010; b) GRACE V_{NN} calculated using both ascending and descending tracks during 2010. Dashed rectangle demonstrates the areas that GOCE V_{NN} sign changes when descending tracks are added. GOCE and GRACE-GM gradients have been interpolated every 0.1° using kriging and have been subject to Gaussian low pass filtering with 400 km cut-off frequency.

Finally, we argue that GRACE-GM can be used complementary to GOCE, for depicting geophysical signatures. In Figure 4.10, we juxtapose GOCE and GRACE-GM V_{NN} over Canada. GOCE gradients demonstrate a pattern with unclear geophysical signals, for instance, in Hudson Bay (dashed area 1), Baffin Bay (dashed area 2), and Greenland ice sheet (dashed area 3). On the contrary, GRACE-GM, due to its multiband nature, clearly maps all the geophysical signals in the continental margin of the Laurentian Plateau (Canadian shield) and specifically in the Hudson Bay area. The negative signal around Hudson and Baffin Bays indicates loss of mass (Sasgen et al., 2012), and the positive signal in the middle of the Hudson Bay indicates gain of mass presumably coming from the influx of the mantle that fills the void created by the uplift (Milne et al., 1999). In addition, GRACE-GM depicts the strong negative signal induced by the Juan de Fuca ridge (denoted with a star) that subducts under Vancouver Island and inland.

To further check the ability of GRACE-GM to recover useful gradients, we compare GRACE-GM V_{rr} with the one derived from the GRACE spherical harmonic coefficients (Level 2) at satellite altitude. However, this comparison may not be ultimate or even fair, because the Level 2 GRACE gradients have not been derived directly from the measurements with minimal processing. Rather, they are the product of numerous processing levels and constraints (i.e., different processing schemes and tunings are usually applied to derive Level 2 solutions using Level 1B measurements).

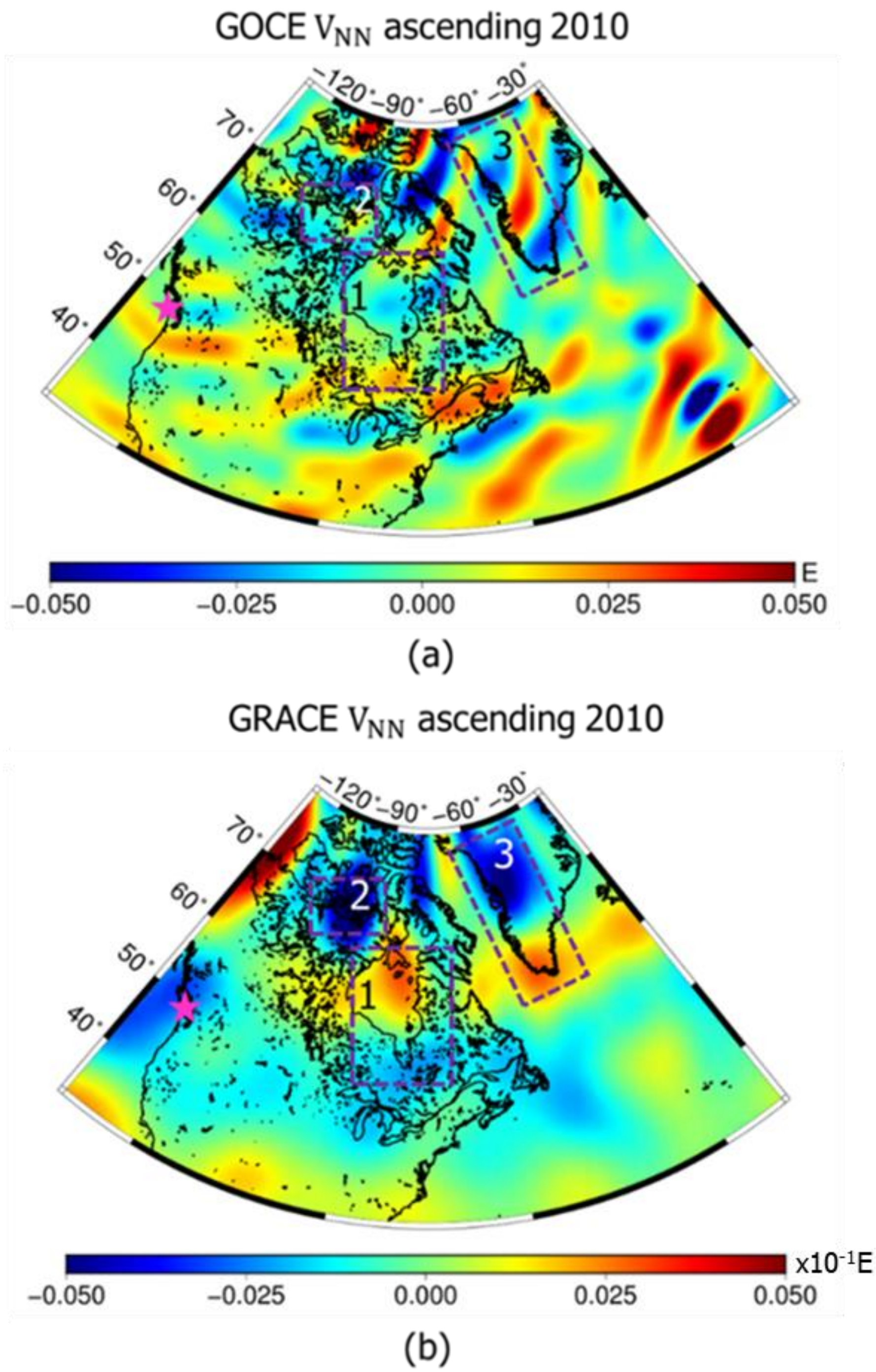

Figure 4.10: a) GOCE V_{NN} calculated using ascending tracks during 2010; b) GRACE V_{NN} calculated ascending tracks during 2010. Dashed areas depict 1) Hudson Bay; 2) Baffin Bay and 3) Greenland. The purple star shows the region of Juan de Fuca ridge. GOCE and GRACE-GM gradients have been interpolated every 0.1° using kriging and have been subject to Gaussian low pass filtering with 600 km cut-off frequency.

Additionally, the gradients derived from the two techniques have different spatial resolution, and therefore, for this comparison, the GRACE-GM solution is filtered accordingly to match GRACE Level 2-based wavelengths. Figure 4.11 displays the radial gradient (V_{rr}) over the Indonesian region estimated from GRACE CSR RL05 April 2010 monthly solution (Figure 4.11a); GRACE GGM05S static solution (Figure 4.11b); and GRACE-GM V_{rr} using Level 1B measurements during April 2010 (Figure 4.11c). The coherence between GGM05s and GRACE-GM V_{rr} is nearly 75%.

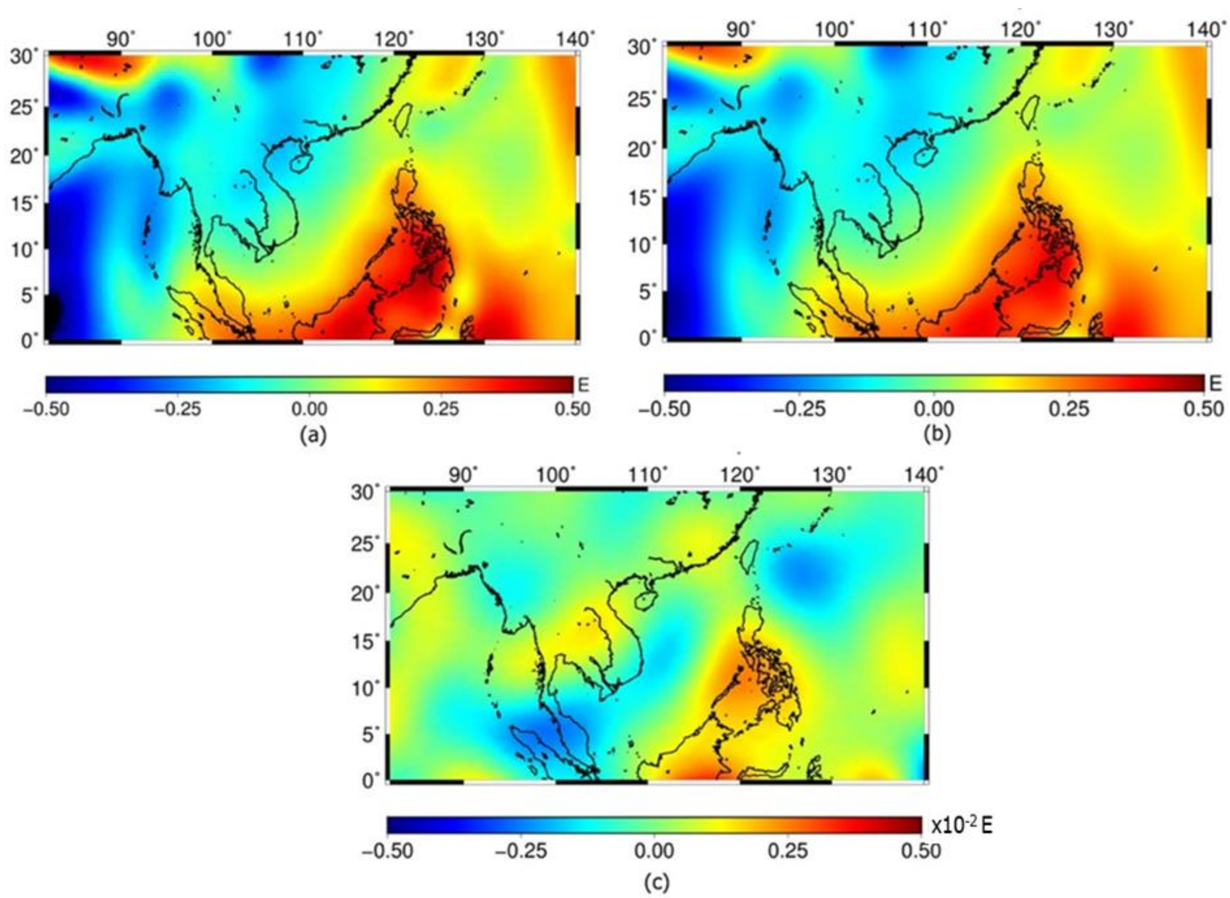

Figure 4.11: a) GRACE CSR RL05 April 2010 V_{rr}; b) GGM05S V_{rr}; c) GRACE-GM V_{rr} during 2010 over Indonesia; Note that all the solutions refer to 450 km altitude. GRACE-GM (c) has been interpolated every 0.1° using kriging and have been subject to a Gaussian filtering with 600 km cut-off to match (a), (b), solutions wavelength.

We now assess the power distribution of GGM05S and GRACE-GM gradients using wavelet multiresolution analysis. Wavelet transformation is a powerful method for signal analysis and decomposition, as it allows short-duration signal detection in both space and frequency domains.

For this analysis, the discrete wavelet transformation (DWT) is applied to the input data (GGM0S5 and GRACE-GM gradients). The DWT can analyze the gradients into various levels (bands) of decomposition, each of them corresponding to a different spatial resolution (or equivalently, spherical harmonic expansion) and has been successfully used in other studies of the gravity field (Fengler et al., 2007; Peidou et al., 2018). Prior to applying wavelet decomposition, the gradients must be gridded. We apply kriging interpolation to the GRACE-GM gradients with 0.1 degree grid step. Now, let us briefly visit the discrete wavelet transformation. The wavelet scaling function $\varphi(x)$ is used to compute the approximation or low-pass wavelet coefficients is given by the following Equation (Mallat, 1999):

$$\varphi(x) = \sqrt{2}\sum_{k\in\mathbb{Z}} h_k \varphi(2x - k), \quad (4.7)$$

where $\{h_k\} \in l^2\mathbb{Z}$ are the approximation or low-pass wavelet coefficients; k is an integer index for the scale of the scaling function; x denotes distance; and $\sqrt{2}$ maintains the norm of the scaling factor by a factor of two.

The mother wavelet function $\psi(x)$ is used to compute the detailed or high-pass coefficients is given as follows:

$$\psi(x) = \sqrt{2}\sum_{k\in\mathbb{Z}} g_k \psi(2x - k), \quad (4.8)$$

where $\{g_k\} \in l^2\mathbb{Z}$ are the detailed or high-pass wavelet coefficients. These functions are used in the analysis of a decomposition of a two-dimensional signal.

The representation of the gridded (x,y) gravity gradients along the north direction (V_{NN}) in the wavelet domain is given by:

$$V_{NN} = \sum_{k_x\in\mathbb{Z}}\sum_{k_y\in\mathbb{Z}} cA^{j}_{k_x,k_y}\varphi_{j,k_x,k_y}(x,y) + \sum_{i=H,V,D}\sum_{j=0}^{n}\sum_{k_x\in\mathbb{Z}}\sum_{k_y\in\mathbb{Z}} cD^{j,i}_{k_x,k_y}\psi^{i}_{j,k_x,k_y}(x,y), \quad (4.9)$$

where $\mathbb{Z}$ is the integer number space; n is the number of levels of decomposition; $\varphi_{\mathrm{j},\mathrm{k_x},\mathrm{k_y}}(\mathrm{x},\mathrm{y})$ and $\psi^{\mathrm{i}}_{\mathrm{j},\mathrm{k_x},\mathrm{k_y}}(\mathrm{x},\mathrm{y})$ are the 2D scaling and wavelet basis functions respectively; $\mathrm{cA}^{\mathrm{j}}_{\mathrm{k_x},\mathrm{k_y}}$ are the approximation coefficients and $\mathrm{cD}^{\mathrm{j,i}}_{\mathrm{k_x},\mathrm{k_y}}$ are the detail coefficients (Horizontal, Vertical and Diagonal, $\mathrm{i} = \mathrm{H},\mathrm{V},\mathrm{D}$) of the gravity difference at level j; $\mathrm{k_x}$ and $\mathrm{k_y}$ are the indices for the shift of the scaling and wavelet basis functions. More details on the formulation can be found on Mallat (1999). Each level of decomposition (n levels) correspond to a different spatial resolution and is reconstructed as follows:

$$\mathrm{Level}_{i=1:n-1} = \mathrm{cD}^{i,\mathrm{H}}_{\mathrm{k_x},\mathrm{k_y}} \psi^{\mathrm{H}}_{i,\mathrm{k_x},\mathrm{k_y}}(\mathrm{x},\mathrm{y}) + \mathrm{cD}^{i,\mathrm{V}}_{\mathrm{k_x},\mathrm{k_y}} \psi^{\mathrm{V}}_{i,\mathrm{k_x},\mathrm{k_y}}(\mathrm{x},\mathrm{y}) + \mathrm{cD}^{i,\mathrm{D}}_{\mathrm{k_x},\mathrm{k_y}} \psi^{\mathrm{D}}_{i,\mathrm{k_x},\mathrm{k_y}}(\mathrm{x},\mathrm{y}), \tag{4.10}$$

$$\mathrm{Level}_{i=n} = \mathrm{cA}^{n}_{\mathrm{k_x},\mathrm{k_y}} \varphi_{n,\mathrm{k_x},\mathrm{k_y}}(\mathrm{x},\mathrm{y}) + \mathrm{cD}^{n,\mathrm{H}}_{\mathrm{k_x},\mathrm{k_y}} \psi^{\mathrm{H}}_{n,\mathrm{k_x},\mathrm{k_y}}(\mathrm{x},\mathrm{y}) + \mathrm{cD}^{n,\mathrm{V}}_{\mathrm{k_x},\mathrm{k_y}} \psi^{\mathrm{V}}_{n,\mathrm{k_x},\mathrm{k_y}}(\mathrm{x},\mathrm{y}) + \mathrm{cD}^{n,\mathrm{D}}_{\mathrm{k_x},\mathrm{k_y}} \psi^{\mathrm{D}}_{n,\mathrm{k_x},\mathrm{k_y}}(\mathrm{x},\mathrm{y}). \tag{4.11}$$

In Figure 4.12, the V_{rr} tensor derived from GGM05S at 450 km is analyzed in various levels of decomposition, each of corresponding to a different waveband for the region of Indonesia. Level 1 corresponds to the very high frequency wavebands (1024-2048 SH), Level 2 to (512-1024 SH) and so on till Level 11 that corresponds to the very long wavelengths (0-2 SH). Analysis shows that GGM05S covers all the wavebands up to 64 d/o spherical harmonic expansion. GRACE-GM derived V_{rr} tensor has been subject to a harsh low pass filter with a cut-off frequency of 600 km in order to match the resolution captured from the long wavelengths of GGM05S. Therefore, it is expected that GRACE-GM wavelet analysis should provide information at the same wavebands as GGM05S. In fact, in Figure 4.13 we notice that the filtered GRACE-GM tensor provides information up to 64 d/o, as GGM05S-derived tensor. The magnitude of the GRACE-GM V_{rr} is approximately 100 smaller than GGM05S, which is expected due to the very long wavelength filter applied. Note also, that for GGM05S the C_{20} spherical harmonic has been replaced by satellite laser ranging measurements (see the Description of GRACE Gravity Model GGM05S, 2013) and therefore the level of decomposition that corresponds to the d/o 2 spherical harmonic cannot not compared with GRACE-GM.

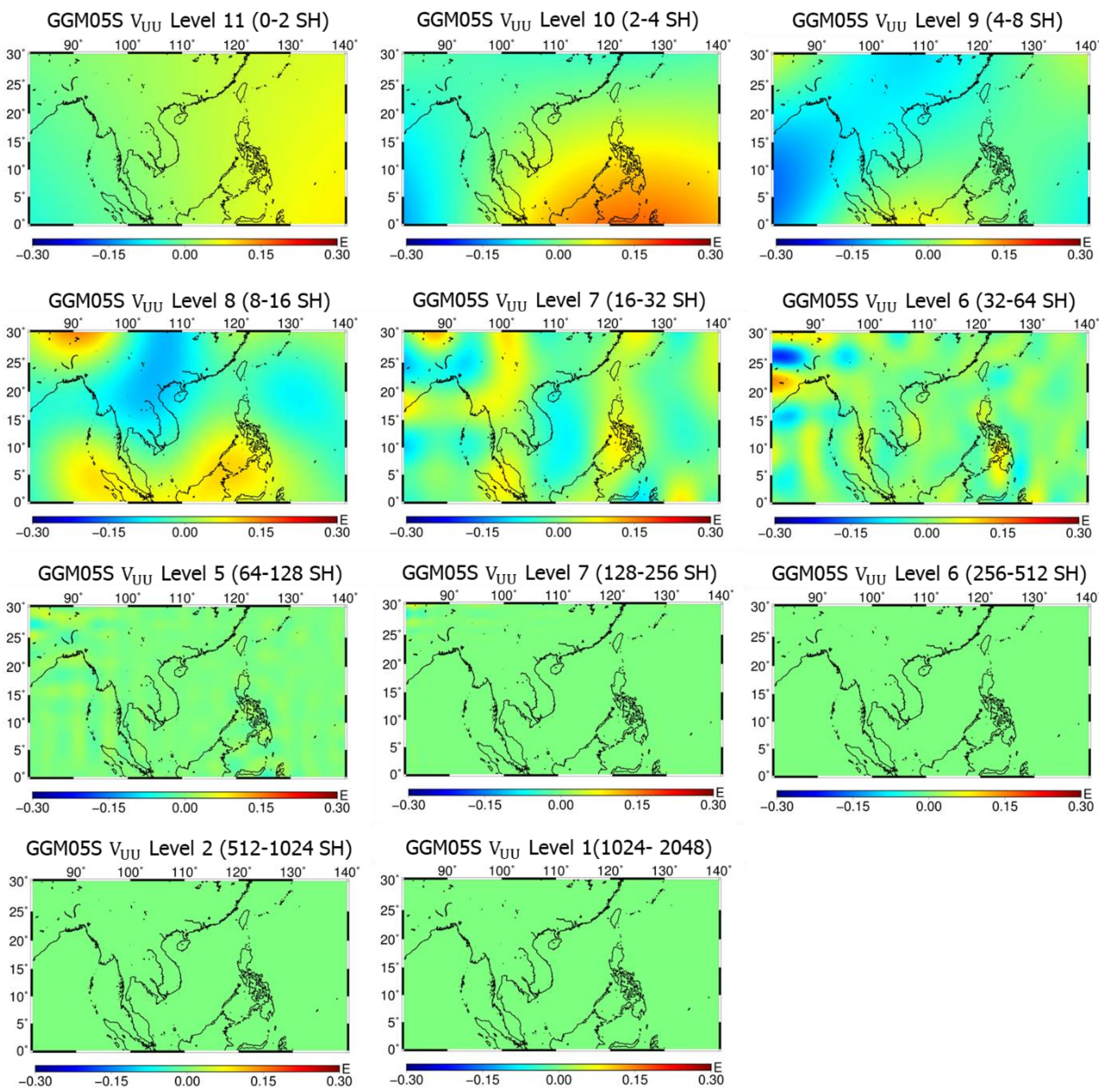

Figure 4.12: Multiresolution analysis of GGM05S V_{UU} estimated at 450 km altitude over Indonesia area.

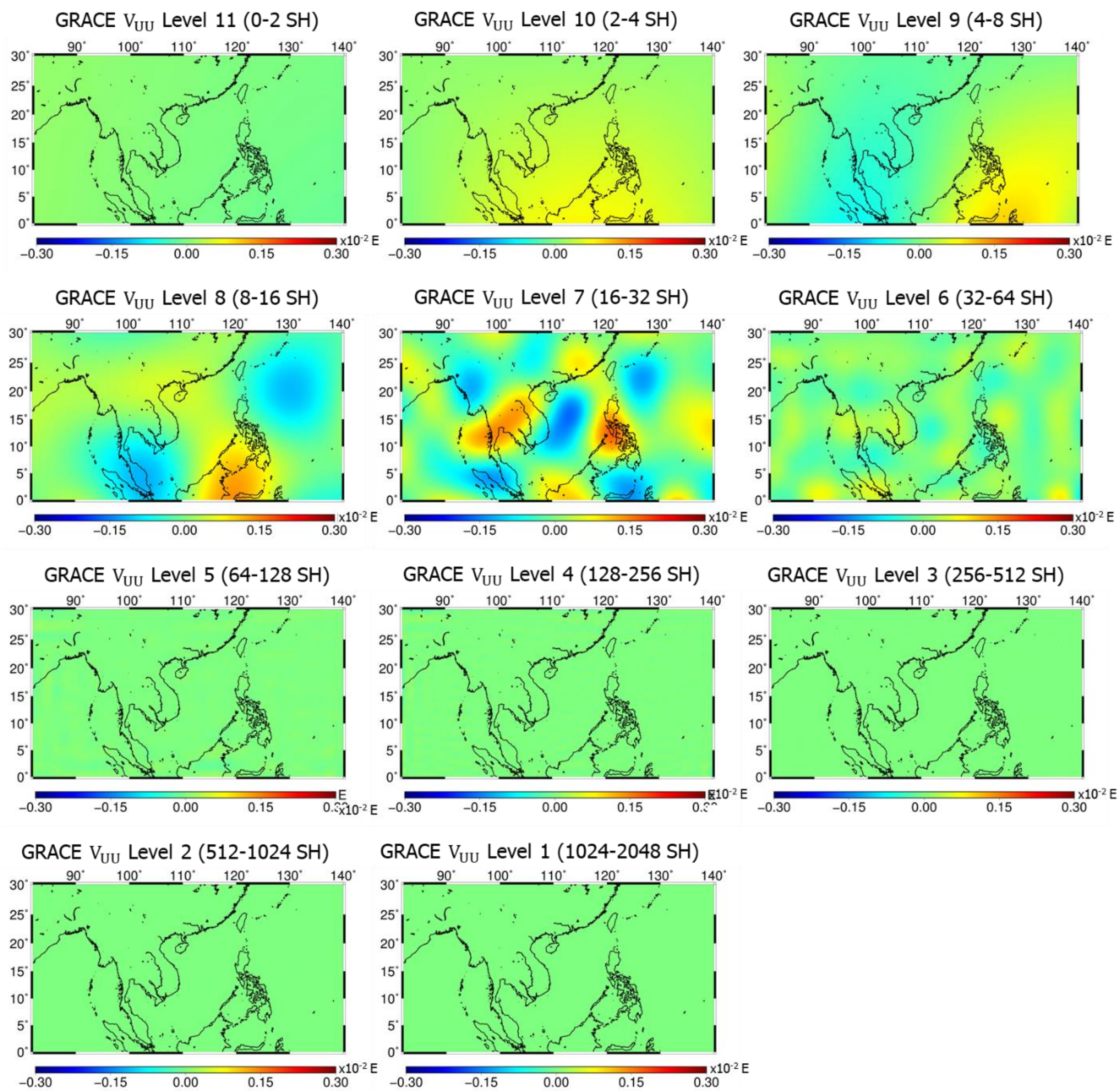

Figure 4.13: GRACE-GM V_{UU} multiresolution analysis into spherical harmonics over Indonesia area. GRACE-GM gradients have been interpolated every 0.1° using kriging interpolation and have been subject to a Gaussian filtering with 600 km cut-off.

4.3.2 GRACE and GOCE GGT comparisons – Quantitative Assessment

We now proceed with a rigorous quantitative assessment of the agreement between GRACE and GOCE gradients. Initially, we estimate the amplitude spectral density of all the GGT components derived from GOCE and GRACE-GM. Figure 4.14 displays the amplitude spectral density of the two missions versus spherical harmonic degree/order. GOCE and GRACE-GM

GGT components demonstrate very similar behaviour and carry most information in the lower degree spherical harmonics. The ratio between GOCE and GRACE-GM GGT amplitude spectral densities reveals that GRACE gradients diminish in the interval [1, 2.5] with respect to GOCE due to altitude difference. It is well known that the attenuation of gradients is small compared to the other gravitational field functionals such as potential and gravity (*cf.*, Equation (4.6); and ESA, 1999). Therefore, GRACE-GM is not just another method of processing the observations. Rather, it is a method that extracts new information from the measurements that is less attenuated with altitude with respect to other functionals of the gravity field.

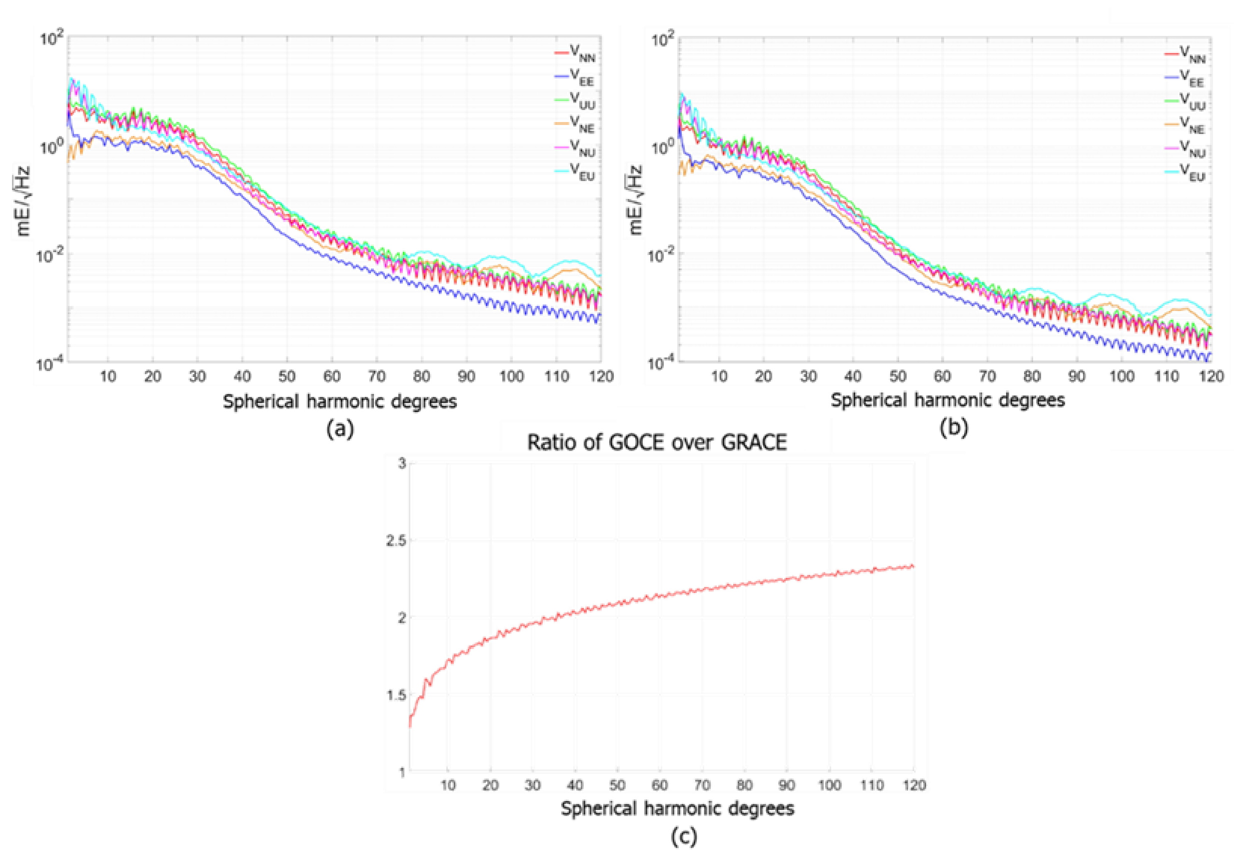

Figure 4.14: Gravitational gradient amplitude spectra: (a) GOCE, (b) GRACE, and (c) ratio of GOCE/GRACE. Note that all the components have the same ratio. The spectra were estimated using the filtered (400-km cut-off wavelength) GOCE and GRACE global gradients.

GRACE-GM gradients are derived from differential accelerations over the distance between the two spacecraft. The distance is not stationary (see Section 4.2), unlike GOCE, where the distance of the accelerometers was fixed to 0.5 m. We argue that the variation of distances can lead to gradients that cover a wider frequency spectrum. Thereinafter, the multispectral nature of gradients is assessed by employing wavelet multiresolution analysis. In contrast to other techniques, multiresolution analysis eliminates spectral leakages, aliasing, and Gibbs phenomenon (Mallat, 1999).

Note that to apply wavelet analysis on the gradients the data should be gridded. We applied a kriging interpolation for both GOCE and GRACE with the grid step being set to 0.1 degrees. A 2-D discrete wavelet transformation is employed to analyze GOCE and GRACE gradients in different levels of decompositions. Both datasets (i.e., GOCE and GRACE-GM) are interpolated using kriging interpolation and the initial grid size for both missions' gradients is set to 0.1° (~11 km at the Equator). Each level of decomposition (wave band) corresponds to a different grid size based on the dyadic sequence of DWT (Peidou et al., 2018) and therefore there are eleven levels (Level 1 ranges between 11-22 km; Level 2 between 22-44 km etc.). The Daubechies wavelet family (order 10) has been tested and proven to perform DWT efficiently. Figures 4.15 and 4.16 display a) GOCE and b) GRACE-GM V_{NN} component analyzed at various levels of decomposition, respectively. The geophysical signal induced by the Indonesia subduction processes is shown in the SH wave band [32, 128] of GOCE V_{NN} (see Figure 4.15). The rest of the levels of decomposition are nearly zero, indicating that GOCE Level 1B data can depict the geophysical signature of Indonesia region only in a very narrow wave band. On the contrary, GRACE-GM depicts geophysical signals in a wider spectrum of frequencies. Figure 4.16 demonstrates that GRACE-GM delineates geophysical signatures in a slightly wider band, namely [8, 128].

Overall, GRACE-GM multiresolution analysis proves that the variable distances, considerably longer than the GOCE accelerometer baseline, result in multispectral gradients that cover low and medium spherical harmonics, while the fixed accelerometer baseline in GOCE can cover only a limited wave band. Hence, we further validate that GRACE-GM can be used complementary to GOCE for gravitational gradient estimation.

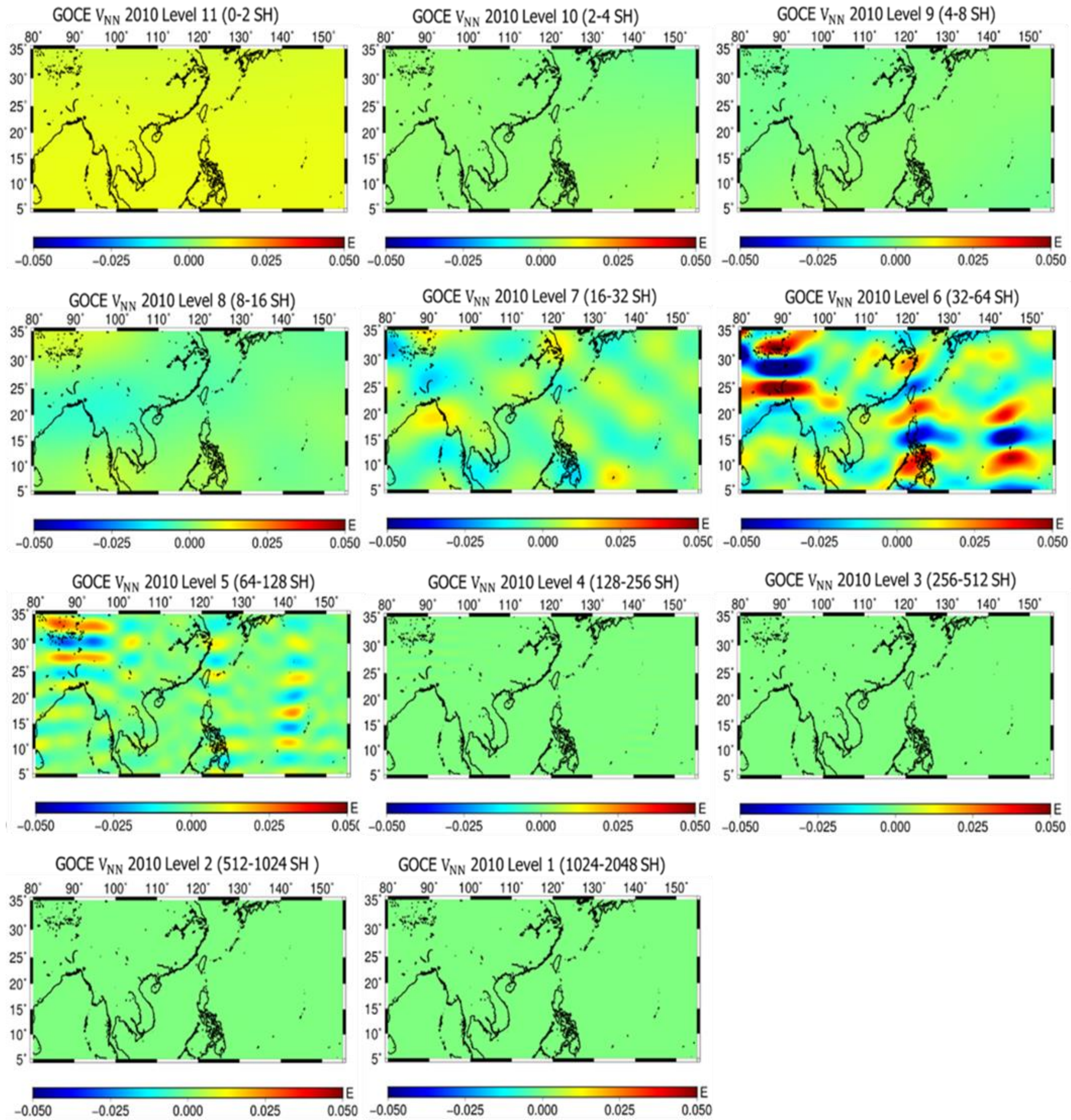

Figure 4.15: a) GOCE V_{NN} multiresolution analysis into spherical harmonics degree expansion over Indonesia area.

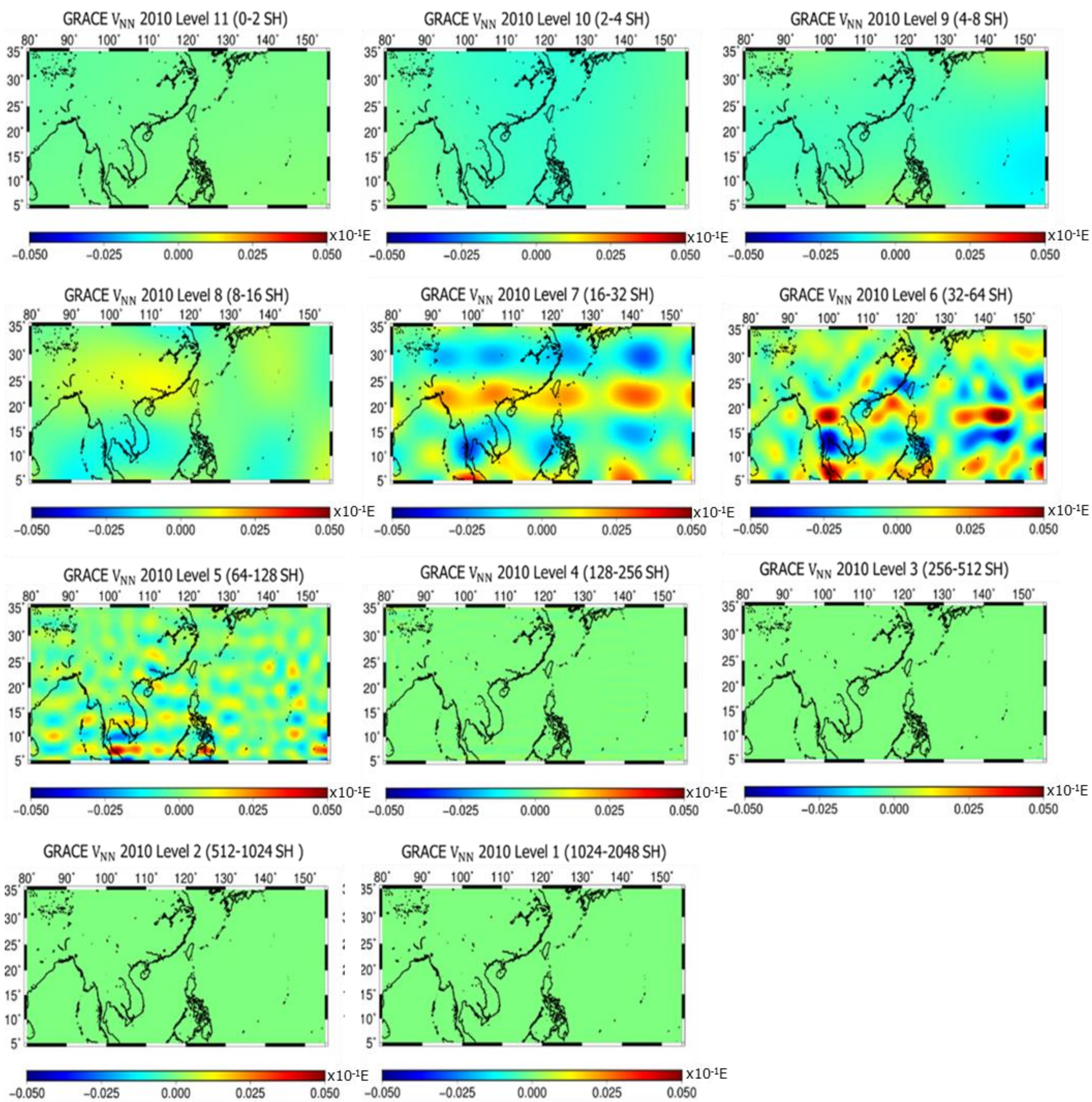

Figure 4.16: GRACE-GM V_{NN} multiresolution analysis into spherical harmonics over Indonesia area.

In a further quantitative analysis of GRACE-GM performance, the coherency between GRACE-GM and GOCE GGTs is examined. Analytical comparisons between GOCE and GRACE gradients for the Himalayan and Indonesia regions reveal high coherence between them, especially in the shorter wavelengths (<100 km). In particular for the Indonesia area, V_{NN} reaches

90% coherence; V_{EE}~ 53%; V_{UU}~82%; V_{NE}~60%; V_{NU}~62% and V_{EU}~80% (see Figure 4.17). Other areas with distinct geophysical signals, such as the Gulf of Alaska and the Japan trench, have been studied, and results also show a strong agreement between GOCE and GRACE GGTs.

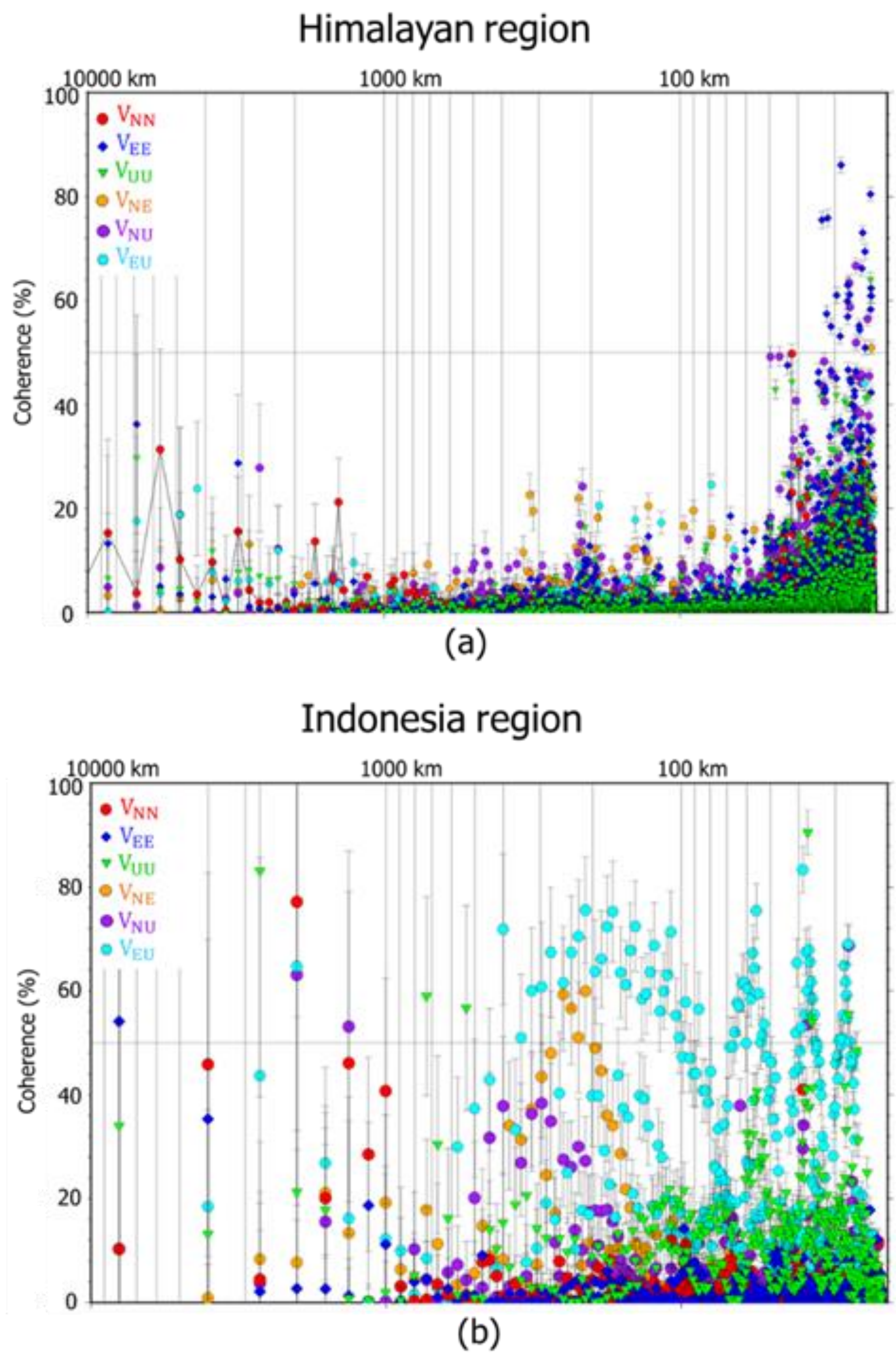

Figure 4.17: GOCE and GRACE-GM Gravitational Gradient Tensors coherence over a) Himalayan and b) Indonesia areas.

The last important step of our quantitative analysis regards the estimation of the error floor of GRACE-GM gradients. One approach would be to apply propagation of the Level 1B errors to the gradients as estimated by Equations (4.3) and (4.4) for V_{xx} and V_{xy}, respectively. However, lack of information on their correlation will lead to significant underestimation of errors. Therefore, we use frequency domain analysis of the GGT trace to estimate the type and the level of errors. The GGT trace should nominally be equal to zero (i.e., $V_{xx} + V_{yy} + V_{zz} = 0$). However, gradiometric measurements usually deviate from the nominal values due to various types of errors, and therefore, the trace can serve as an indicator of the quality of the GGT. In Figure 4.18 we show the power spectral density of the GRACE-GM trace during April 2010 (estimates around the globe). Note that both ascending and descending tracks were employed. As the GGT trace is practically the residual of the Laplacian of the Earth's gravitational potential, we calculate the noise level by integrating the power spectral density of the trace over the instrument bandwidth (shaded area). This process reveals an error of ±48 mE (the square root of the power within the instrument bandwidth) and indicates pink noise ($1/f$). Assuming no correlation between the trace components, the error of the GGT diagonal components is approximately ±28 mE. Of note is that GRACE-GM trace peaks in the lower frequencies. Ince (2016) notes the same behaviour on GOCE trace estimates and suggests narrow bandwidth filtering between [180, 300] s. The above refer to the 10 Hz interpolated data. The estimated gradients refer to GRACE-A SRF and using the azimuth of the tracks they are finally referenced to ENU system.

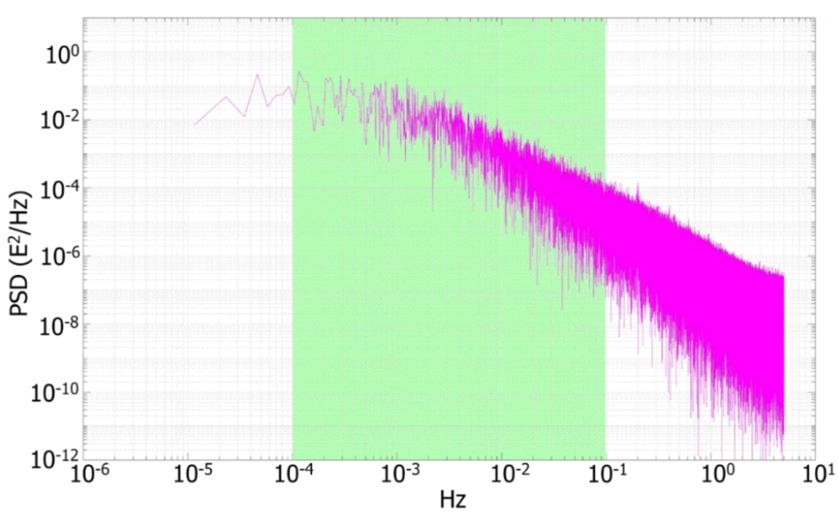

Figure 4.18: Power spectral density of GRACE-GM trace during April 2010 estimated around the globe. Green shaded area denotes the ACC bandwidth $[10^{-4},\ 10^{-1}]$ Hz.

4.4 Discussion

The effectiveness of the GRACE-GM method was initially assessed by employing GOCE DM accelerations, since they are the fundamental quantities for deriving the gravitational gradients. The classification of GRACE orbits into ascending and descending tracks as well as into daytime and nighttime tracks was necessary for such comparisons due to the GOCE dusk-dawn, sun-synchronous orbit. Comparisons of the DM accelerations from the two missions demonstrated a strong similarity in their structure, particularly exposing the very strong magnetic inclination signal. Notwithstanding this similarity, the GRACE DM magnetic inclination signal in all tracks appeared consistent in position with the IGRF11 model, whereas the inclination disturbance on GOCE showed an unexplained significant shift between ascending and descending tracks, none of which agrees with GRACE or IGRF11.

GRACE gravitational gradients were estimated using DM accelerations and the distance between the two spacecraft. The key element that allows the estimation of gravitational gradients from GRACE is the attitude determination that carries all the gravitational signal information that is propagated to the final gradients. GRACE-GM gradients were compared to gradients calculated from GRACE Level 2 products. It was concluded that GRACE-GM can depict shorter-scale mass transfers with the trade-off of high noise level. Of note is that GRACE Level 2 gradients have been subject to postprocessing (e.g., filtering, downward and upward continuations), and therefore, a direct comparison between GRACE-GM and GRACE Level 2 gradients is not very indicative of the efficiency of the new technique. Therefore, it was necessary to compare GRACE-GM with GOCE Level 1B gradients; the data from both missions are Level 1B and have not been subjected to extensive postprocessing as Level 2, while the attenuation of GRACE-GM gradients is minimal compared to GOCE.

GRACE gradients were juxtaposed to GOCE gradients and a strong and promising agreement between the two was demonstrated both in magnitude and signature. Considering the post-GOCE era gap in the gravitational gradients with global coverage and the discussions for follow-on missions (Rummel, 2003) with new innovative satellite configurations (Hauk and Pail, 2019), a "virtual GOCE-FO" mission may be achieved by employing the GRACE-GM methodology on the GRACE-FO mission.

Comparisons between the two missions also revealed an unexpected and important discovery. The ascending nighttime GRACE DM accelerations showed a visible characteristic disturbance in the auroral oval. We believe that this disturbance resembles the Birkeland current cyclical pattern confined by the 60th parallel in the north. In addition, visible disturbances present in the GRACE DM accelerations in the uncompensated x axis and in all tracks within the north auroral oval resemble the GOCE magnetic disturbances present in the DM accelerations and GGT. We note here that the likely effects of the Birkeland currents on GRACE cropped up unexpectedly from the classification of the orbits done for the purpose of deriving gravitational gradients. The above need further investigations with possible impact on GRACE data inversion.

Finally, the concept of GRACE-GM can be very useful in compensating any malfunctions of GRACE-FO instrumentation. The instrumentation of any of the two spacecraft can either poorly perform or be totally switched off as occurred in September 2016, when GRACE-B accelerometer ran out of power. To recover the gravitational field, a technique called “transplant” employed GRACE-A ACC data and corrected them for time, attitude, and residual linear accelerations (spikes; Bandikova et al., 2017, 2019). GRACE-GM can advance the efficiency of this technique by “bringing” the two spacecraft as close as possible, where the non-gravitational forces acting on each spacecraft are nearly the same (see Section 4.2), and therefore, the “transplanted” measurements could resemble more realistically the non-gravitational accelerations acting on GRACE-B. Therefore, it is expected that GRACE-GM may have a substantial contribution on improving the gravitational field estimates in cases of instrumentation failures.

GRACE-GM is a novel methodology with contributions in geophysical signal prospecting. Gravitational gradients can be obtained from GRACE and GRACE-FO not equipped with a gradiometer. Overall, GRACE-GM can have a substantial contribution in the studies of the gravitational field and can improve the gravitational field models because the technique provides (a) full GGT without postprocessing, (b) multispectral resolution, and (c) a new processing scheme to supplement any malfunction or poor performance of the GRACE-FO instrumentation. The biggest limitation of the technique is the high noise level and further analyses on the accumulated errors should be employed to fully quantify the error level of its component.

Additionally, magnetic field induced disturbances should be further studied and removed from the final gradients to lead to a global GRACE-GM GGT map. Therefore, further work is required to advance the idea of GRACE-GM to an operational method.

4.5 Summary

This chapter introduced a new proof-of-concept that views the GRACE twin satellites with extension to the recently launched GRACE follow-on gravity space mission (GRACE-FO) as a system that can be transitioned into a 3D gradiometer. This chapter presented and discussed one of the original contributions of this research, that is deriving gravitational gradients using GRACE instrumentation.

5

Discovering the origin of stripes in GRACE models

In Chapter 4, we estimated gravitational gradients using GRACE on-board measurements. While applying the differential mode approach to other GRACE instruments, we found that the POD-derived total accelerations suffer from stripes, even when simply differenced between GRACE-A and GRACE-B, i.e., without time-shifting the measurements (*vis*., Fig 5.16). This finding, along with other evidence from the analysis on various LEO missions signaled the direction of our study that is, analysis of the orbits of GRACE to investigate how they may drive the stripe artifact on GRACE models.

Sections 5.5 and 5.6 are unabridged versions of the original research article *"Stripe mystery in GRACE geopotential models revealed"* published in *Geophysical Research Letters* (Peidou and Pagiatakis, 2020), with additions of more results in Section 5.5.2.

5.1 Introduction

With the aim of this research being to improve the performance of GRACE-based models, this chapter focuses on the well-known artifact of stripes that appear in the solutions of the gravitational field recovered from GRACE measurements. The artifact of stripes has been evident since the release of the first stream of temporal and static GRACE-based models (e.g., GGM01S); and the first studies on the Earth's water storage and ocean mass variations that used GRACE models mention the need for low pass spatial filtering with smoothing radius of 750 km and 1500 km (see, e.g., Chambers et al., 2004). Chen et al. (2005) introduced several spatial smoothing schemes to eliminate a phenomenon called "striping" in GRACE global terrestrial water storage maps, whereas Bosch (2005) adapted the term "meridional stripes" to describe the presence of stripes in EIGEN-GRACE02S gravity model while validating marine gravity data. In 2005 a non-isotropic empirical filter with large smoothing radii along the two directions, was also designed to filter the "*ill-determined higher-degree components of GRACE monthly models"* (Han et al., 2005).

It was four years after the release of the first GRACE gravity model that this systematic error was independently addressed. Swenson and Wahr (2006) studied the presence of systematic linear features that extended in N-S direction and dominated the shorter wavelengths of the gravitational field. This effect, widely known as "longitudinal stripes" (e.g., Save et al., 2016; Davis et al., 2008) was attributed to the spatial correlation of the high d/o spherical harmonics (ibid, 2006). Swenson and Wahr (2006) introduced a "decorrelation spatial filter" and tested several smoothing radii (i.e., 250 km; 500 km; 750 km and 1000 km halfwidth) to reduce the magnitude of the stripes. The filter removes a polynomial function fitted to a moving window of spherical harmonic coefficients of the same parity degree. The simplicity of the Swenson and Wahr (2006) filter and the achieved improvement of the GRACE model performance made it one of the most widely applied filters in GRACE literature. Later, a number of filters were introduced and applied either in space or frequency domains. The most widely used filters are the anisotropic decorrelation filters applied in the frequency domain as a regularization scheme (Kusche, 2007; Kusche et al., 2009). The smoothing of the DDK series of filters depends on the kernels of the filter, that is the localization properties in space act either as a weak smoothing (narrow kernel) or a harsh smoothing (broad kernel). There are eight different kernels available that range from DDK1 (harsher smoothing) to DDK8 (weakest smoothing). Klees et al. (2008) also suggested an anisotropic and adaptive filter to remove noise from spherical harmonic coefficients by means of an anisotropic non-symmetric filter. Other studies recommended the use of a statistical test on spherical harmonics (Davis et al., 2008) or the use of stochastic filters to decipher the signal from the correlated errors (Wang et al., 2016). Wouters and Schrama (2007) employed empirical orthogonal functions to decompose the spherical harmonic coefficients and after testing each mode for noise, they reconstructed the signal. Later, several other filtering schemes were introduced with some of them focusing on advancing or tuning older filters. A modification of the "destriping filter" of Swenson and Wahr (2006) was done by Duan et al. (2009), while RL05 solutions have been filtered using an optimized decorrelation filter discussed in Belda et al. (2015).

Each filter has its strengths and weaknesses, however all of them result in geophysical information loss, especially in areas where the filter has a very narrow passband. Although many filters have been suggested to remove the stripes at various levels of success, their origin has remained a rather controversial subject over the GRACE lifetime and beyond. Many contradictory hypotheses have been suggested, but to the best of our knowledge, they have simply remained conjectures. Some studies suggested that the stripes are induced by spatial correlations in the GRACE errors and are evident in order eight and higher spherical harmonics (Swenson and Wahr, 2006), while other studies suggested that the stripes are spatial aliasing errors induced by atmospheric and oceanic tidal and non-tidal aliases, evident in order 15 or multiples of 15 spherical harmonics (Seo et al., 2008a). However, ocean tides have been dismissed as the cause of stripes (Seo et al., 2008b). The limited longitudinal sampling due to GRACE orbit configuration (Klees et al., 2008) has also been suggested as a factor that can lead to stripes. Watkins et al. (2015) suggest the orbitals errors due to poor observability of the east-west gradients as the leading cause of stripes, while very recent studies suggested that stripes are temporal aliasing effects induced by the inter-satellite range rate between the two GRACE spacecraft (Hauk and Pail, 2019). It is evident from the above that the hypotheses for the origin of stripes cover a wide spectrum of possibilities that range from spatial correlation to poor sectorial observability and from near-sectorial limited observability to temporal aliasing due to the inter-satellite ranging. Rightfully, one may wonder what the physical cause of stripes is, due to contradictory claims, and due to the absence of any proof in the peer reviewed literature. To the best of our knowledge, all these potential causes have never been fully addressed or proven; rather, they remain widespread conjectures.

The nearly identical GRACE-FO mission is also contaminated by stripes and the existing filters are applied, either a priori in form of covariance matrices (Kusche et al., 2009) or in the post-processing stage directly on the monthly solutions. Of note is that new methods, such as spherical cap mascons also demonstrate stripes (Ivins et al., 2011; Watkins et al., 2015), whose magnitude is minimized by using a priori covariance matrices in the final solution (Watkins et al., 2015; Equation (15)).

Stripes on GRACE and GRACE-FO have been a notable constraint to geoscience applications as they limit the spatial resolution of the available models, and therefore detection and monitoring of geophysical processes with spatial scale less than 200 km becomes challenging. Discovering the origin of stripes requires a thorough investigation and physical understanding of the mechanism that induces them. In this research, we show that the stripes are not the result of aliasing, i.e., they are not generated from under-sampling high frequency gravitational signal(s). On the contrary, we show that the stripes are the result of oversampling a low frequency gravitational signal in the latitudinal direction, namely the low-degree latitudinal (sectorial) disturbing potential (geoid), with a sampling frequency near $\frac{m}{n} f_s$, where f_s is the spatial frequency of the GRACE ground tracks along the parallels, and *m* and *n* are integers with $n>2m$. We achieve this by working in both spatio-temporal and frequency domains using Fourier theory, and least-squares spectral and wavelet analyses methods.

5.2 Stripes on other LEO missions: CHAMP and Swarm

Although the GRACE stripes have been known as disturbing features in the GRACE models since the beginning, it was not the first time that a space gravity mission experienced this artifact. In fact, stripes were evident in the models of the first space gravity mission CHAMP (Reigber et al., 2002), a fact that was overlooked in GRACE literature on stripes. Flechtner et al. (2010) mentioned the presence of meridional stripes in the CHAMP-based model, EIGEN-CHAMP03S (Reigber et al., 2004). Figure 5.1a displays the gravity anomalies from EIGEN-CHAMP03S; the impact of the north-south stripes is evident around the globe. Interestingly, we discovered that it is not only space gravity models that suffers from stripes, but other LEO missions, such as Swarm (2013-present), demonstrate the same artifact (see Figure 5.1b). Swarm targets the measurement of the Earth's static and dynamic magnetic fields and it is a constellation of three spacecraft: two satellites are in a i=87.4^{o} inclination orbit at 450 km altitude and the third is at i=88^{o} inclination at nearly 530 km altitude. Swarm payload consists of magnetometers, accelerometers and electric field instruments.

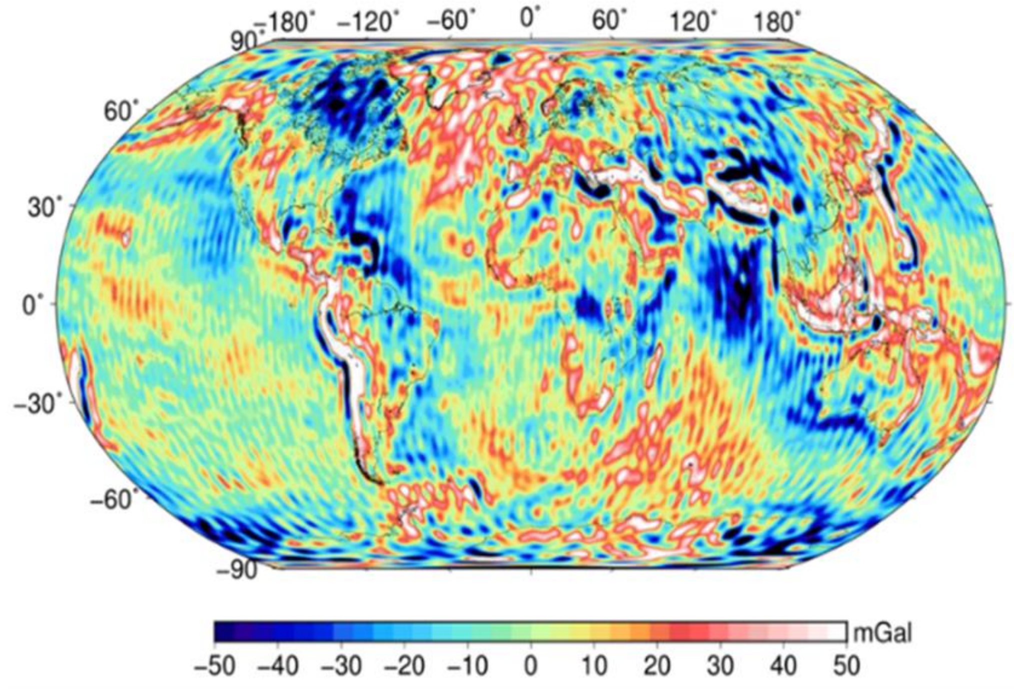

(a)

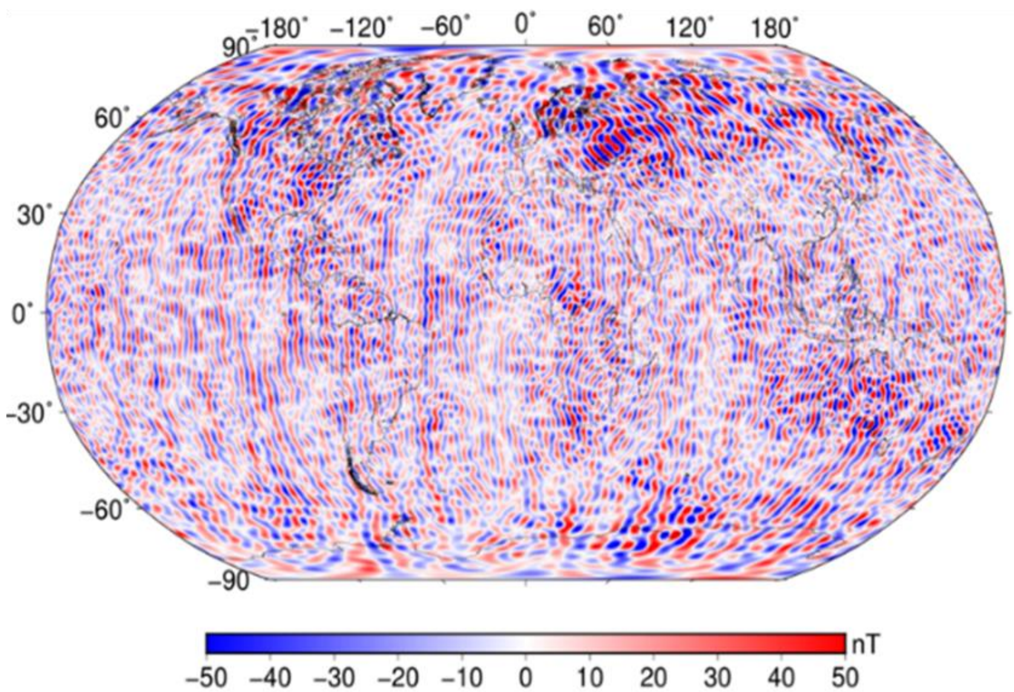

(b)

Figure 5.1: a) CHAMP: Gravity anomalies estimated using EIGEN-CHAMP03S; b) Swarm: Field differences in Y component between magnetic lithospheric models MLIi2C and MLIi2D.

As the presence of stripes on CHAMP and Swarm models was not adequately addressed, the origin of this artifact remained unknown. Of note is that the only space gravity mission that did not suffer from stripes was GOCE, a single spacecraft mission that measured the second derivatives of the gravitational potential in a near polar sun-synchronous (dusk-dawn) orbit. Table 5.1 summarizes the characteristics of the four LEO missions and highlights the presence of stripes in their models, if applicable.

Table 5.1: Characteristics of space gravity and space magnetic missions

	Number of Spacecraft	**Goal**	**Key-science instrumentation**	**Inclination (º)**	**Orbit**	**Stripes**
CHAMP	1	Map the Earth's gravitational and magnetic field	GPS and SLR, SuperStar 3-axis accelerometer	87	Non-sun-synchronous	Yes
GRACE	2	Map the temporal variations of the Earth's gravitational field	GPS and SLR, SuperStar 3-axis accelerometer, K-band inter-satellite ranging system	89	Non-sun-synchronous	Yes
GOCE	1	Map the static part of the Earth's gravitational field	GPS/ GLONASS and SLR, Gradiometer (Six 3-axis accelerometers)	96.7	Sun-synchronous	No
Swarm	3	Map the temporal variations of the Earth's magnetic field	Magnetometers	87.4 / 88	Non-sun-synchronous	Yes

It is noticeable that the four missions listed in Table 5.1 had different configurations, carried different instrumentation and followed different principles to recover the potential field they targeted to measure. However, three missions that resulted in “stripy” models followed a non-sun-synchronous orbit. Figure 5.2 displays the ground tracks over one month for GRACE (January 2010), GOCE (January 2010) and Swarm (January 2014) missions. The geometry of the ground tracks is very different among the missions and in Section 5.4 we discuss how this geometry is related to stripes.

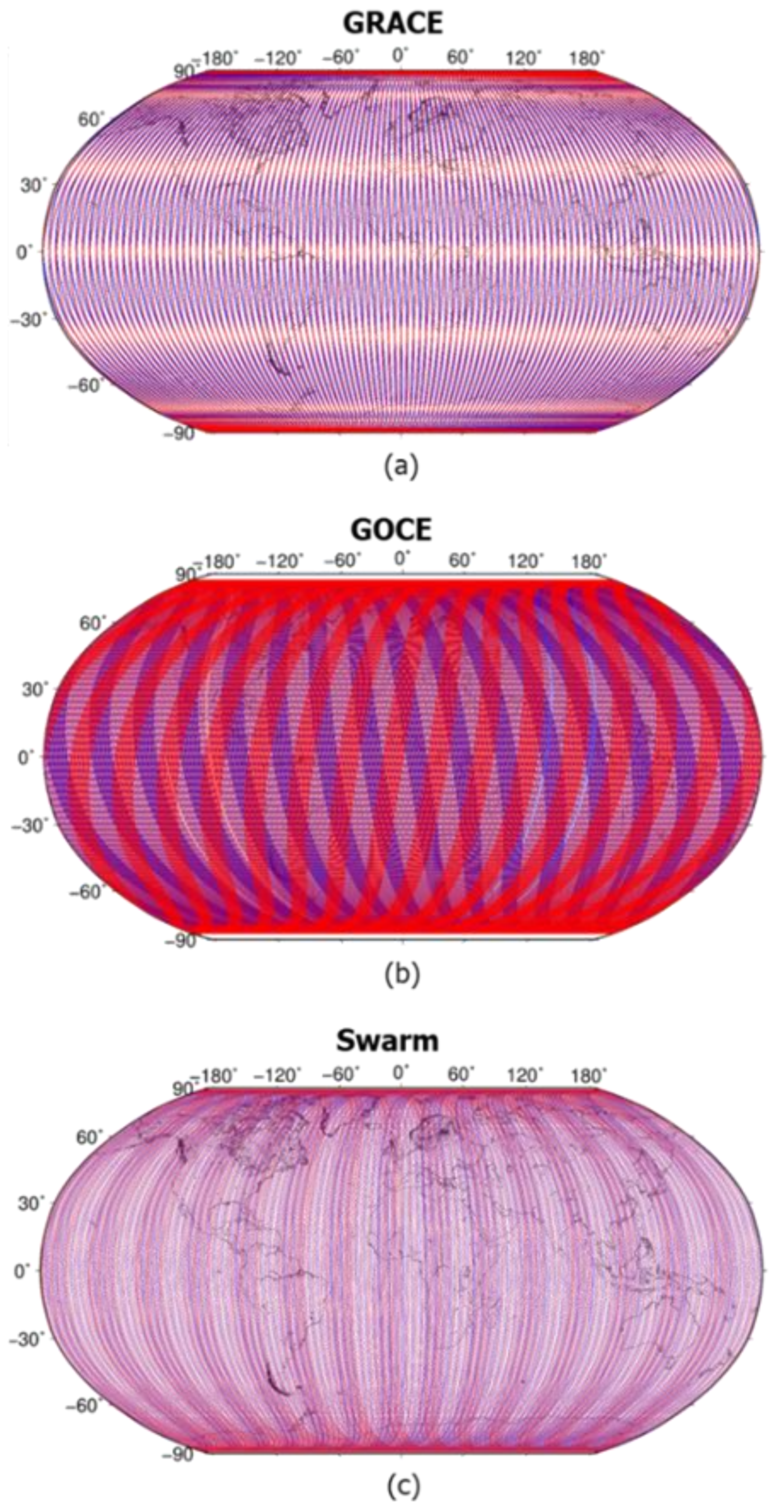

Figure 5.2: a) Ground tracks of GRACE-A during January 2010; b) Ground tracks of GOCE during January 2010; c) Ground tracks of Swarm-A during January 2014. Ascending tracks are denoted with blue color and descending with red.

5.3 Spectral and geospatial characteristics of GRACE stripes

To fully understand the mechanism that induces stripes, it is necessary to understand how stripes behave in space, time and frequency domains. We analyze 36 monthly gravity anomalies solutions derived from the currently available RL05 of d/o 96 for the period 2008-2010. We are fully aware that RL05 contains a smaller number of much fainter (i.e., lower magnitude) stripes, but we are only interested in examining consistency of their spectral characteristics in time and around the globe. To enhance the effect of stripes, the solutions filtered using the DDK3 decorrelation filter are subtracted from the total field (Kusche et al., 2009).

We adopt the terms *longitudinal* to mean direction along the meridians and *latitudinal* to signify directions along the parallels of latitude. When we refer to *stripes* we refer to the full wavelength stripes, that is the distance between two consecutive crests (or equivalently troughs). Figure 5.3 displays the enhanced stripes on the gravity field for various months in 2010.

Full latitudinal stripe profiles at arbitrarily selected $\phi = 30^0$N are presented in Figure 5.4 (left panels; in blue). A simple superposition of these monthly profiles in the spatial domain reveals the striking occurrence of a nearly constructive wave pattern (cf., Figure 5.4g), signaling an interesting behaviour of stripes in the space domain. The visual observation of the patterns of the stripes in the latitudinal profiles as depicted in the left panels of Figure 5.4 marked the starting point of the investigation, after all, the appearance of the stripes themselves reminds us of the constructive and distractive fringes as explained in moiré theory. Generally, from a geometric approach, a moiré pattern describes the interference of overlaid grids that are misaligned (translated) or rotated, resulting in constructive and destructive fringes that follow an interchange pattern (Theocaris, 1969; Glass, 1969). We suspect that GRACE overlaid daily ground tracks result in constructive and destructive fringes showing as crests and troughs in GRACE-based gravity field models.

We investigate whether the spatial behaviour of stripes from month to month matches the respective GRACE ground track pattern. Therefore, we formulate the hypothesis that the stripes are interference fringes created from the travelling wave-like ground track characteristic behaviour in space-time. Whereas, in principle, the phenomenon of wave interference is relatively simple and well known from physics, creating wave patterns from ground tracks that will eventually produce the GRACE stripes may practically be very challenging.

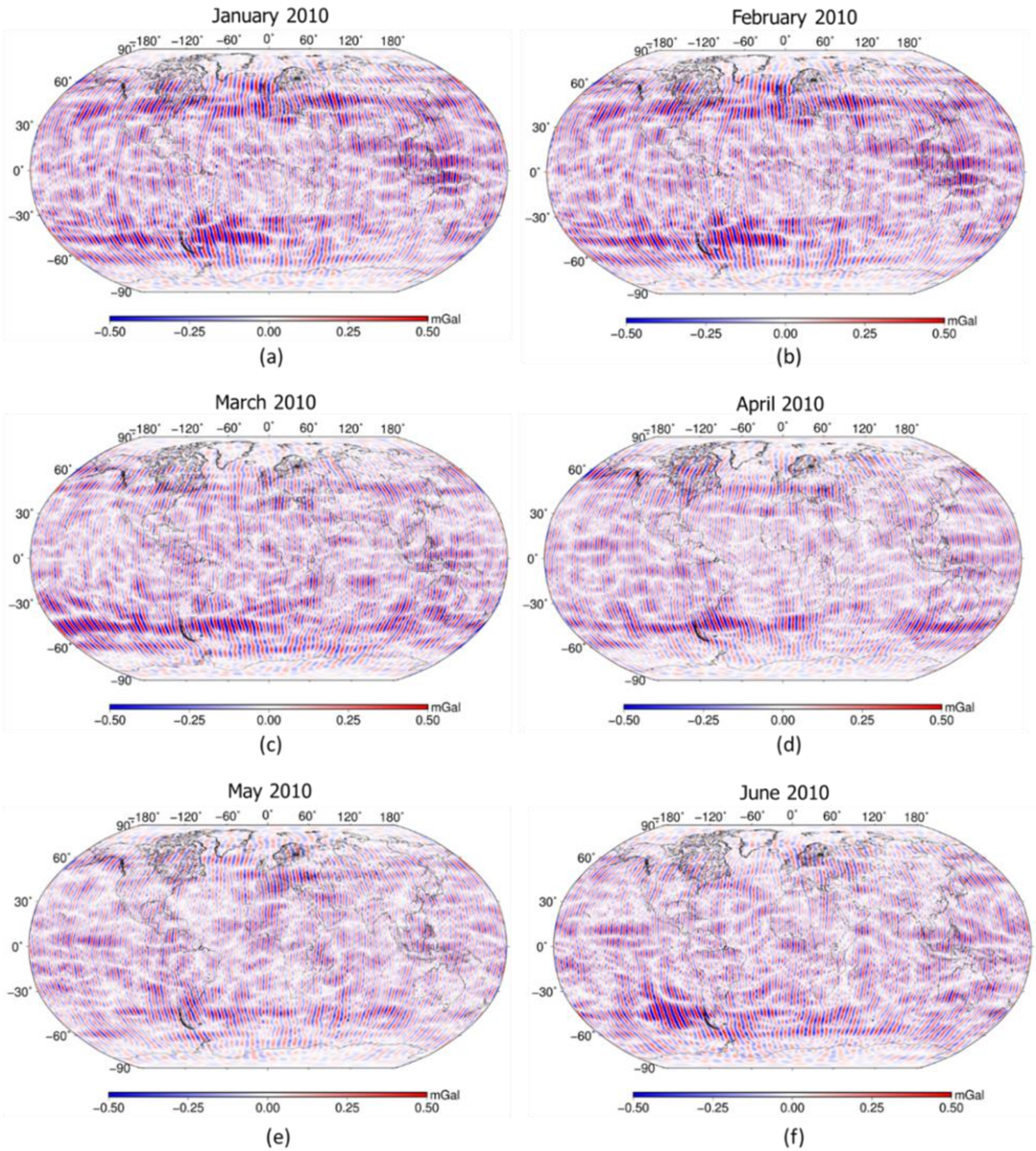

Figure 5.3: Stripes on RL05 monthly gravity anomalies (January to June, 2010).

Afterwards, we strive to test our hypothesis through a series of ground track data processing methodologies and analyses, using simple physics principles and data analytics, such as Least Squares Spectral Analysis (LSSA) (Vanicek,1963; Pagiatakis, 1999), Least Squares Wavelet Analysis (LSWA) (Ghaderpour and Pagiatakis, 2017) and Least Squares Cross Wavelet Analysis (LSCWA) (Ghaderpour et al., 2018). These spectral analyses methods have been proven excellent methods in analyzing non-stationary and unequally spaced data series without the need for editing at a pre-analysis stage (Ghaderpour and Pagiatakis, 2017).

LSSA estimates the spectrum of a data series by employing least-squares fit of sinusoids to the longitudinal profiles. Note that in Figure 5.4, we only show a sample of six-monthly stripe profiles that were used for fact-finding. In our analyses and results, 36 monthly longitudinal profiles were used. The spectra of the stripe profiles are displayed in the right panels of Figure 5.4. The abscissa values indicate frequency in cycles per the entire length of the profile, i.e., in 360° longitude, hereafter indicated by c/ℓ, and the ordinate values signify percentage variances, i.e., how much each of the frequency peaks separately contributes to the series.

In the spectra three distinct dominant peaks with frequencies 63.5, 76.7 and 79.4 c/ℓ are identified. The superposition of the monthly stripe profiles contains exactly the same dominant frequencies (Figure 5.4g; bottom panels) found in the monthly profiles. In fact, we find precisely the same frequencies in the superposition of the 36 profiles (Figure 5.4h). This behavior is expected because the least squares spectrum is a linear transformation applied to a superposition of the monthly series that have identical frequencies (see the addition theorem of Fourier theory (Bracewell, 1978)).We point out that it is in agreement with the fact that the stripes never cancel out regardless of the length of the data used to produce the gravity models (monthly, annual, multi-year). To this end, we confirm that the stripes demonstrate the same spectral characteristics for all monthly profiles and their superposition. Latitudinal profiles along other parallels have similar but not identical beating frequencies.

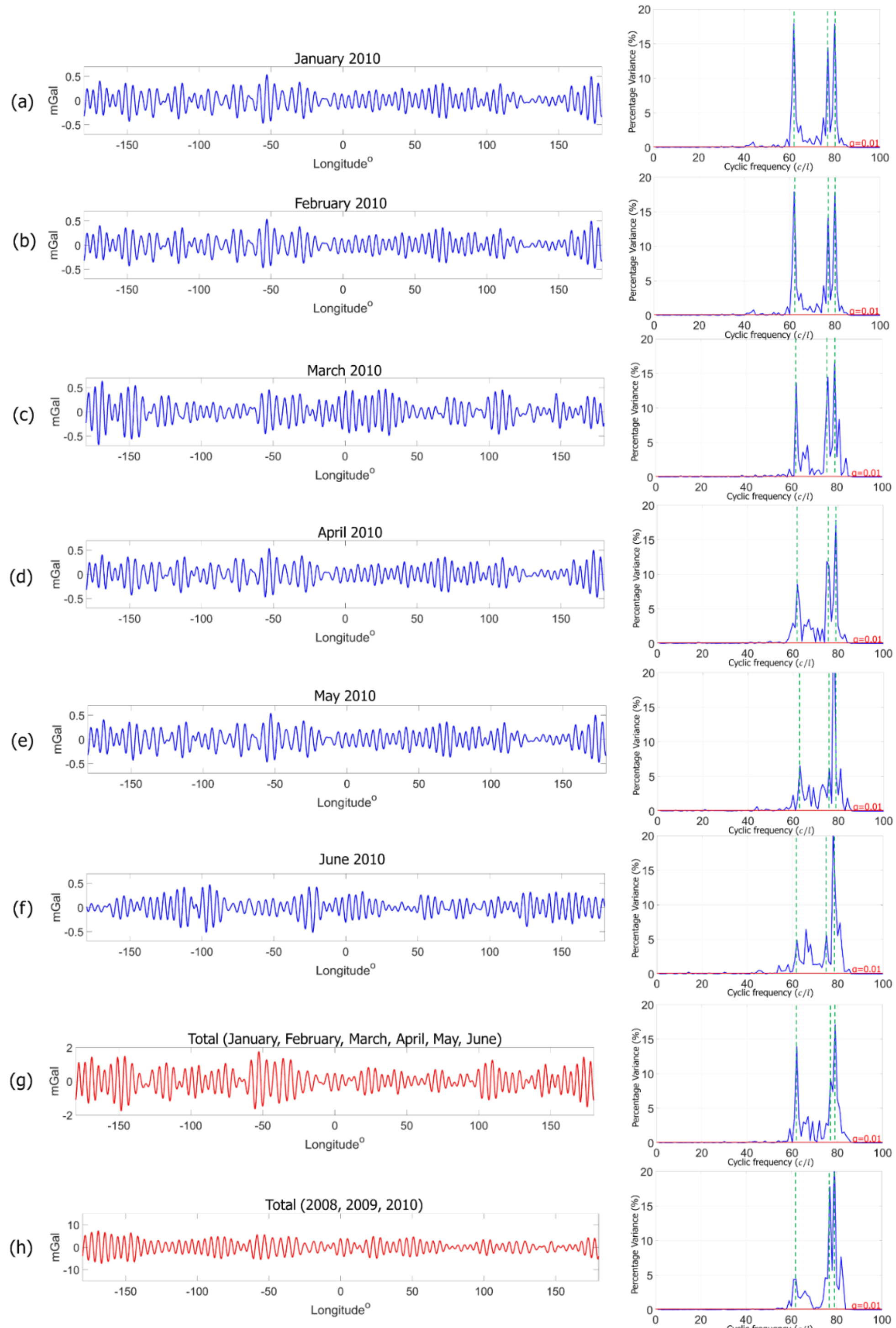

Figure 5.4: a-f) Left panels: Longitudinal profiles of stripes at $\phi = 30^{\circ}$ for January to June 2010; Right panel LSS of longitudinal profiles of stripes at $\phi = 30^{\circ}$ for January to June 2010; g) Series superposition (January to June 2010; Left panel) and its Least-squares spectrum (right panel); h) Series superposition of 36 monthly releases (left panel) and its Least-squares spectrum (right panel). Red line indicates the confidence level (i.e., 99%). Dashed green lines indicate the significant peaks at 63.5, 76.7 and 79.4 c/ℓ.

Of note is that the 1D spectral analysis performed herein shows only the average characteristics of the entire data series and not specific characteristics of local nature. Nevertheless, this first step is important in identifying the general characteristics of the stripe profiles and leads to the next step of spatio-temporal analyses using least-squares wavelet analysis.

To investigate the nature of the stripe periodicities in the space-frequency domain, LSWA is employed, a transformation particularly useful for feature extraction in space/frequency domain (see Ghaderpour and Pagiatakis, 2017). Given that the profiles span the entire Earth $[-180^o \leq \lambda \leq 180^o]$, we use the fundamental wavelength (unit length) of $\ell = 360$ degrees.

The sampling rate of the gravity anomalies is set at 0.1 degrees (in longitude) and hence there are $M = 3600$ samples with Nyquist frequency of 1800 c/ℓ. As in the previous 1D spectral analysis using LSSA, we choose the frequency band $\Omega \in \{1, 100\}$ c/ℓ (cf., ibid, 2017). Figure 5.5 displays the scalograms (space vs. frequency) of the six longitudinal profiles used in the previous step. All scalograms show peaks at 63.5, 76.7 and 79.4 c/ℓ, demonstrating very similar behaviour in all months. The magnitude variations of the stripes (colour scale) suggests that the wavelength of stripes is stationary as opposed to the magnitude that is non-stationary.

Furthermore, we notice a tendency of separation in space of the two main peaks indicating that they are not dominant at the same places, i.e., one exhibits strong magnitude when the other is weak and vice versa (Figure 5.5). This behaviour is explained in Section 5.5.

Further to the previous analyses, we now attempt to determine whether the wave-like nature of the stripes can be represented as a travelling wave in space-time, or equivalently if there is a phase lag from month to month. Least squares cross-wavelet analysis (LSCWA) (Ghaderpour et al., 2018) is employed for this analysis. Amplitude and phase cross-scalograms between various consecutive monthly latitudinal profiles are estimated to determine a possible translation of the stripes from month to month.

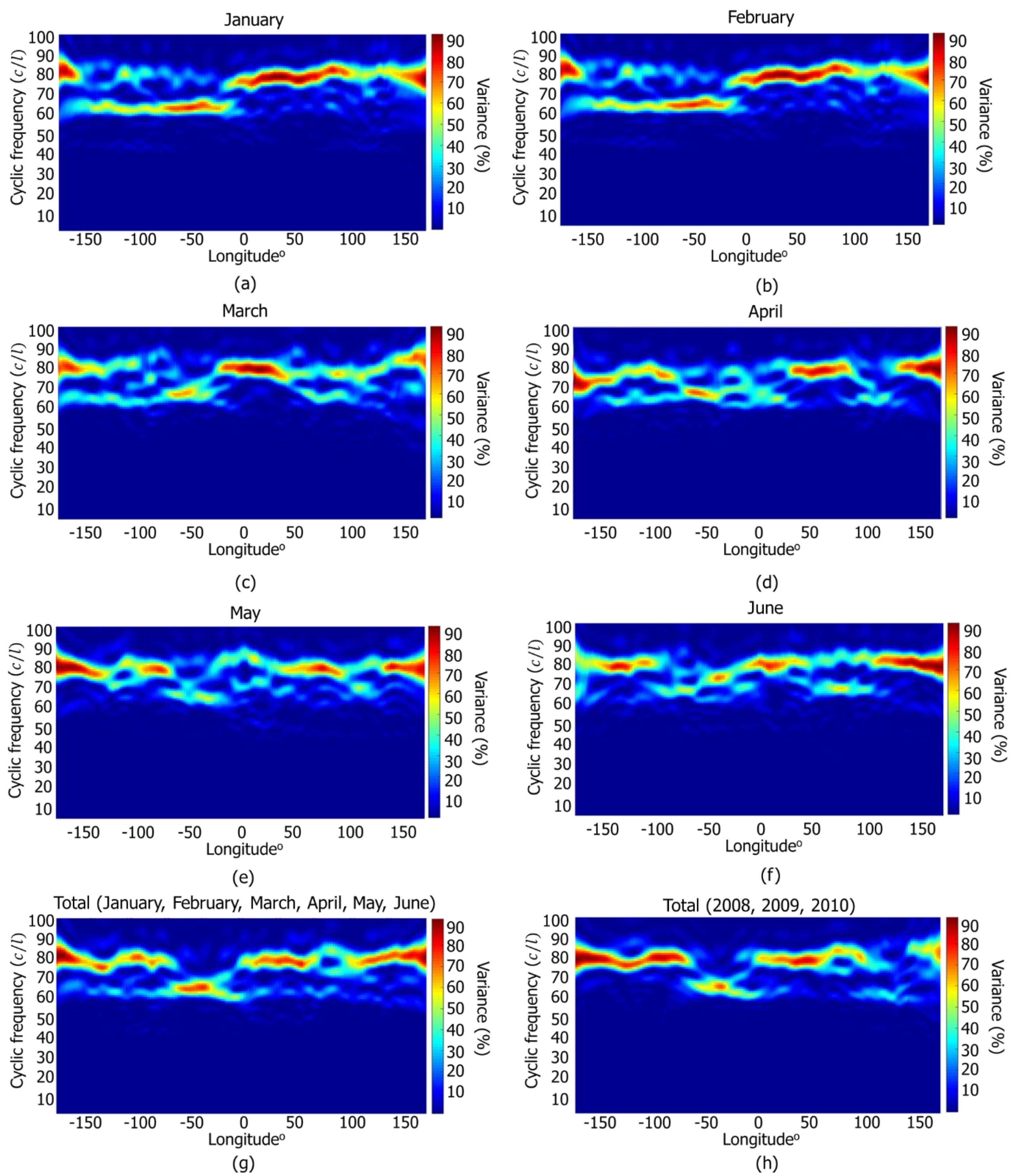

Figure 5.5: a-f) LSWA scalograms of stripes longitudinal profiles at $\phi = 30^{\circ}$ between January to June 2010; g) LSWA scalogram of the stripes sum between January to June 2010; h) LSWA scalogram of the stripes sum between 2008-2010.

Differences in phase reveal the spatial differences (i.e., space lag) of the stripes and provide information about their spatial translation over time. In Figure 5.6, we display two LSCWA scalograms and phase shifts between two random profile pairs namely, February-March and April-May 2010. The same process is applied to other pairs of monthly solutions within the 36 monthly series and results are very similar regardless the input monthly pairs. As expected, the highest coherence between any two consecutive months appears at the frequencies of 63.5, 76.7 and 79.4 c/ℓ. The areas with the largest phase differences are located between $-50^{\circ} \leq \lambda < 50^{\circ}$, where we observe a high coherence between the two signals.

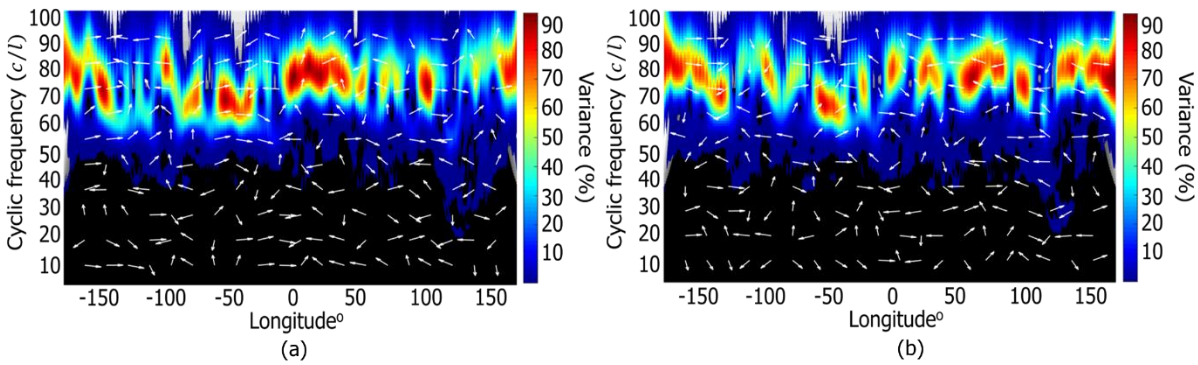

Figure 5.6: a) LSCWA spectrum between February and March 2010 longitudinal profiles at $\phi = 30^{\circ} N$; b) LSCWA spectrum between April and May 2010 longitudinal profiles at $\phi = 30^{\circ} N$. The analysis is done for 99% confidence level. Note that arrows in the first or second quadrant of the trigonometric circle denote $0^{\circ} \leq \psi < 180^{\circ}$, and arrows in the third or fourth quadrant denote $-180^{\circ} \leq \psi < 0^{\circ}$.

5.4 Moiré theory and GRACE sampling characteristics: The geometric approach

From a geometric perspective, an interesting type of moiré fringes can take place when two traveling waves with similar spatial frequencies interfere. The interference leads to a process called *spatial modulation* (Dos Santos, 2002), which drives beating artifacts. The interference may happen either by the additive, the subtractive or the multiplicative superposition type of grids (Patorski et al., 2011). We now need to understand the behaviour of GRACE ground tracks and then examine if their interference may lead to beating artifacts.

GRACE and other LEO satellite ground tracks have been thoroughly studied by Klokočník et al. (2008; 2013); Wagner et al. (2006); Weigelt et al. (2009) and Gooding et al. (2007). Some of the very interesting findings from these studies suggest that: 1) GRACE ground track resonance impacts the performance of the monthly gravity field models. That is, critical resonances, such as $\beta{:}\,\alpha$ equal to 61:4 and 107:7 (with β and α being co-prime integers; β is the number of nodal revolutions per α nodal days) lead to accuracy degradation and limited spatial resolution; and 2) the density of the ground tracks at the Equator is given by $1/D$, where $D = 2\pi R/\beta$ in km and β is the number of nodal revolutions (from an ascending node of the orbit to the next one). The quantity D resembles the longitudinal distance of the same direction (ascending or descending) satellite tracks at the Equator (Farless, 1985). In reality, the longitudinal distance of the ground tracks varies with respect to latitude, a behaviour that makes the determination of a fixed sampling interval a rather challenging task. This constraint is further discussed in Section 5.5.3.

We now begin with the study of the geospatial characteristics of the daily ground tracks during January 2010, given in Figure 5.7, by displaying the GRACE ascending (blue) and descending (red) ground tracks. Visually, the tracks display an elongated diamond-like pattern intercrossing approximately at latitudes $\phi = -75^{\circ}, -40^{\circ}, 0^{\circ}, 40^{\circ}, 75^{\circ}$. Additionally, in the zoomed Area 1 of Figure 5.7, it can be seen that the ground tracks form "bundles" of overlaid daily tracks (~ 15 tracks per day). Interestingly, there are 105 bundles of tracks across the globe, a number that is similar to the number of stripes found in each month (see Figure 5.2). Each bundle consists of approximately 4 tracks. It takes 7 days for a track to cluster (interlace) in a bundle[8]. We argue that the GRACE bundling of the ground tracks is connected to the presence of stripes on GRACE-based gravity models, in a caused and effect relationship. To prove this relationship, we delve into GRACE ground tracks structure to identify the mechanism that leads to stripes. Our hypothesis therefore postulates that the monthly translation of stripes is proportional to the ground track translation.

In the GRACE case, the spacecraft orbits result in clustering of daily ground tracks in bundles. The bundles are formed by translated and rotated daily tracks superposed upon one another, a structure that mimics a travelling wave. The interference between the travelling waves (superposed ground tracks) leads to pseudo-moiré (constructive and destructive) fringes that show in the

[8] Note that these numbers might be different for other monthly solutions, as GRACE orbits were variable with respect to time.

sampled signal as beating artifacts (Dos Santos, 2002). This process is widely known in the optics sciences and explained in many optics textbooks (see e.g., Hecht, 1998).

To describe the mechanism that drives fringes due to overlaid daily ground-tracks, we estimate the wavelength and direction angle of the nominal fringes (ground tracks) using moiré pattern formulation, and we compare it with the spectral characteristics of the stripes (wavelength and direction angle). After all, moiré interference patterns remind us of the GRACE stripes, where fringes (stripes) interchange between constructive (crests) and destructive (troughs).

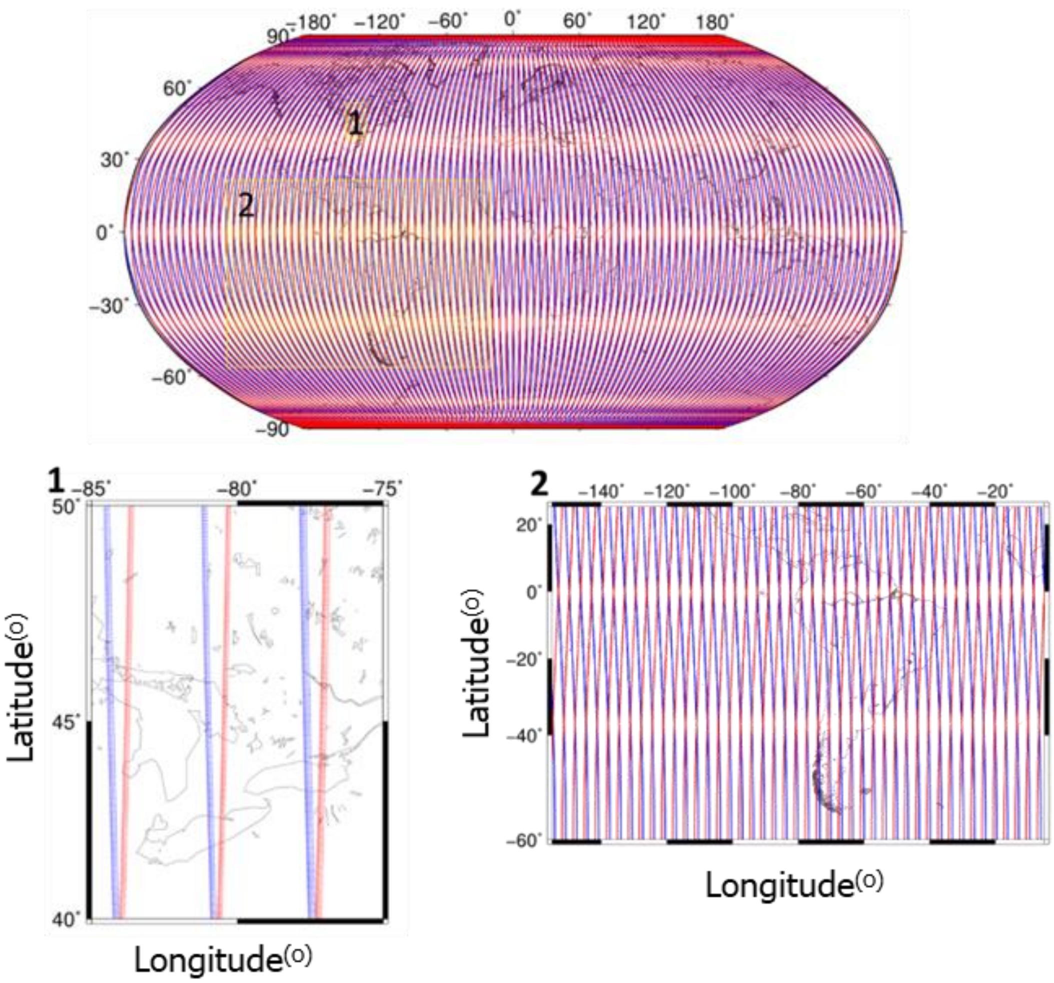

Figure 5.7: Ground tracks of GRACE-A during January 2010. Ascending tracks are noted with blue and descending with red; Zoomed Area 1 depicts in detail the “bundling” of the ground tracks; Zoomed Area 2 highlights the diamond like shape of the bundled tracks.

We calculate the angle between the ground tracks and the equatorial plane and the periodicity of ground track bundles to be able to derive the wavelength λ_{beat} and the direction angle θ of the moiré fringes. The bundle wavelength between same direction orbits (ascending or descending) is approximately $3^{\circ}25'$ which equals the 105 same direction bundles per length, i.e., $f = \frac{105}{360}\ c/\ell$. In Section 5.5 it is shown that the bundle frequency defines the latitudinal spatial sampling frequency of GRACE. The direction angle[9] of each bundle describes the angle between the overlaid ground tracks and the equatorial plane, which for GRACE orbits is approximately $\theta \approx 89^{\circ}$. Overall, the frequency vector $\boldsymbol{f}$ of the n superposed daily ground tracks reflects the vectorial sum of the frequencies of the n days and comprises two Cartesian components (Amidror, 2009):

$$u = f_1 cos\theta_1 + \cdots + f_n cos\theta_n, \tag{5.1}$$

$$v = f_1 sin\theta_1 + \cdots + f_n sin\theta_n. \tag{5.2}$$

The GRACE ground track sampling frequency is approximately the same every day, i.e., $f_1 \approx f_2 \approx \cdots \approx f_n \approx \frac{105}{360} c/\ell$ and the ground tracks have the same direction angle $\theta_1 \approx \theta_2 \approx \cdots \approx \theta_n \approx 89^{\circ}$. Now the frequency and the direction angle of the moiré fringes are given as:

$$f_{\text{beat}} = \sqrt{u^2 + v^2}, \tag{5.3}$$

$$\theta_{\text{beat}} = \arctan\left(\frac{v}{u}\right). \tag{5.4}$$

As the moiré fringes occur due to the vectorial sum (addition type) of the daily ground tracks, Equations (5.3) and (5.4) can be simplified in geometrical formulas that equally describe the frequency (f_{beat}) and the direction angle (θ_{beat}) of moiré fringes (Nishijima and Oster, 1964). The spatial period of the ground tracks is defined as $T = \frac{1}{f}$ and for simplicity we look only into the case where two grids are overlaid. Let us now define the beat frequency and direction angle from two overlaid ground tracks given in Equations (5.5) and (5.6):

$$T_{\text{beat}} = \frac{T_1 T_2}{\sqrt{{T_1}^2 + {T_2}^2 - 2T_1 T_2 cosa}}, \tag{5.5}$$

$$\theta_{\text{beat}} = \arctan\left(\frac{T_2 sin\theta_1 - T_1 sin\theta_2}{T_2 cos\theta_1 - T_1 cos\theta_2}\right), \tag{5.6}$$

[9] The direction angle is also known as screen angle and shows the direction that the sampled points are aligned (Amidror, 2009).

where a=$\theta_2 - \theta_1$. Note that special cases where $\theta_n = \cdots = \theta_2 = \theta_1$ and $T_n = \cdots = T_2 = T_1$ can also be considered further simplifications of Equations (5.3) and (5.4) (Amidror, 2009; Equations (2.9)-(2.11)).

The beat wavelength (λ_{beat}) of the fringes is similar to the wavelength of stripes estimated with LSSA. Additionally, we estimate the direction angle of stripes to be approximately 89^{o}. We derive this by measuring the azimuth angle of the stripes. Therefore, the stripes are correlated to the geometry of the GRACE ground tracks as it has been suggested in previous studies (see e.g., Watkins et al., 2015). Figure 5.8 depicts how the moiré pattern leads to constructive and destructive fringes. The notation p_s is used for the distance between the bundles and p_m for the half-wavelength of fringes.

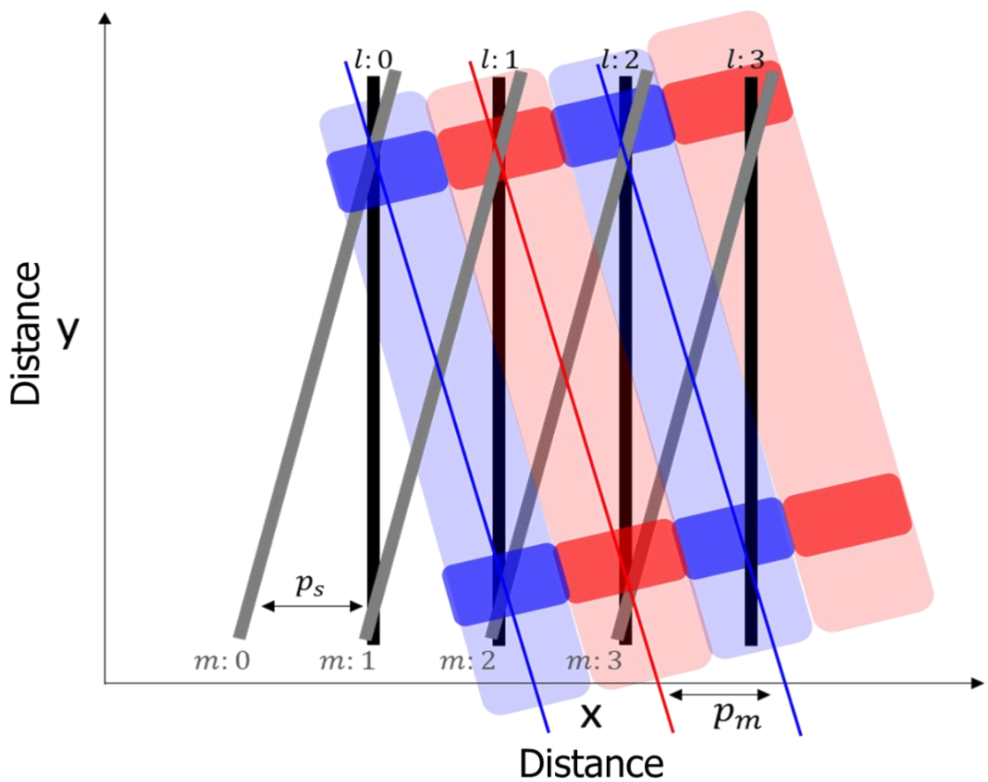

Figure 5.8: Schematic representation of constructive and destructive fringes induced by moiré pattern. l (black line) and m (grey line) denote the ascending and descending bundles, respectively. Constructive and destructive fringes are displayed with red and blue colour, respectively. Note that in areas that l and m intercross, the magnitude of fringes peaks. The thin red and blue lines resemble the direction of the fringes.

The relatively good agreement between the ground-track induced moiré fringes (105 fringes) and the GRACE stripes (~96 full wavelength stripes) is an indicator of the direction we need to follow to find the source of stripes. Additionally, in Section 5.5 we show that in the sampled gravitational signal derived from GRACE (cf., Figure 5.16), we count 105 stripes which perfectly matches the number of fringes derived from the ground tracks.

In general, the moiré fringes describe the result of the superposition of two (or more) grids. The overlay process is done through wave interference between two (or more) input units. Based on the longitudinal drift (translation or 'travelling') of the daily ground tracks, this interference results in constructive and destructive waves. Creating interference waves from the daily ground track is challenging since the ground track geometry is not per se a wave but rather it can be perceived as a binary pattern in a 2D space, where the locations with ground tracks present are assigned the value of one (unity) and the locations with no ground tracks present are assigned the value of zero. To overcome this limitation, we model the ground tracks as binary units that resemble a square wave. We then transform the binary square wave to a sine-like pulse by employing a smoothing spline function. The spline function is described in Equation (5.7) and the smoothing parameter p applied to the function is given in Equation (5.8):

$$s(x) = ax^3 + bx^2 + cx + d, \tag{5.7}$$

$$p \sum_i (y_i - s(x_i))^2 + (1-p) \int \left(\frac{d^2 s}{dx^2} \right)^2 dx, \tag{5.8}$$

with, a, b, c, d being the polynomial coefficients; x being the longitude $[0^\circ\ 360^\circ]$; $s(x)$ the spline function; p the smoothing parameter that ranges between [0 1]; and y the binary square waves across the longitude $[0^\circ\ 360^\circ]$. In our analysis the p value was set to 0.6. Note that the higher the value of p the rougher is the fit and the smaller the p the smoother the fit, respectively.

Afterwards, we sum the sine-like waves in a month that represent the translating daily ground tracks and derive constructive and destructive waves (fringes). Our analysis of January 2010 tracks, shows a ground track "wave" that consists of 105 full wavelength fringes. Figure 5.9 demonstrates the steps followed to estimate moiré fringes from GRACE ground tracks along $\phi = 30^\circ$N . In Figure 5.10 the profile of the fringes along $\phi = 30^\circ$N is presented.

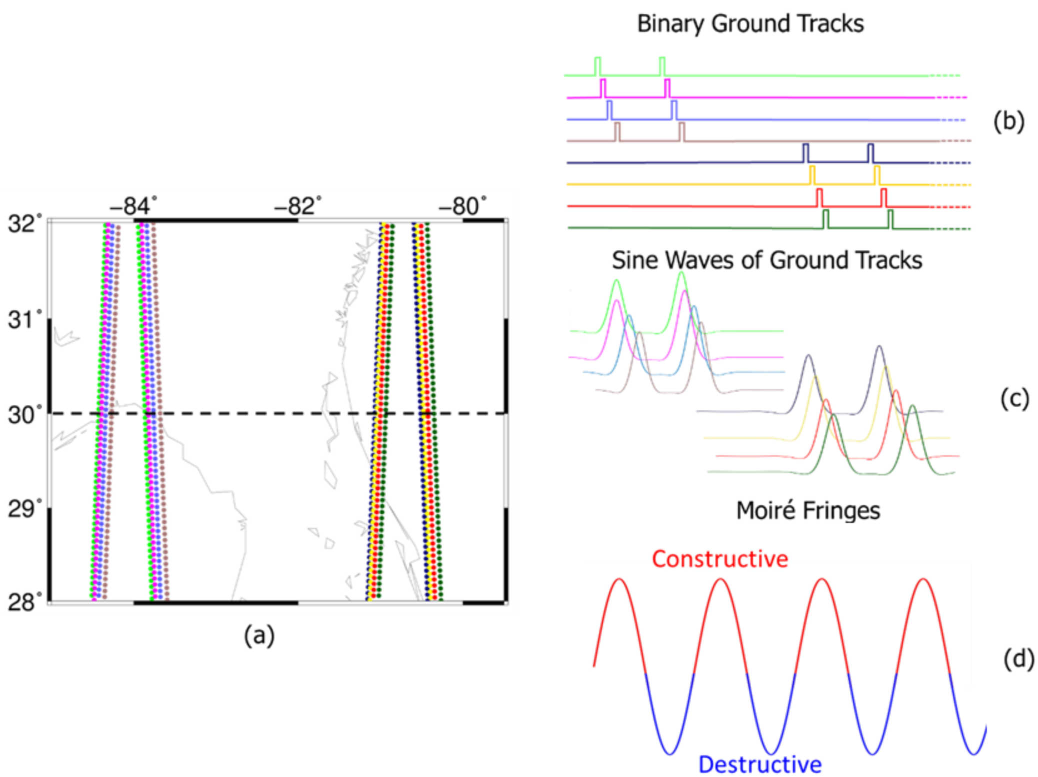

Figure 5.9: a) GRACE-A ascending and descending ground tracks on January 2010. Each day is assigned a different colour; dashed line indicates the longitudinal profile on which the fringes are estimated; b) Binary representation of the tracks; c) Sine-like waves of the ground tracks; d) moiré fringes derived by superposition of the daily sine waves (tracks).

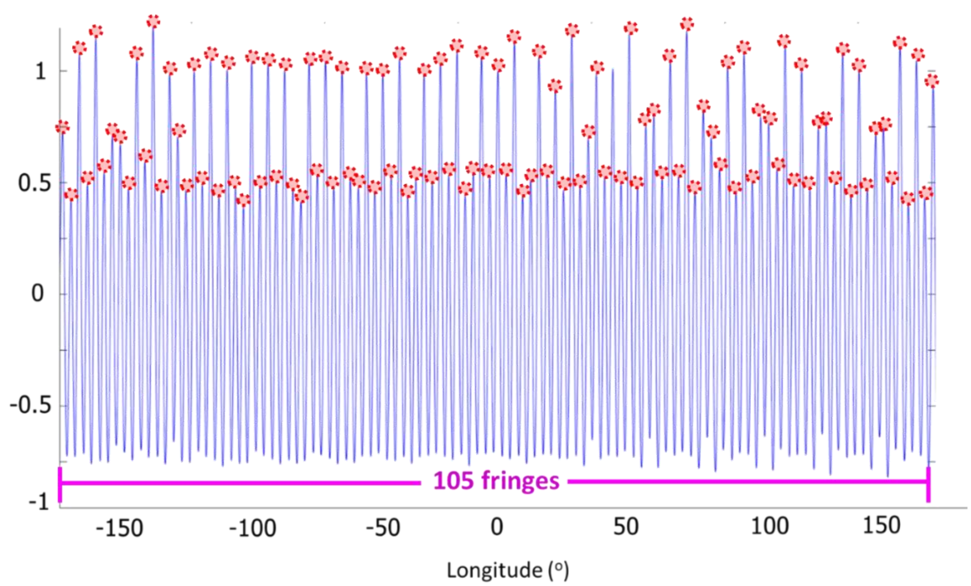

Figure 5.10: Moiré fringes from GRACE ascending ground tracks along $\phi = 30^{\circ}N$. Red dashed circles denote the crests of the fringes.

As a final step to better understand the relationship between GRACE stripes are moiré interference fringes, we derive the latitudinal profile of moiré fringes (see Figure 5.11) and apply LSCWA between the estimated interference fringes and latitudinal stripe profiles as derived from double differencing the positions derived from the GNV1B files along each axis . Specifically, the total acceleration of each spacecraft is derived along the three axes (x,y,z) and then the difference between the accelerations of the two spacecraft suffers from stripes (see Section 5.5 for more details). The stripes along the z-axis are displayed in Figure 5.11a. Interestingly, there are 105 stripes across the globe. Therefore, we use the stripes shown on the sampled signal to assess their similarity with the moiré fringes made using the geometry approach. The results shown in Figure 5.11b demonstrate the coherence of the ground tracks wave interference with stripes during January 2010 for the latitudinal profile along the parallel $\phi = 45^{\circ}N$. The coherence between the two input signals reaches nearly 70% in the near the frequency of 105 c/ℓ.

The moiré geometry approach gives us a good idea of the relationship between the stripes and the ground tracks. Overall, the relatively high coherence between stripes and moiré fringes clearly indicates the good match between stripes and GRACE ground tracks. To this end, it can be now more clearly that there is a strong correlation between the GRACE orbits and the stripes, as is often mentioned but never proved in the literature.

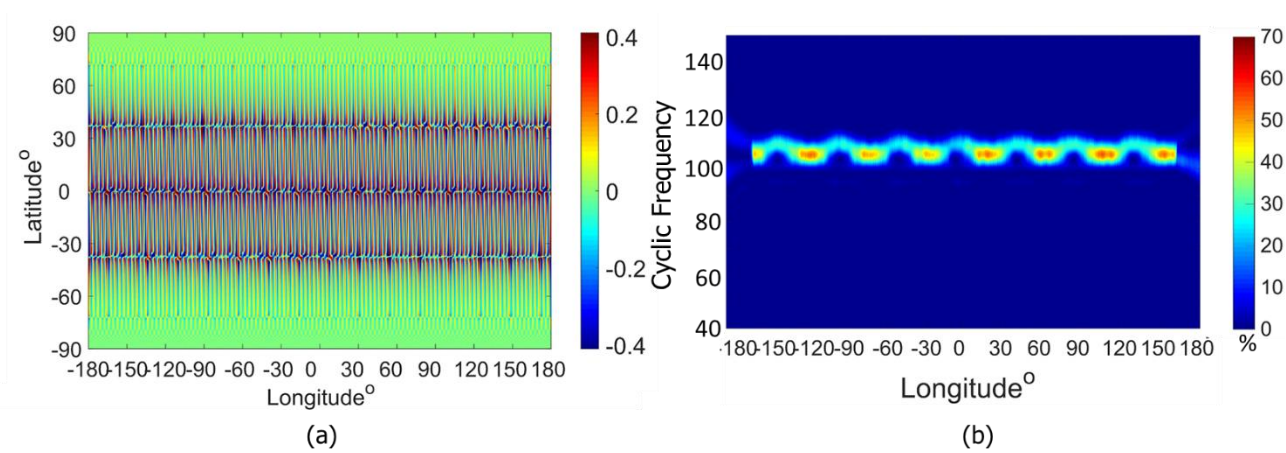

Figure 5.11: a) Difference between GRACE A and GRACE B total accelerations derived from the precise orbits (POD) along z-axis in ITRF during January 2010; b) LSCWA along the latitudinal profile at $\phi = 45^{\circ}N$ between POD derived accelerations (cf., Figure 5.11a) and moiré fringes created using GRACE ground tracks of January 2010.

5.5 Moiré theory and GRACE sampling characteristics: The Fourier approach

In Section 5.4 we showed that the GRACE ground track geometry may lead to moiré artifacts and we quantified the relationship between stripes and GRACE ground track geometry by applying coherence analysis along various latitudinal profiles. A good match between GRACE stripes and moiré interference fringes signals that in fact moiré and sampling theory may explain the artifact of stripes. We now need to fully understand the mechanism that introduces stripes. To achieve this, the Fourier approach of moiré theory will be employed. Fourier (or spectral) approach is the most powerful approach to describe sampling artifacts mainly due to its effectiveness to examine a sampled signal in space from the perspective of both space and frequency domains (Amidror, 2009). Therefore, we will examine how GRACE samples the gravitational field in space (i.e., along the ground tracks and along the parallels), and employing Fourier approach formulation, the mechanism that drives stripes will be explained.

5.5.1 Heuristic observations and fundamental hypothesis on the origin of stripes

Our analysis is guided by heuristic, yet fundamental observations on the spatiotemporal characteristics of the stripes discussed in Sections 5.3 and 5.4. Our observations are made on the results of the analyses of 36 GRACE monthly solutions between 2008-2010. We summarize the findings of this analysis in points (1)-(6):

1. The ground tracks of GRACE form longitudinal bundles, whose latitudinal spatial frequency defines the sampling frequency f_s of the gravitational signals along the parallels of latitude. The bundles are formed by the superposition of translated and rotated daily tracks. We count 105 ascending and 105 descending such ground track bundles in a monthly data set. We also note, that there are 15 complete tracks per day, and it takes about 7 days for a track to be superposed (added) on the same bundle, thus in a month there are typically 4-5 interlaced tracks in a bundle $(30/7)$. This geometry is not fixed throughout GRACE lifetime and monthly orbits from previous or following years may follow different ratio from 30/7. Furthermore, we note that the longitudinal translation of the superposed ground tracks resembles (mimics) a travelling wave in space.

2. The stripes are nearly longitudinal and are aligned with the GRACE ground track bundles, thus they appear as a latitudinal wave. Albeit somewhat difficult, we count about 96 stripes (crests) globally in a few random monthly models (e.g., from RL04 d/o 120 field). Remarkably, the number of stripes appears to be close to the number of the same direction (e.g., ascending) ground track bundles and is also nearly identical to the maximum d/o used for RL05 solutions[10].

3. To further substantiate and expand the above observation, we take a GRACE model that is currently available, namely RL05 of d/o 96. We are fully aware that RL05 contains a smaller number of much fainted stripes, but we are only interested in examining consistency of their spectral characteristics in time and around the globe. To enhance the stripes for more reliable analysis, the filtered field is subtracted from the total one (e.g., Kusche, 2007). Afterwards, we perform least-squares spectral and wavelet analyses (Ghaderpour et al., 2018; Ghaderpour and Pagiatakis, 2017) of 36 consecutive monthly stripe profiles (years 2008, 2009 and 2010), along $\phi = 30^{\circ}$, to ensure that the spatial spectral characteristics of stripes remain constant. Remarkably, results showed that the stripes peak at nearly identical spatial frequencies over time, but with a consistent phase shift in all 36 profiles.

4. We calculate the scalogram (space vs. frequency) of the latitudinal profiles of stripes and show that they peak at the same frequencies, i.e., 63.5, 76.7 and 79.4 c/ℓ. Figure 5.12 shows the scalogram of one month namely, January 2010. We notice magnitude variations (colour scale), which suggests that although the wavelength of stripes is consistent, the magnitude is non-stationary. Furthermore, we detect a tendency of separation in space between the two main peaks indicating that they are not dominant at the same places, i.e., one exhibits strong magnitude when the other is weak and vice versa. Interestingly, the behaviour of these peaks agrees with the peaks of the geoid profile. Of note is that at the longitudes where the geoid peaks, the frequencies shift, while in areas that the geoid peaks less, a split (separation) of frequencies is detected.

5. We superpose the 36 monthly profiles mentioned above on one profile, whose least-squares scalogram (space vs. frequency; Ghaderpour et al., 2018) displays spectral peaks at precisely the same frequencies as the monthly ones. According to the addition theorem of Fourier theory

[10] d/o of RL05 solutions lowered from d/o 120 to 96 due to the 7-day repeat orbit that peaked at 12/2009 (Dahle, 2014).

(Bracewell, 1978), this finding provides proof that the stripes possess the same spectral characteristics in time (linear system) although their amplitude and phase are non-stationary. The stripes show a traveling, wave-like pattern that translates proportionally to the eastward drift of the ground tracks. That is, the spatial position of the stripes, changes with time and correlates with the variable position of the ground track bundles.

6. The stripes remind us of moiré fringes, such as the ones we observe in the interferometric synthetic aperture radar (inSAR) images and other phenomena. These fringes are not the result of aliasing, rather they are the result of interference of two or more signals.

Considering the observations and the analysis of stripes in points (1)-(6) made above, and having always in mind the sampling and moiré theories as described in Bracewell (1978; 1995), Amidror (2009) and Theocaris (1969), as well as in scientific papers on moiré theory by Amidror (2013; 2015), we form the following hypothesis on the origin of GRACE stripes:

The stripes are pseudo-moiré or sub-Nyquist artifacts (modulated signals) that are produced by the latitudinal spatial sampling frequency of the ground track bundles that sample a low frequency gravitational signal.

Sub-Nyquist artifacts are a special type of sampling artifacts. In Section 5.5.2 we discuss the three types of artifacts that may be driven by the sampling characteristics of GRACE and focus is placed on the poorly studied sub-Nyquist artifacts, as our hypothesis postulates that this type of artifacts drives stripes on GRACE models.

5.5.2 Sampling Artifacts

In the GRACE peer reviewed literature, the stripes have been primarily attributed to aliasing, whether spatial and/o r temporal. According to the classical sampling theorem, all the information in a continuous signal $g(x)$ is preserved in its sampled version $g(x_k)$ if the sampling frequency f_s is at least twice the highest frequency contained in $g(x)$, a condition known as the Nyquist criterion (e.g., Amidror, 2015).

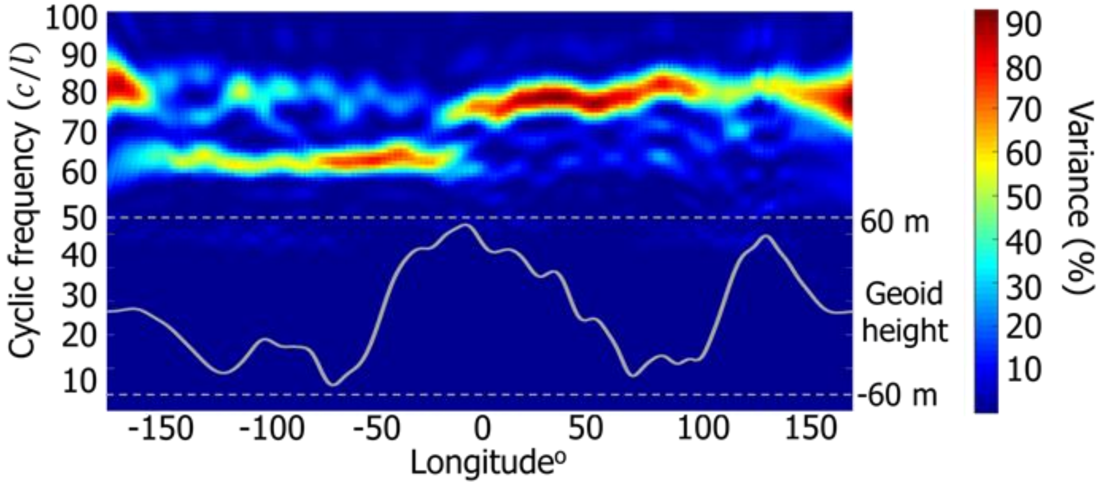

Figure 5.12: LSWA scalogram of latitudinal profiles of stripes at $\phi = 30^{\circ}N$ for January 2010. The latitudinal profile of the geoid (d/o 60) derived from GO_CONS_GCF_2_TIM_R5 (Brockmann et al., 2014) is shown within the grey dashed lines.

Any periodic component in $g(x)$ that violates the Nyquist condition (has frequency $f > f_s/2$) will fold-over to low frequencies as a false (aliased) peak of low frequency in the spectrum of the sampled signal $g(x_k)$. This process is commonly known as *aliasing* or *sampling moiré effect.* To understand what periodic signals can cause aliasing artifacts in GRACE models we first need to understand how GRACE samples the gravitational field.

In the GRACE experiment, the continuous function of interest is *gravitation* $g(P,t)$ in the spatio-temporal 4D domain, where P is 3D position (e.g., geodetic coordinates) and t is time. GRACE obtained a sample of the Earth's gravitation, i.e., $g(P_k, t_k)$, that depended on the orbit geometry and sampling frequency. Any periodic phenomena in $g(P,t)$ with frequencies higher than a critical Nyquist threshold will appear as low frequency aliases in the reconstruction of the gravitational field (spherical harmonics) from the sampled gravitation signal $g(P_k, t_k)$, through the process of the least-squares method. The fact that the functional $g(P,t)$ is defined in 4D domain makes the determination of the Nyquist threshold very challenging, if not impossible. Perhaps the only way to determine it is via simulations (Velicogna et al., 2011; Zenner et al., 2010). Therefore, more simplistic approaches of defining aliasing on GRACE models have been adopted. It appears that the determination of the Nyquist threshold has not been searched adequately and it is poorly understood.

Aliasing effects on GRACE solutions have been studied in-depth, and many anti-aliasing force models have been tested and employed in the reconstruction phase of $g(P,t)$ (see, e.g., Dobslaw et al., 2013). To avoid temporal and spatial aliasing effects on GRACE models, periodic mass redistribution phenomena, such as tides, atmosphere and hydrology, are modelled (force models) and removed from $g(P_k, t_k)$ prior to the reconstruction of the signal (Han et al., 2004; Seo et al., 2008; Wiese, 2011).

Although these aliasing sources are known and removed from the final solutions, analyses show that residual artifacts with low frequency and low magnitude still exist in the final solutions (Han et al., 2004). These aliasing effects are not to be confused with the stripes that dominate GRACE solutions, because the stripes have very different spectral characteristics (see Section 5.3) and their magnitude is negligible compared to the magnitude of the gravitational field (ibid, 2004). Therefore, the surmise that the stripes showing in the reconstruction of $g(P,t)$ from the sampled signal $g(P_k, t_k)$ are aliases, is rather an unsubstantiated hypothesis.

Overall, aliasing artifacts on GRACE models follow a north-south "stripy" pattern, however, their frequency and magnitude are considerably lower than the very dominant artifact present on GRACE solutions. Wiese (2011) distinguishes two different artifacts seen in the form of north-south stripes on GRACE models, calling the aliasing artifacts *striations*.

Interestingly, there are other possible 'artifacts' introduced by the sampling frequency, such as *borderline artifacts* and *sub-Nyquist artifacts* (Amidror, 2015). To the best of our knowledge these artifacts have never been considered in GRACE literature. As it turns out (see Section 5.6), the stripes are not aliasing effects but rather beating sub-Nyquist artifacts. Borderline artifacts occur when the frequency of a signal f is nearly equal to the sampling frequency, that is $f_s - f \approx 0$. Again, in this borderline case, aliasing occurs and the folded frequency $f_M = f_s - f$ lies nearly at the spectrum origin and has a very long wavelength.

Sub-Nyquist artifacts

The more complex type of beating artifacts, known as *sub-Nyquist* (*pseudo-moiré*) artifacts, may appear in the sampled signal $g(P_k, t_k)$, even if the sampling frequency f_s fully satisfies the Nyquist criterion. To understand the *sub-Nyquist artifacts,* the reader is referred to the excellent work by Amidror (2015) that provides a rigorous in-depth exploration of the *sub-Nyquist* artifacts supported by many illustrative examples. Sub-Nyquist artifacts are driven by amplitude modulation of a carrier (high frequency) wave by an information (low frequency) signal. The artifacts are created only when the sampled signal comes from a superposition of grids (ground tracks) (Patorski et al., 2011).

In the frequency domain, the key point is that beating or sub-Nyquist artifacts may appear in $g(P_k,\ t_k)$ when $g(P,t)$ contains a periodic (or pseudo-periodic) signal of frequency f and is sampled with a frequency f_s, when f_s *does* respect the Nyquist condition, i.e., $f \approx \frac{1}{2} f_s$ (borderline artifacts), or it is close to $\frac{m}{n} f_s$, i.e., $f = \frac{m}{n} f_s + \varepsilon$ (ε is a small frequency increment, positive or negative), where *m* and *n* are integers, and $2m \leq n$ (this inequality excludes aliasing effects). That is, each time the signal with frequency f approaches the critical frequency $\frac{m}{n} f_s$, the sampled signal experiences beating artifacts. The value ε signifies the difference between f and $\frac{m}{n} f_s$ and shows in the sampled signal domain as a modulating envelope of low frequency $f_{env} = \varepsilon$. There are *n* such interlaced envelopes with a phase difference equal to $m/n\varepsilon$.

The beating artifacts are formed when successive sampled points of the original continuous signal (carrier signal) fall alternately onto the *n* interlaced envelopes formed by a modulating signal (information signal) of low frequency f_{env}, leading to false highly oscillating waves that are visible in the sampled signal. These false waves are in fact the sub-Nyquist artifact (for the GRACE example this artifact shows as stripes) with frequency $f_{beat} = \frac{m}{n} f_{env}$.

GRACE is in fact in the sub-Nyquist sampling milieu in which there is a quasi-periodic low frequency gravitational signal (information signal) that modulates the GRACE sampled signal (carrier signal) and leads to sub-Nyquist artifacts. GRACE ground tracks (sampler) follow a travelling wave pattern (they drift eastward) and in any gravitational solution (monthly or long-term) we count 15 tracks per day clustered successively in a ground track bundle every 7 days (note that the 7 days depend on the mission's orbit and change with respect to time). The interference between the traveling wave (sampler) and a low frequency quasi-periodic gravitational signal leads to pseudo-moiré fringes that show in the sampled signal as beat artifacts, a process widely known in the optics sciences and explained in many optics textbooks (see e.g., Hecht, 1998).

Overall, sub-Nyquist artifacts have the following properties (Amidror, 2015):

a) They appear even when the Nyquist condition is fully satisfied (in that case no aliasing is expected).

b) Their periods cannot be seen in the spectral domain but are clearly visible in the signal domain.

c) They result in high frequency sine waves modulated by low-frequency envelopes.

Let us now visualize the conditions under which a signal experiences sub-Nyquist artifacts, and the mechanism that results in these artifacts. To see how these artifacts are introduced in the sampled signal, let $g(x)$ be a random signal (periodic or quasi-periodic), with sampling frequency f_s. While sampling $g(x)$ there are $n = 7$ number of interlaced envelopes of a very low frequency signal; and for simplicity we set $m = 1$. In Figure 5.13 each envelope is denoted with a different colour and the phase difference between the envelopes is $m/n\varepsilon$ where ε is the frequency of the envelope. In this case, the sub-Nyquist artifacts shown in the final signal are induced by sampling the very low frequency signal, in the "dangerous" neighbourhood $\frac{m}{n} f_S$.

The envelopes are nothing more than stretched and shifted versions of $g(x)$ driven by a very low frequency signal with frequency f_{env} . In Figure 5.14a we show in detail how the successive sampled points fall alternately onto the interlaced envelopes creating sub-Nyquist artifacts. That is, for $n = 7$, the 1^{st},8^{th},15^{th}, etc. sampled points fall into the first envelope, the 2^{nd},9^{th}, 16^{th} points, etc. fall onto the second envelope, and so on. In the zoomed area shown in Figure 5.14b we demonstrate how the sampled points from the consecutive interlaced envelopes lead to sub-Nyquist artifacts (red colour). In essence, the final sampled signal is contaminated by a *pseudo-signal* created by the amplitude modulation of the sampled signal (sampled points) by the low frequency envelopes. The phase difference between two envelopes equals $a = \frac{m}{n\varepsilon}$ and shapes a distinct structure within which there are m highly oscillating waves.

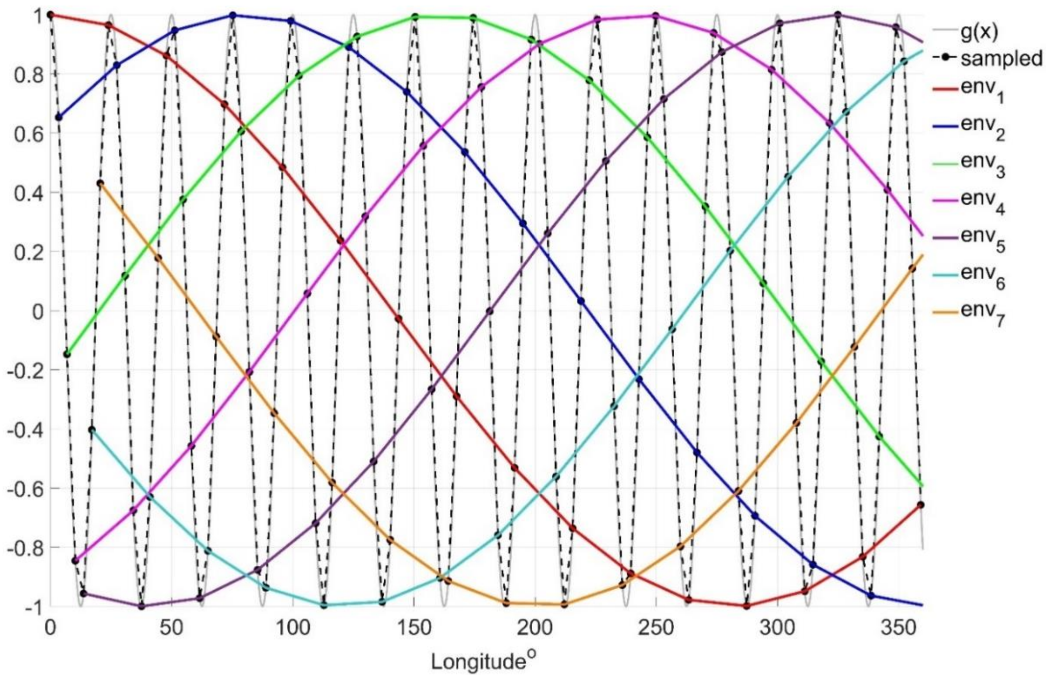

Figure 5.13: The signal $g(x)$ is in grey color and its sampled version in black dashed line. The $n = 7$ modulating envelopes of the low frequency signal (ε) are shown in red, green and blue. The phase difference between the envelopes is equal to $m/n\varepsilon$.

The sub-Nyquist artifacts driven by the amplitude modulation of the sampled signal $g(x)$, by the low frequency envelopes, can be described by using Equation (5.9):

$$SubNyquist = cos\left(2\pi\left[\frac{m}{n}f_{env}\right]\frac{k}{f_s}\right), \tag{5.9}$$

where $k = [0°, 360°]$; that is, k defines the sampling step for each latitudinal profile (when integrating along the Earth).

We now need to fully understand the role of the integers m, n in the final sub-Nyquist artifacts. In Figure 5.15 for the sampled function $g(x)$, we keep the sampling frequency f_s and the low frequency signal ε constant and generate sub-Nyquist artifacts for various m, n combinations using Equation (5.7). The artifacts resemble highly oscillating false signals that contaminate the sampled signal.

We note that the higher the integer m, the higher the frequency of the sub-Nyquist artifacts. On the other hand, higher number of interlaced envelopes n results in lower frequency artifacts. If $m > n$ then the artifacts are simple *sampling moiré artifacts* (aliasing).

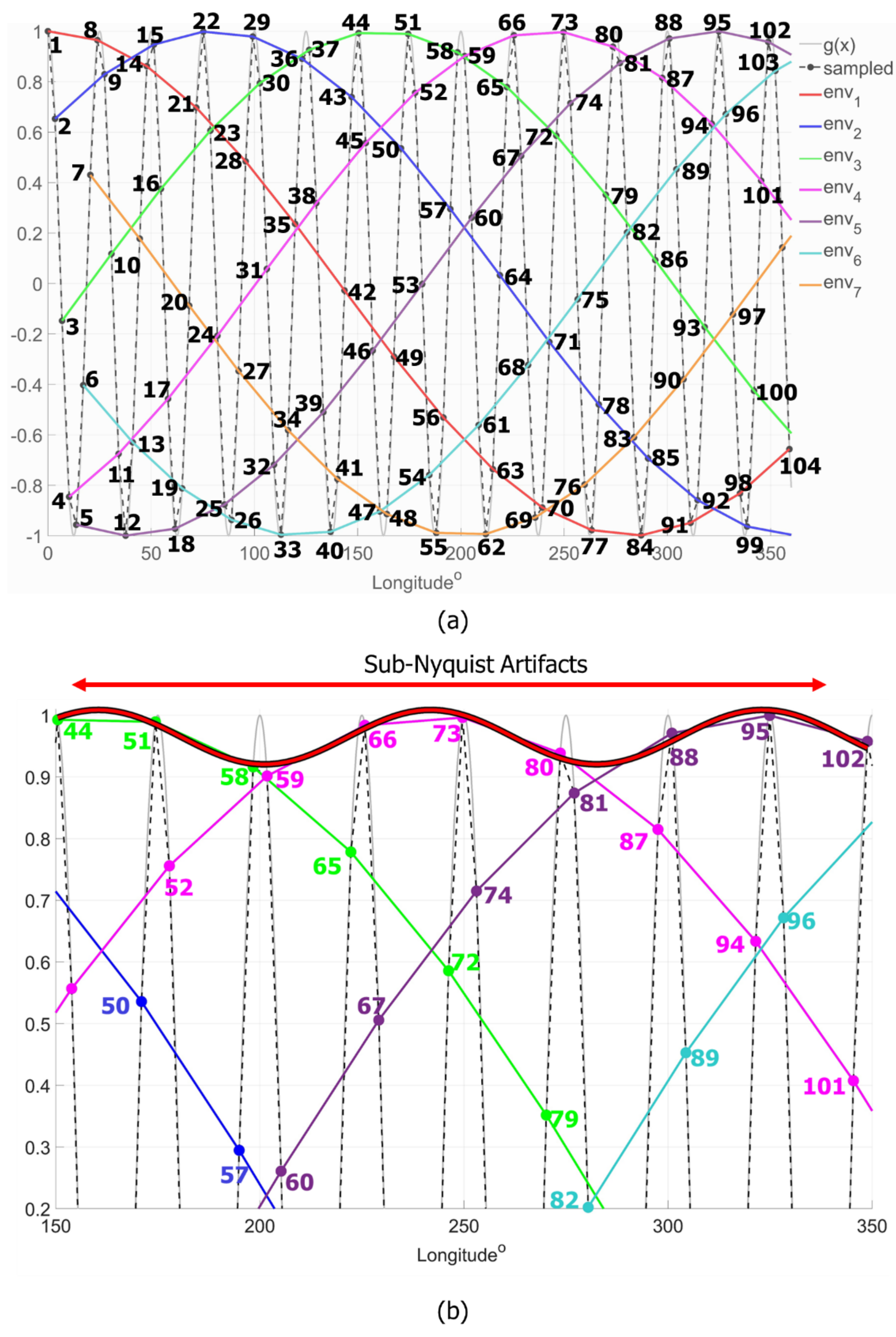

Figure 5.14: a) Visual representation of the “jump” of sampled points onto the interlaced envelopes. Each colour resembles a different envelope. Note that consecutive sampled points fall onto (jump to) a different envelope; b) Zoomed area of the sampled points and the modulated envelopes. The sub-Nyquist artifacts (red colour) driven by the modulation of the sampled signal shape an oscillating sine wave.

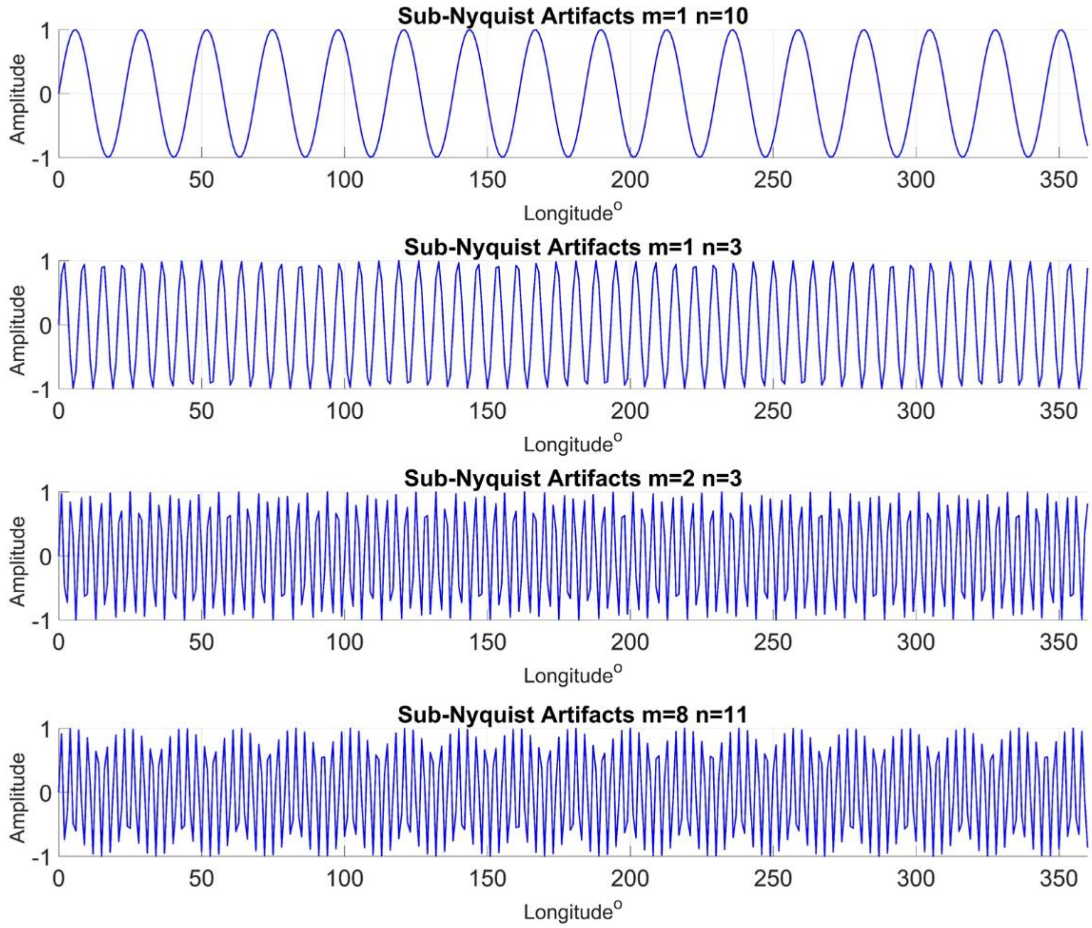

Figure 5.15: Sub-Nyquist artifacts for various combinations of m, n. Note that the artifacts generated are synthetic and therefore unitless.

To fully understand how GRACE might be affected by sampling artifacts, we first need to understand and subsequently quantify how GRACE sampled *gravitation* $g(P, t)$. We commence with the study of the characteristics of GRACE gravitational accelerations $g(P_k, t_k)$ calculated by double time-differentiation of the precise orbits (POD) provided in GNV1B files for both GRACE spacecraft (i.e., the difference between the total accelerations of GRACE A and B). Figure 5.16 shows the total acceleration (gravitational plus non gravitational) and their amplitude spectral densities along the three ITRF axes, during January 2010.

Stripes are clearly evident in all three components. Their magnitude varies geographically, and their number is equal to that of stripes in the monthly solutions (i.e., approximately 105 positive and negative stripes): We count 15 distinct structures across the globe shaped from the ground track nodes (*vis*., Figure 5.16h), each of which contains 7 *stripes*.

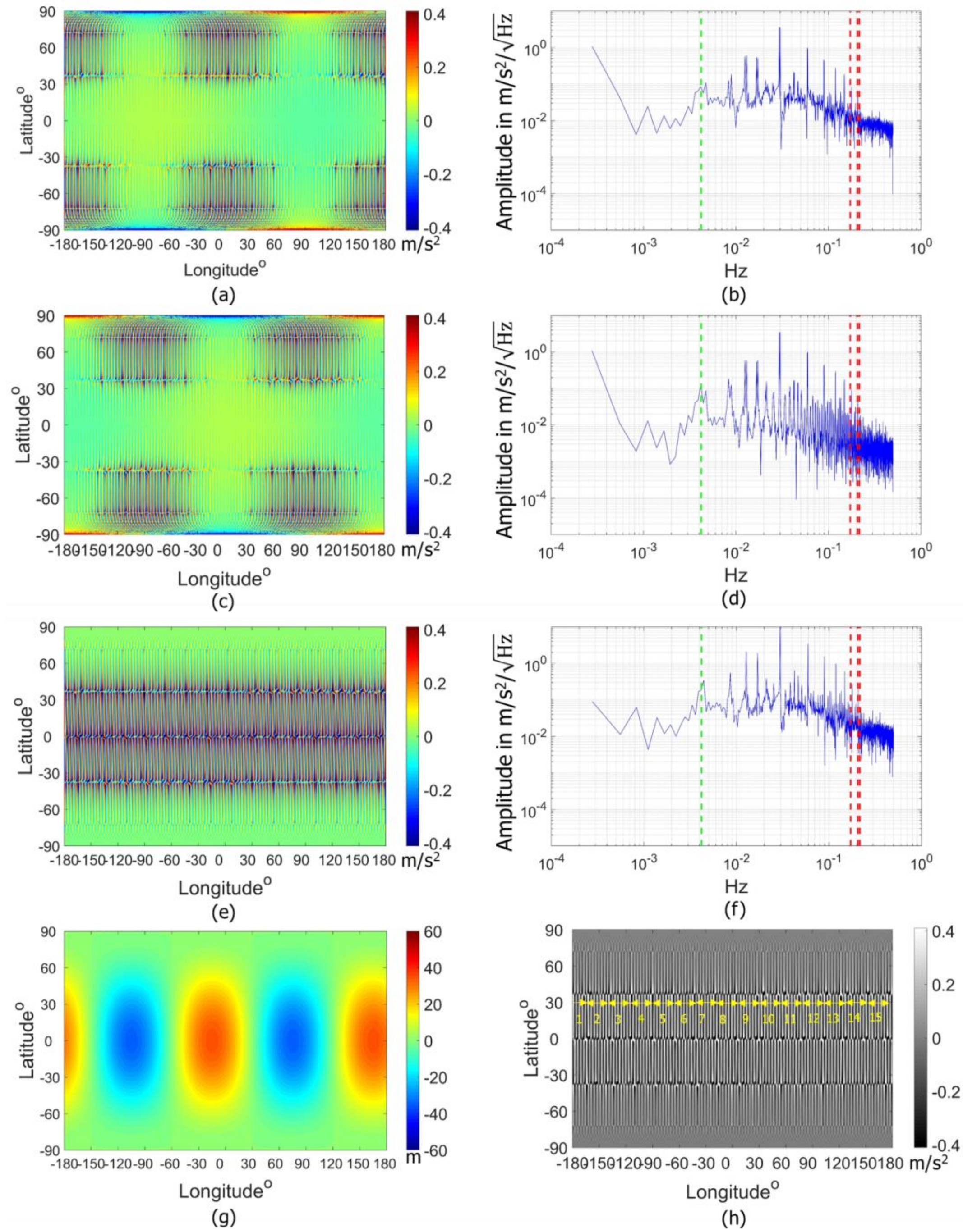

Figure 5.16: Difference of the total accelerations derived from the precise orbits (POD) of the two spacecraft along (a) x-axis (a_x); (c) y-axis (a_y) and (e) z-axis (a_z), in ITRF during January 2010. 2-D amplitude spectral densities of a_x, a_y and a_z (panels b, d, and f, respectively). Red dashed lines show the position of the three beating frequencies of stripes. The green dashed line denotes the latitudinal beating frequency of the disturbing potential (geoid) (~0.005 Hz); g) GO_CONS_GCF_2_TIM_R5 geoid calculated up to d/o 2; h) Total accelerations (a_z) in greyscale. Note the number and the distinct structure of the sampled accelerations highlighted with yellow arrows.

Interestingly, we notice that the stripes of the total accelerations along the x-axis and the y-axis (Figure 5.16a, 5.16c) have a pattern that appears to be closely related to the long wavelength structure of the geoid (*vis.*, Figure 5.16g; GO_CONS_GCF_2_TIM_R5 geoid) calculated up to d/o 2, and more notably related to its (latitudinal) sectorial structure. The positive values of the geoid coincide with the location of stripes of the measured accelerations along the x-axis, while the negative values coincide with the stripes present in the measured accelerations along the y-axis. We also note the peak of the magnitude of stripes along the latitudes, where GRACE ascending and descending ground tracks intercross (cf., Fig 5.16e; $\phi = -75^{\circ}, -40^{\circ}, 0^{\circ}, 40^{\circ}, 75^{\circ}$). The sampled total accelerations derived from GOCE POD do not demonstrate any sampling artifacts as GRACE does. This finding further validates that the origin of stripes lies in GRACE sampling characteristics and in particular, in the latitudinal sampling.

Additionally, we estimate the amplitude spectral density of the 2D gravitational accelerations for each accelerometer axis (see Figure 5.16b; d; f) and surprisingly there is no spectral peak at the frequency of stripes shown with red dashed lines. Therefore, the stripes are visible in the signal domain (see Figure 5.16a; c; e), but they are not present in the spectral domain. Considering that: a) the sampled gravitational signal is contaminated by stripes in the signal domain and not in the spectral domain, and b) the stripe pattern resembles a highly oscillating sine wave, we surmise that the stripes are in fact beating sub-Nyquist artifacts caused by the GRACE latitudinal sampling frequency. We note that the geoid (dashed green line in Fig 5.16b; d; f) is the gravitational signal of low frequency, oversampled by GRACE.

To prove the above findings, we need to simulate a sub-Nyquist artifact using GRACE sampling parameters. We remind the reader that the Equation that describes sub-Nyquist artifacts is as follows (Amidror, 2015):

$$f = \frac{m}{n} f_s + \varepsilon, \quad 2m < n. \tag{5.10}$$

For this we need to define: 1) the effective latitudinal sampling frequency f_s of GRACE; 2) a reducing integer ratio m/n that is the number of the modulating envelopes (n) and the number of stripes within each envelope (m); and 3) a very low frequency gravitational signal that GRACE samples with high sampling frequency.

5.5.3 GRACE latitudinal sampling frequency

GRACE follows, in principle, non-repeat orbits and therefore it is challenging to quantify its sampling frequency, especially in the space domain; after all, the Nyquist frequency is defined by the repeat period of the satellite orbit (Zenner et al., 2010). For more information on GRACE sampling, the interested reader is referred to the work of Klokočník et al. (2008) and Wagner et al. (2006). We analyze the ground tracks of 36 months and notice that in each month the ground tracks form "bundles" of daily tracks. Additionally, the distance between same direction bundles (ascending or descending) is approximately $3^{\circ}\ 25'$. This distance is almost constant in each month, slight deviations from this value do not impact our analysis. The geometry of the ground tracks follows a diamond-like pattern generated from the intercrossing of the ascending and descending bundles. This poses additional challenges for the definition of the latitudinal sampling frequency because the distance between ascending and descending bundles varies with latitude.

To fully understand how this complex geometry impacts the latitudinal sampling frequency of GRACE, we first assume that the ground tracks are equally spaced and we calculate the Poisson kernel of the upward continuation of gravity anomalies at GRACE altitude (Heiskanen and Moritz, 1967; Cruz and Laskowski, 1984). The upward continuation of gravity anomalies (Δg) using Poisson kernel is given as follows:

$$\Delta g(r,\phi,\lambda) = \frac{1}{4\pi}\iint_{\sigma} K(t,\psi)\Delta g(R,\ \phi',\lambda')d\sigma, \tag{5.11}$$

with $K(q,\psi) = \frac{q^2(1-q^2)}{D^3}$, $q = {}^{R}\!/_{r}$ and $D = (1 + q^2 - 2q\cos\psi)^{1/2}$

where R is the radius of the Earth; r is the distance of the spacecraft from the geocentre; ϕ', λ' are the geodetic coordinates at the Earth's surface; ϕ, λ are the geodetic coordinates at the spacecraft altitude; ψ is the angular distance between the point of interest (sub-satellite point) and the point of integration (i.e., ground tracks) with respect to the geocentre; and σ and $d\sigma$ resemble the dimensional measure and the integration area, respectively.

Figure 5.17 shows the results of the simulations using the normalized Poisson kernel, which quantify the scale of the gravitational signal that can be sensed by GRACE. We estimate the geometric separation (distance) of the ground tracks within a bundle, the variable distance between the ascending and descending bundles and the distance between the same direction (ascending or descending) bundles. The upward continuation Poisson kernel (defining a low pass filter) at GRACE altitude does not attenuate very fast with distance from the sub-satellite point (cf., geocentric angle). In fact, it drops below the -6dB power level at the average distance between two ascending (or descending) bundles indicating that at GRACE altitude the ground tracks within a bundle as well as between two adjacent bundles (ascending-descending) are not clearly resolved. The equally spaced latitudinal sampling interval that GRACE can achieve is the distance between the same direction bundles, that is approximately $\Delta_s = \frac{360}{105} = 3.43^{\circ}$.

The sampling frequency $f_s = 1/\Delta_s$ will be the starting value for our simulations of sub-Nyquist artifacts (stripes) followed by a frequency sweep through different values in either direction from f_s to observe its effect on the number of stripes such different frequencies produce. How the sampling frequency is determined is important to consider, given the complex geometry of the ground tracks and bundles (unequally spaced) as well as their interlaced character. As it turns out, this approach provides a reliable estimate of the effective latitudinal sampling rate of GRACE.

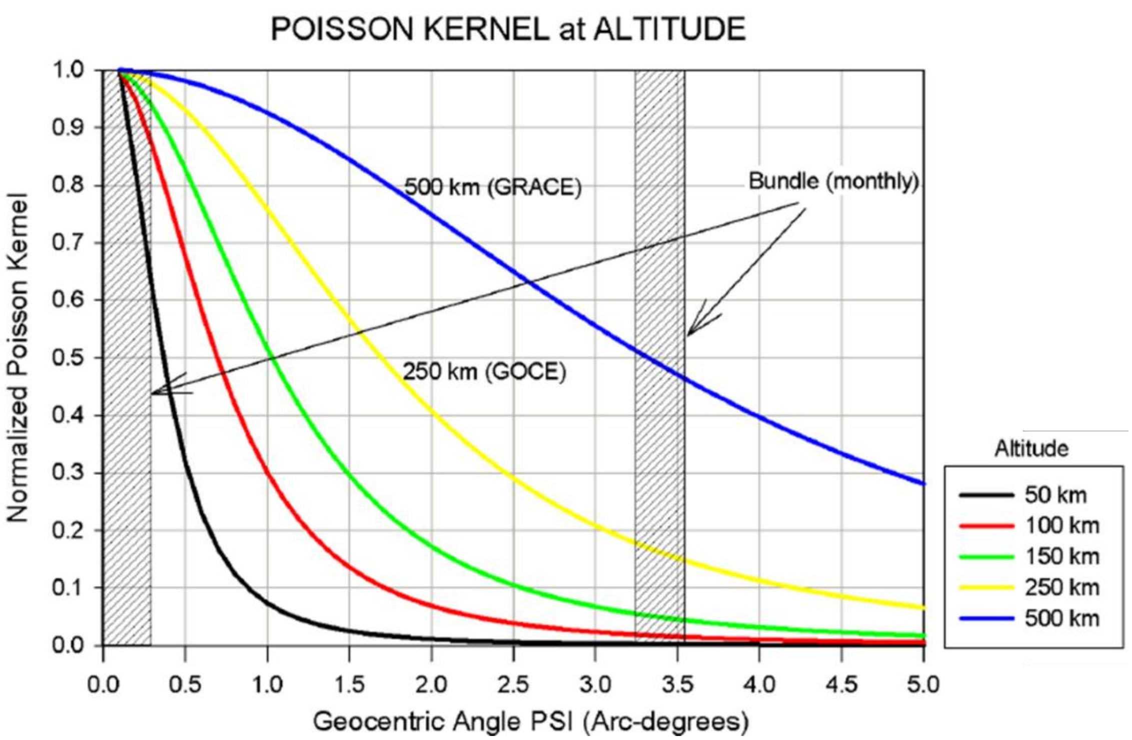

Figure 5.17: Simulations of GRACE sensitivity to the gravitational signal of each bundle using Poisson Kernel and upward continuation (normalized). Each colour represents simulations at a different altitude. The grey shaded areas denote two consecutive ascending (or descending) bundles formed by GRACE ground tracks over a month.

5.5.4 Number of the modulating envelopes

As discussed in Section 5.5.2, sub-Nyquist artifacts fall on different modulating envelopes. The number of modulating envelopes comes from the reducing ratio $\frac{m}{n}$, where n is the number of interlaced modulating envelopes and m is integer, such that $m < n$ (Amidror, 2015; Theorem 5.1), and in our case (sub-Nyquist artifacts), $2m < n$ (Patorski et al., 2011). From the analyses presented in Figure 5.16, the interlaced envelopes $n = 15$ correspond to the number of the distinct structure noted, whereas integer $m = 7$ corresponds to the stripes within each structure that indeed satisfy $2m < n$. Note that the number of interlaced modulating envelopes ($n = 15$) equals the number of tracks per day (15) and the integer m equals the number of days needed to cluster a ground track into the same bundle. The ratio $\frac{m}{n} = \frac{7}{15}$ is at the 'border' of the sampling theorem that leads to *borderline sub-Nyquist artifacts* (Amidror, 2015). We note that ratio $\frac{m}{n}$ can only range in the interval $\frac{1}{20} < \frac{m}{n} < \frac{1}{2}$ (Williams, 2000).

5.5.5 A very low frequency gravitational signal

The final part to complete Equation (5.10) is to identify a very low frequency signal that GRACE oversamples. From the spectral analysis of the sampled gravitational signal (see Figure 5.16), we already suspect that the latitudinal structure of the disturbing potential (geoid) might be the low frequency gravitational signal we are looking for. So far, the latitudinal sampling frequency of GRACE and the number of modulating envelopes are defined, and we already know the beat frequency (stripe beat frequency) f. Therefore, we can calculate the frequency of the "unknown" gravitational signal directly for each parallel of latitude that modulates the sampled signal. Initially, the frequency of stripes ($f \approx \frac{96}{360} \approx 0.27\ c/\ell$) equals the phase difference between the highly oscillating waves $\frac{m}{n\varepsilon} = \frac{7}{15\varepsilon}$. Solving for ε, the low frequency of the modulating envelope is derived as $\varepsilon = f_{env} = \frac{m}{nf} = 1.72\ c/\ell$. We note that the wavelength of stripes demonstrates slight variations along various latitudes and therefore it is expected that the f_{env} will vary within a narrow interval. Our initial hypothesis postulates that the low frequency gravitational signal oversampled by GRACE is the geoid. To test this hypothesis, we derive latitudinal profiles of the geoid using GO_CONS_GCF_2_TIM_R5 (Brockmann et al., 2014) model and estimate the least squares spectrum of each profile. The dominant frequency of the geoid latitudinal profiles ranges within the interval [1.5, 3.1] c/ℓ, which is in agreement with our previous calculation i.e., $\varepsilon = f_{env} = \frac{m}{nf} = 1.72\ c/\ell$, validating that geoid is indeed the very low frequency signal that GRACE samples in the critical neighbourhood $\frac{m}{n} f_s$.

5.6 Synthetic Stripes

We are now in the position to simulate sub-Nyquist artifacts. To achieve this, the steps (a)-(c) are followed:

a) We derive latitudinal profiles of GO_CONS_GCF_2_TIM_R5 geoid every 0.5° degrees with a sampling interval of 0.5°.

b) We estimate the statistically significant and dominant frequency $f_{env} = \varepsilon$ using least-squares spectral analysis of each latitudinal profile. As noted previously, this frequency ranges in [1.5, 3.1] c/ℓ for the different profiles.

c) We reconstruct the sub-Nyquist artifact along each latitudinal profile and we use $\frac{m}{n} = \frac{7}{15}$, the initial sampling frequency $f_s = \frac{360}{3.43} \approx 105\ c/\ell$ and the geoid frequency $\varepsilon = f_{env}$ corresponding to the geoid latitudinal profile. We now proceed with the reconstruction of the sub-Nyquist artifacts along the latitudes that are given as amplitude modulated signals employing Equation (5.7) (Amidror, 2015).

Subsequently, we sweep through a number of sampling frequencies around $f_s = 105\ c/\ell$ namely, $2f_s$, $3f_s$, and so on, keeping the rest of the parameters in Equation (5.7) constant. These various values of the sampling frequency affect the number of stripes produced. The latitudinal sampling frequency is found to be $3f_s = 315\ c/\ell$ or equivalently the sampling interval $\Delta_s = \frac{3.43^0}{3} = 1.14^{\circ}$ produces 96 stripes, which are equal to the number of stripes we find in RL04 models. Note that these 96 stripes are created using the $105\ c/\ell$ initial sampling frequency. Notably, $\Delta_s = 1.14^{\circ}$ is the effective sampling interval of GRACE along the lines of latitude representing the unequal and interlaced sampling. The effective sampling interval defines the resolution of GRACE at half-wavelength. Note that frequencies below $f_s = 105\ c/\ell$ and above $3f_s$ do not produce meaningful stripes or produce no stripes at all.

The artifacts we generated are synthetic and thus unitless. However, we note that the stripes shown in Figure 5.18 are of variable amplitude in a nearly latitudinal direction. This behaviour is attributed to the variable latitudinal spectral characteristics of the geoid, albeit within a relatively narrow spectral band, namely [1.5, 3.1] c/ℓ. Quantifying the magnitude of stripes is a rather challenging task, as it depends on a variety of factors, such as the latitudinal variability of the geoid (amplitude, frequency), the mission's orbital resonance, the intensity of the magnetic storms, and others. The peak frequency of the synthetic stripes was estimated by means of least-squares spectral analysis; results demonstrate a peak frequency at 96 c/ℓ, which agrees very well with the spectral characteristics of the real stripes (we count 96 stripes across the globe). Of note is that the number of stripes is very close to the resonant orders (Dahle et al., 2014; Seo et al., 2008). Overall, our analyses indicates that the stripes are induced by the GRACE sampling characteristics, where the latitudinal spatial sampling interval is of critical nature (close to $\Delta_s = 1.14^{\circ}$) and the ground track bundles oversample the geoid, leading to sub-Nyquist artifacts.

Since the aim of this study was to reveal the mechanism that generates the stripes and not to introduce yet another type of filtering, we do not proceed with their elimination by means of tuning the magnitude of the synthetic stripes. Rather now that the origin of the artifact is revealed, we target a rigorous solution. Synthetic stripes calculated every month, can be used to identify specific regions in the world that are more affected by the stripes. Therefore, depending on the geophysical application, different strategies to decipher stripes from geophysical signal can be locally adopted.

Overall, the following strategies to eliminate at source the stripes on GRACE models using sampling and moiré theories are suggested:

1) *remove the low-degree (up to C_{33}) latitudinal structure of the geoid at Level 1B data before developing the new models*
2) *break of latitudinal sampling pattern by randomly selecting orbits (applicable for long-term solutions) or design different spatial sampling frequencies (different orbits) for future (follow-on) missions*
3) *demodulation of the amplitude modulated sampled signal on existing models; this may be rather challenging. Examples of classical demodulation processes can be found in Fagot and Magne (2013) and Ruppert et al. (2017).*

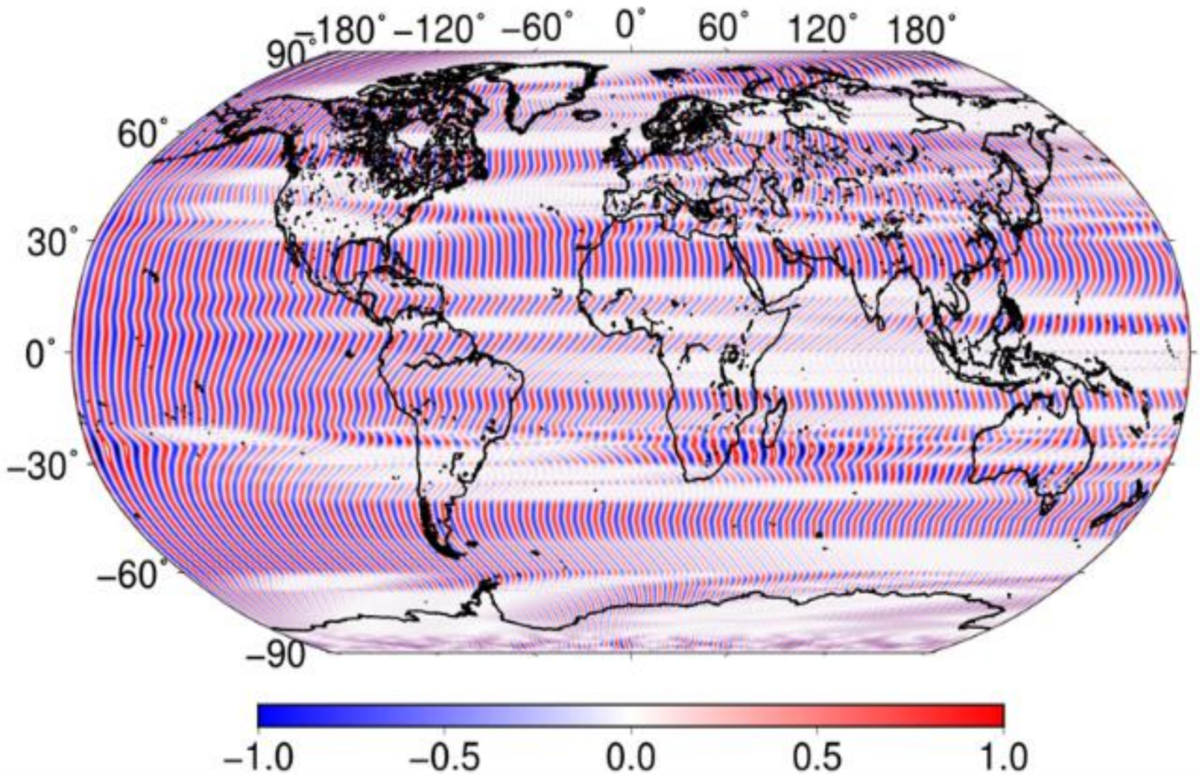

Figure 5.18: Synthetic stripes created using sub-Nyquist moiré theory and GRACE sampling characteristics. Note that these are synthetic stripes and therefore unitless.

From the perspective of celestial mechanics, the part of the Earth's disturbing potential that expresses the deviation of the Earth's gravity potential (geopotential) from a 'perfect' (ellipsoidal) normal field, is in fact the source of a disturbing gravitational force that affects the motion of a satellite. This disturbing potential, if known, can be implemented as a force model in the equations of motion of the satellite, whose form is well known (e.g., Bettadpur and McCullough, 2017; Kaula, 1966):

$$\ddot{\boldsymbol{r}} = -\frac{\mu}{r^2}\boldsymbol{e}_r + \boldsymbol{f}_p(\boldsymbol{r}, \dot{\boldsymbol{r}}, \alpha), \tag{5.12}$$

where the first term in the RHS is the central field and the second term represents the perturbations of the central field; $\boldsymbol{r}$ is the position vector of the satellite (usually in the orbital coordinate system – includes the 6 Keplerian elements); μ is the gravitational parameter (constant) of the central body and α are the parameters of the force model (gravitational or other). The critical parameters in the equations of motion are the force model parameters α, which must be known to be able to double integrate the equations of motion in space-time (subject to initial conditions on the position and velocity of the satellite at some instant of time t_0) to obtain the position of the satellite correctly. If a force model is not known and neglected, its effects will plague the final model. In the case of GRACE stripes, α must contain the latitudinal variability of the disturbing potential, dominated by at least the sectorial component of the disturbing potential of d/o 2 (C_{22}) is a-priori included) to avoid the creation of sub-Nyquist artifacts. This approach might eliminate the stripes at the source altogether.

Of note is that for other monthly solutions, GRACE repeat orbits might be different than the 7-days found for the monthly solutions analyzed herein. This behaviour does not change the theory and consequently the formulation used to create synthetic stripes. The only change refers to the integer *m*, that should reflect the actual number of days for repeat orbits (i.e., the number of days of repeat orbits (herein 7), should be replaced accordingly).

Note that for the current available releases of GRACE models (RL01-RL06) the end user could not apply any of the recommendations made here, as they all apply to data processing at earlier stages (processing of Level 1A and 1B data) or to the design of different orbits that will avoid the critical $3f_s$ sampling frequency.

5.7 Summary

In this chapter, the origin for the presence of stripes artifact in GRACE-based models has been investigated. Results of this analysis constitute one of the original contributions of this research and suggest that GRACE sampling characteristics drive stripes in the sampled signal. Specific strategies to eliminate stripes in the first place are suggested.

6

Conclusions and Recommendations for future work

In this Chapter, the main conclusions drawn by this research and recommendations for future work are discussed.

6.1 Conclusions

With GRACE-FO mission just releasing the first stream of data, and new concepts for the next generation gravity missions being contemplated, the expectations for extracting the utmost information about the Earth's gravity field have been raised. The focus of this study has been on improving the performance of GRACE mission products, which is achieved by assessing the three main research objectives as described in Chapters 3,4 and 5.

Each of the objectives led to an original contribution. We briefly draw the main conclusions that were analyzed in each chapter and discuss the impact they have on the research in satellite gravimetry.

In Chapter 3 the response of GRACE on-board instrumentation to geomagnetic storms was investigated. This analysis showed that:

1) Disturbances shown on GRACE measurements are correlated with the dynamics as measured by the ACE mission and derived from Poynting flux estimates.

2) GRACE accelerometers mounted at the centre of mass of the spacecraft may not only be affected by kinetic energy exchange between neutral winds and the spacecraft, but also from plasma exchange between the electromagnetic input and the accelerometers electrostatic structure. The concept of differential mode was shown to be useful to assess the source of perturbation. Further analysis on the impact of these leakages on the final solution is required.

Impact: Understanding how GRACE instrumentation is affected by dynamics occurring on the spacecraft environment can lead to modeling/removal of the instrumentation disturbances, which will improve the performance of the final solutions. Additionally, should the origin of the disturbances be known (i.e., uncharged and charged particles) a reverse analysis can be applied to extract information for the geomagnetic storms using the disturbances of GRACE instrumentation.

Chapter 4 advanced the idea of differential mode to a new innovative method called GRACE gradiometer mode (GRACE-GM), that allows for the estimation of gravitational gradients using GRACE mission measurements. It was shown that:

1) GRACE-GM can be used to derive the full GGT, employing only Level 1B data. These gradients agree well with GOCE's gradients. Coherence analysis between GOCE and GRACE-GM gradients reached nearly 80% in certain cases.

2) GRACE-GM is highly sensitive in signals induced by the Earth's magnetic field. In particular, we showed that DM accelerations from GOCE and GRACE-GM demonstrated a strong similarity in their structure, particularly exposing the very strong magnetic inclination signal.

3) GRACE-GM gradients depict multi-spectral gravitational gradients allowing for sensing geophysical signals of various wavelengths.

4) GRACE-GM gradients suffer from high noise and magnetic-field related leakages. The noise floor of the trace was estimated to be 48mE.

Impact: The idea of GRACE-GM can be used as a proof-of-concept idea for future satellite gravity missions. GRACE-GM gradients provide stripe-free solutions and capture geophysical signals in a wide waveband. Additionally, the core idea of GRACE-GM, that is "bringing the two spacecraft as close as possible" can be used in cases of instrumentation failure.

Chapter 5 revealed for the first time since GRACE launch in 2002, the origin of the very disturbing and systematic artifact of stripes on GRACE gravity field models. It was shown that:

1) There are two different types of artifacts that follow a "stripy" pattern on GRACE models. The *aliasing* artifacts that show as *striations* (they fold-over the lower frequencies of the sampled gravitational field); and the sub-Nyquist artifacts that show as *stripes* (they show in the higher frequencies of the sampled gravitational field). In this study we investigated the *stripes* artifact.
2) Spatiotemporal and spectral characteristics of the stripes display nearly identical frequencies along a latitudinal profile for all the 36 solutions employed in this study. Additionally, the stripes drift from month to month.
3) GRACE ground tracks resemble a travelling wave. Interference fringes derived using the ground tracks as provided in GNV1B files appear to be highly correlated with the stripes shown in the sampled signal.
4) Stripes are an artifact driven by GRACE sampling characteristics. Our analysis suggests that the stripes are sub-Nyquist (or pseudo-moiré) artifacts, produced by GRACE latitudinal spatial sampling frequency of ground track bundles, that sample a very low frequency gravitational signal, namely the geoid.
5) GRACE effective latitudinal sampling frequency is equal to $\Delta_s = 1.14^{\circ}$.

Impact: Stripes deteriorate significantly the performance of the gravity field maps derived from GRACE measurements. They conceal signals shorter than approximately 200 km and their magnitude may reach several cm in the geoid. This study investigated and explained the mechanism that drives stripes in GRACE models. Based on the analysis conducted, certain techniques for removal of the stripes artifact in the first place have been suggested. Should these recommendations be implemented and lead to stripe-free models, the upcoming releases of GRACE models would not suffer from stripes, leading to higher performance gravity field models (e.g., shorter scale signals could be resolved) and better understanding of mass transport phenomena.

6.2 Recommendations for future work

Analysis on the response of GRACE on-board instrumentation in intense space weather conditions (i.e., geomagnetic storms), suggests that further investigation of the impact of the spacecraft environment on the satellite is required. Swarm mission (launched in 2013), might be proven an excellent source of information to enlighten perturbations on GRACE-FO mission driven by space weather dynamics. The correlation between GRACE perturbations with measurements and geomagnetic anomalies derived from Swarm Level 1B and Level 2 data, will help establish the initial hypothesis for their relationship, advancing our understanding on how LEO missions are affected by the Earth's static and dynamic magnetic field.

GRACE-GM, as presented in this study, is a proof-of-concept methodology, whose further enhancement will contribute toward designing a single space mission that will allow for both high-accuracy estimates of the gravitational field's temporal and stationary parts. Projecting this concept into the future, we can in fact further venture with only one space mission consisting of an enhanced GRACE-like configuration or multispacecraft constellation that will capture both the Earth's static and time-varying gravity field. This enhanced and perhaps multipurpose mission should include more accurate POD, precise accelerometers, and an enhanced attitude determination system. The same principle applies to the Earth's magnetic field when future Swarm-like missions could result in a more accurate mapping of the Earth's static and time-varying magnetic field.

An improved GRACE-GM methodology could be a fully independent operational technique should the following three constraints be overcome:

1. Instead of using the accelerometer and start camera measurements, GRACE-GM could estimate the full GGT using the gravitational accelerations recovered from the POD solutions of each spacecraft.
2. The distance between the two spacecraft is considerably longer than the mean distance in certain geographical areas. Such distances violate assumption (a) and may limit the homogeneity and resolution of the gradients. Improvements on the accelerometer sampling frequency, that is, providing GRACE-FO Level 1B measurements at 10 Hz or higher, rather

than interpolating the 1 Hz data, would result in capturing acceleration measurements at shorter intersatellite distances and consequently in better estimates of GGT.

3. More accurate dynamic orbits would allow for better estimates of the distance between the two spacecraft. Studies on the error budget of distances and their spatial distribution would improve the accuracy of GRACE-GM. GRACE-FO laser-based ranging system would also be considered as a constraining parameter that will increase the intersatellite 3-D distance accuracy derived from POD.
4. Better modeling of the magnetic inclination signal that disturbs differential accelerations and leaks into the gravitational gradients.

Finally, this research achieved to unravel the mechanism that drives stripes on GRACE models for the first time. GRACE sampling characteristics have been shown to be responsible for the dominant artifact on GRACE models. To be able to create stripe-free solutions we suggest to a) demodulate the sampled signal; b) remove the latitudinal structure of the geoid before processing the new models and c) change of latitudinal sampling pattern (moiré pattern) by randomly selecting different orbits for future (follow-on) missions. The latter solution is applicable only for long-term solutions. Perceiving the artifact of stripes from the celestial mechanics approach we identified the origin of stripes on the lack of knowledge of the geoid (force models). We recommend that further investigations of the latitudinal variability of the geoid should take place, to allow for the generation of stripe-free gravity field models dominated by at least the sectorial component of the low frequency (C_{33}) geoid.

7

References

Amidror, I., 2009. The Theory of the Moiré Phenomenon. Springer, London.

Amidror, I., 2013. Mastering the discrete Fourier transform in one, two or several dimensions: pitfalls and artifacts (Vol. **43**). Springer Science and Business Media.

Amidror, I., 2015. Sub-Nyquist artefacts and sampling moiré effects, *R. Soc. open sci.* 2: 140550. http://dx.doi.org/10.1098/rsos.140550.

Amm, O., 1997. Ionospheric elementary current systems in spherical coordinates and their application. *Journal of geomagnetism and geoelectricity*, **49**(7), pp.947-955.

Amm, O. and Viljanen, A., 1999. Ionospheric disturbance magnetic field continuation from the ground to the ionosphere using spherical elementary current systems. *Earth, Planets and Space*, **51**(6), pp.431-440.

Amm, O., Engebretson, M.J., Hughes, T., Newitt, L., Viljanen, A. and Watermann, J., 2002. A traveling convection vortex event study: Instantaneous ionospheric equivalent currents, estimation of field-aligned currents, and the role of induced currents. *Journal of Geophysical Research: Space Physics*, **107**(A11), pp.SIA-1.

Anderson, B.J., Olson, C.N., Korth, H., Barnes, R.J., Waters, C.L. and Vines, S.K., 2018. Temporal and spatial development of global Birkeland currents. *Journal of Geophysical Research: Space Physics*, **123**(6), pp.4785-4808.

Bandikova, T., 2016. The role of attitude determination for inter-satellite ranging. Doctoral dissertation. Retrieved from Deutsche Geodätische Kommission (https://dgk.badw.de/fileadmin/user_upload/Files/DGK/docs/c-758.pdf).

Bandikova, T., McCullough, C., *and* Kruizinga, G.L., 2017. GRACE Accelerometer data transplant. *AGU Fall meeting, G31B-0903.*

Bandikova, T., McCullough, C., Kruizinga, G. L., Save, H., *and* Christophe, B., 2019. GRACE Accelerometer data transplant. *Advances in Space Research,* **64***(*3*),* 623–644.

Bandikova, T. and Flury, J., 2014. Improvement of the GRACE star camera data based on the revision of the combination method. *Advances in Space Research*, **54**(9), 1818-1827.

Belda, S., García-García, D. and Ferrándiz, J.M., 2015. On the decorrelation filtering of RL05 GRACE data for global applications. *Geophysical Journal International*, **200**(1), pp.173-184.

Bettadpur, S. and McCullough, C., 2017. The classical variational approach. *In Global Gravity Field Modeling from Satellite-to-Satellite Tracking Data* (pp. 81-95). Springer, Cham.

Bettadpur, S., 2007. CSR level-2 processing standards document for product release 04, GRACE 327-742, The GRACE Project. Center for Space Research, University of Texas at Austin.

Bock, R., Lühr, H. and Grunwaldt, L., 2000. Champ scientific payload and its contribution to a stable attitude control system. In *AGU Fall Meeting*.

Bosch, W., 2005. Using the EIGEN-GRACE02S gravity field to investigate defectiveness of marine gravity data. In *Gravity, Geoid and Space Missions* (pp. 89-94). Springer, Berlin, Heidelberg.

Bouman, J., Ebbing, J., Meekes, S., Fattah, R. A., Fuchs, M., Gradmann, S., Haagmans, R., Lieb, V., Schmidt, M., Dettmering, D., and Bosch, W. 2015. GOCE gravity gradient data for lithospheric modeling. *International Journal of Applied Earth Observation and Geoinformation*, **35**, 16-30.

Bouman, J., Fiorot, S., Fuchs, M., Gruber, T., Schrama, E., Tscherning, C., Veicherts, M., and Visser, P., 2011. GOCE gravitational gradients along the orbit. *Journal of Geodesy*, **85**(11), 791.

Bracewell, R.N., 1978. The Fourier Transform and Its Applications. McGraw-Hill Publishing Company, Reading, New York.

Bracewell, R.N., 1995. Two-dimensional imaging. Prentice Hall, New Jersey.

Brockmann, J.M., Zehentner, N., Höck, E., Pail, R., Loth, I., Mayer-Gürr, T. and Schuh, W.D., 2014. EGM_TIM_RL05: an independent geoid with centimeter accuracy purely based on the GOCE mission. *Geophysical Research Letters*, **41**(22), pp.8089-8099.

Bruinsma, S., Forbes, J.M., Nerem, R.S. and Zhang, X., 2006. Thermosphere density response to the 20–21 November 2003 solar and geomagnetic storm from CHAMP and GRACE accelerometer data. *Journal of Geophysical Research: Space Physics*, **111**(A6).

Bruinsma, S.L. and Forbes, J.M., 2010. Anomalous behaviour of the thermosphere during solar minimum observed by CHAMP and GRACE. *Journal of Geophysical Research: Space Physics*, **115**(A11).

Bruinsma, S.L., Förste, C., Abrikosov, O., Lemoine, J.M., Marty, J.C., Mulet, S., Rio, M.H. and Bonvalot, S., 2014. ESA's satellite-only gravity field model via the direct approach based on all GOCE data. *Geophysical research letters*, **41**(21), pp.7508-7514.

Cade III, W.B. and Chan-Park, C., 2015. The origin of “Space Weather”. *Space Weather*, **13**(2), pp.99-103.

Canuto, C., Hussaini, M.Y., Quarteroni, A. and Zang, T.A., 2006. Spectral methods. Springer-Verlag, Berlin.

Case, K., Kruizinga, G. and Wu, S., 2010. GRACE Level 1B data product user handbook. JPL Publication D-22027.

Casotto, S., and Fantino, E., 2007. Evaluation of methods for spherical harmonic synthesis of the gravitational potential and its gradients. *Advances in Space Research*, **40**(1), pp.69-75.

Cesare, S., Allasio, A., Anselmi, A., Dionisio, S., Mottini, S., Parisch, M., Massotti, L. and Silvestrin, P., 2016. The European way to gravimetry: From GOCE to NGGM. *Advances in Space Research*, **57**(4), pp.1047-1064.

Chambers, D.P., Wahr, J. and Nerem, R.S., 2004. Preliminary observations of global ocean mass variations with GRACE. *Geophysical Research Letters*, **31**(13).

Chen, J.L., Rodell, M., Wilson, C.R. and Famiglietti, J.S., 2005. Low degree spherical harmonic influences on Gravity Recovery and Climate Experiment (GRACE) water storage estimates. *Geophysical Research Letters*, **32**(14).

Chen, J., Li, J., Zhang, Z., and Ni, S., 2014. Long-term groundwater variations in Northwest India from satellite gravity measurements. *Global and Planetary Change*, **116**, pp.130-138.

Cruz, J.Y and Laskowski., P., 1984. Upward continuation of surface gravity Anomalies. Report No 360. The Ohio State Univeristy, Department of Geodetic Science and Surveying, Columbus, Ohio, USA.

Dahle, C., Flechtner, F., Gruber, C., König, D., König, R., Michalak, G. and Neumayer, K.H., 2014. GFZ RL05: an improved time-series of monthly GRACE gravity field solutions. In *Observation of the System Earth from Space-CHAMP, GRACE, GOCE and future missions* (pp. 29-39). Springer, Berlin, Heidelberg.

Dahle, C., Flechtner, F., Gruber, C., König, D., König, R., Michalak, G. and Neumayer, K.H., 2013. GFZ GRACE level-2 processing standards document for level-2 product release 0005: revised edition. GeoForschungsZentrum, Potsdam.

Darbeheshti, N., Wöske, F., Weigelt, M., Mccullough, C. and Wu, H., 2018. GRACETOOLS—GRACE Gravity Field Recovery Tools. Geosciences, **8**(9), p.350.

Davis, J.L., Tamisiea, M.E., Elósegui, P., Mitrovica, J.X. and Hill, E.M., 2008. A statistical filtering approach for Gravity Recovery and Climate Experiment (GRACE) gravity data. *Journal of Geophysical Research: Solid Earth*, **113**(B4).

Dobslaw, H., Flechtner, F., Bergmann-Wolf, I., Dahle, C., Dill, R., Esselborn, S., Sasgen, I. and Thomas, M., 2013. Simulating high-frequency atmosphere-ocean mass variability for dealiasing of satellite gravity observations: AOD1B RL05. *Journal of Geophysical Research: Oceans*, **118**(7), pp.3704-3711.

Doornbos, E. and Klinkrad, H., 2006. Modelling of space weather effects on satellite drag. *Advances in Space Research*, **37**(6), pp.1229-1239.

Doornbos, E., Klinkrad, H. and Visser, P., 2008. Use of two-line element data for thermosphere neutral density model calibration. *Advances in Space Research*, **41**(7), pp.1115-1122.

Dos Santos, P.A.M., 2002. Moiré-like patterns as a spatial beat frequency in photorefractive sinusoidal phase gratings superposition. *Optics communications*, **212**(4-6), pp.211-216.

Drucker, H., Burges, C.J., Kaufman, L., Smola, A.J. and Vapnik, V., 1997. Support vector regression machines. In *Advances in neural information processing systems*, pp. 155-161.

Duan, X.J., Guo, J.Y., Shum, C.K. and Van Der Wal, W., 2009. On the postprocessing removal of correlated errors in GRACE temporal gravity field solutions. *Journal of Geodesy*, **83**(11), p.1095.

Dunn, C., Bertiger, W., Bar-Sever, Y., Desai, S., Haines, B., Kuang, D., Franklin, G., Harris, I., Kruizinga, G., Meehan, T. and Nandi, S., 2003. Instrument of GRACE: GPS augments gravity measurements.

ESA, S. Reports for Mission Selection.,1999. The four candidate Earth Explorer Core Missions. Gravity Field and Steady-State Ocean Circulation Mission.

ESA, 2006. S. Goce l1b products user handbook. Tech. rep.

Fagot, J. and Magne, P., 2013. *Frequency modulation theory: Application to microwave links* (Vol. 11). Elsevier.

Farless, D.L., 1985, August. The application of periodic orbits to TOPEX mission design. In: Kaufman B et al (eds)‘‘Astrodynamics’’, 58, Part I, Adv Astron Sci Am Astronaut Soc, San Diego, pp 13–36.

Fengler, M. J., Freeden, W., Kohlhaas, A., Michel, V., *and* Peters, T., 2007. Wavelet modeling of regional and temporal variations of the Earth's gravitational potential observed by GRACE. *Journal of Geodesy*, **81**(1), 5–15.

Flechtner, F., Dahle, C., Neumayer, K.H., König, R. and Förste, C., 2010. The release 04 CHAMP and GRACE EIGEN gravity field models. In *System Earth via geodetic-geophysical space techniques* (pp. 41-58). Springer, Berlin, Heidelberg.

Flechtner, F., Neumayer, K.H., Dahle, C., Dobslaw, H., Fagiolini, E., Raimondo, J.C., and Güntner, A., 2016. What can be expected from the GRACE-FO laser ranging interferometer for Earth science applications?. *Remote Sensing and Water Resources*, pp. 263-280.

Flury, J., Bettadpur, S. and Tapley, B.D., 2008. Precise accelerometry on-board the GRACE gravity field satellite mission. *Advances in Space Research*, **42**(8), pp.1414-1423.

Friis-Christensen, E., Finlay, C. C., Hesse, M., and Laundal, K. M., 2017. Magnetic field perturbations from currents in the dark polar regions during quiet geomagnetic conditions. *Space Science Reviews*, **206**(1-4), 281-297.

Frommknecht, B., 2007. Integrated sensor analysis of the GRACE mission (Doctoral dissertation). Retrieved from Technische Universität München (https://mediatum.ub.tum.de/doc/630607/file.pdf).

Frommknecht, B., Oberndorfer, H., Flechtner, F. and Schmidt, R., 2003. Integrated sensor analysis for GRACE? development and validation. *Advances in Geosciences*, **1**, pp.57-63.

Fuchs, M. J., Bouman, J., Broerse, T., Visser, P., and Vermeersen, B., 2013. Observing coseismic gravity change from the Japan Tohoku-Oki 2011 earthquake with GOCE gravity gradiometry. *Journal of Geophysical Research: Solid Earth*, **118**(10), 5712-5721.

Gerlach, O.H., 1965. Attitude stabilization and control of earth satellites. *Space Science Reviews*, **4**(4), pp.541-582.

Ghaderpour, E. and Pagiatakis, S.D., 2017. Least-squares wavelet analysis of unequally spaced and non-stationary time series and its applications. *Math. Geo*, **49**(7), pp.819-844.

Ghaderpour, E., Ince, E.S. and Pagiatakis, S.D., 2018. Least-squares cross-wavelet analysis and its applications in geophysical time series. *Journal of Geodesy*, pp.1-14.

Glass, L., 1969. Moire effect from random dots. *Nature*, **223**(5206), p.578.

Gonzalez, W.D., Joselyn, J.A., Kamide, Y., Kroehl, H.W., Rostoker, G., Tsurutani, B.T. and Vasyliunas, V.M., 1994. What is a geomagnetic storm?. *Journal of Geophysical Research: Space Physics*, **99**(A4), pp.5771-5792.

Gooding, R.H., Wagner, C.A., Klokočník, J., Kostelecký, J. and Gruber, C., 2007. CHAMP and GRACE resonances, and the gravity field of the Earth. *Advances in Space Research*, **39**(10), pp.1604-1611.

Han, S.C., Jekeli, C. and Shum, C.K., 2004. Time-variable aliasing effects of ocean tides, atmosphere, and continental water mass on monthly mean GRACE gravity field. *Journal of Geophysical Research: Solid Earth*, **109**(B4).

Han, S.C., Shum, C.K., Jekeli, C., Kuo, C.Y., Wilson, C. and Seo, K.W., 2005. Non-isotropic filtering of GRACE temporal gravity for geophysical signal enhancement. *Geophysical Journal International*, **163**(1), pp.18-25.

Hapgood, M.A., 1992. Space physics coordinate transformations: A user guide. Planetary and Space Science, **40**(5), pp.711-717.

Hauk, M. and Pail, R., 2019. Gravity Field Recovery Using High-Precision, High–Low Inter-Satellite Links. *Remote Sensing*, **11**(5), p.537.

Hecht, E., 1998. *Optics*. Third ed., Reading, MA: Addison-Wesley, 1998. - 694 p.

Heiskanen, W.A and H. Moritz, 1967. Physical Geodesy. W.H. Freeman and Co., San fransisco.

Herman, J., Presti, D., Codazzi, A., and Belle, C. Attitude Control for GRACE: The First Low-Flying Satellite Formation. *18th International Symposium on Space Flight Dynamics*, Munich, Germany, Vol. **548**, p.27.

Hetényi, G., Cattin, R., Berthet, T., Le Moigne, N., Chophel, J., Lechmann, S., Hammer, P., Drukpa, D., Sapkota, S.N., Gautier, S. and Thinley, K., 2016. Segmentation of the Himalayas as revealed by arc-parallel gravity anomalies. *Scientific reports*, **6**, 33866.

Hofmann-Wellenhof, B. and Moritz, H., 2006. *Physical geodesy*. Springer Science and Business Media.

Ince, E.S., 2016. GOCE gradiometer measurement disturbances and their modelling by means of ionospheric dynamics, (Doctoral dissertation). Retrieved from YorkSpace (*http://hdl.handle.net/10315/33646*). York University.

Ince, E. S., and Pagiatakis, S. D., 2016. Effects of space weather on GOCE electrostatic gravity gradiometer measurements. *Journal of Geodesy*, **90**(12), 1389-1403.

Ince, E.S. and Pagiatakis, S.D., 2017. GOCE gradiometer measurements response to ionospheric dynamics. *Journal of Geophysical Research: Space Physics*, ***122***(10), pp.10-712.

Ivins, E.R., James, T.S., Wahr, J., O. Schrama, E.J., Landerer, F.W. and Simon, K.M., 2013. Antarctic contribution to sea level rise observed by GRACE with improved GIA correction. *Journal of Geophysical Research: Solid Earth*, **118**(6), pp.3126-3141.

Ivins, E.R., Watkins, M.M., Yuan, D.N., Dietrich, R., Casassa, G. and Rülke, A., 2011. On-land ice loss and glacial isostatic adjustment at the Drake Passage: 2003–2009. *Journal of Geophysical Research: Solid Earth*, **116**(B2).

Janssen, V., 2009. Understanding Coordinate Systems, Datums and Transformations in Australia. In: Ostendorf, B., Baldock, P., Bruce, D., Burdett, M. and P. Corcoran (eds.), Proceedings of the

Surveying and Spatial Sciences Institute Biennial International Conference, Adelaide 2009, Surveying and Spatial Sciences Institute, pp. 697-715.ISBN: 978-0-9581366-8-6.

Kang, Z., Nagel, P. and Pastor, R., 2003. Precise orbit determination for GRACE. *Advances in Space Research*, **31**(8), pp.1875-1881.

Kang, Z., Tapley, B., Bettadpur, S., Ries, J. and Nagel, P., 2006. Precise orbit determination for GRACE using accelerometer data. *Advances in Space Research*, **38**(9), pp.2131-2136.

Kaula, W.M., 1966. Theory of satellite geodesy. Applications of satellites to geodesy. Waltham, Mass: Blaisdell.

Keller, W. and Sharifi, M.A., 2005. Satellite gradiometry using a satellite pair. *Journal of Geodesy*, **78**(9), pp.544-557.

Kelley, M.C., 2009. *The Earth's ionosphere: plasma physics and electrodynamics* (Vol. **96**). Academic press.

Kim, J., 2000. *Simulation study of a low-low satellite-to-satellite tracking mission* (Doctoral dissertation, University of Texas at Austin).

Kim, J. and Lee, S.W., 2009. Flight performance analysis of GRACE K-band ranging instrument with simulation data. *Acta Astronautica*, **65**(11-12), pp.1571-1581.

Klees, R., Revtova, E.A., Gunter, B.C., Ditmar, P., Oudman, E., Winsemius, H.C. and Savenije, H.H.G., 2008. The design of an optimal filter for monthly GRACE gravity models. *Geophysical Journal International*, **175**(2), pp.417-432.

Klinger, B. and Mayer-Gürr, T., 2016. The role of accelerometer data calibration within GRACE gravity field recovery: Results from ITSG-Grace2016. *Advances in space research*, **58**(9), pp.1597-1609.

Klokočník, J., Gooding, R.H., Wagner, C.A., Kostelecký, J. and Bezděk, A., 2013. The use of resonant orbits in satellite geodesy: a review. *Surveys in Geophysics*, **34**(1), pp.43-72.

Klokočník, J., Wagner, C.A., Kostelecký, J., Bezděk, A., Novák, P. and McAdoo, D., 2008. Variations in the accuracy of gravity recovery due to ground track variability: GRACE, CHAMP, and GOCE. *Journal of Geodesy*, **82**(12), pp.917-927.

Knudsen, P., Bingham, R., Andersen, O., and Rio, M. H., 2011. A global mean dynamic topography and ocean circulation estimation using a preliminary GOCE gravity model. *Journal of Geodesy*, **85**(11), 861-879.

Kroes, R., Montenbruck, O., Bertiger, W. and Visser, P., 2005. Precise GRACE baseline determination using GPS. *GPS Solutions*, **9**(1), pp.21-31.

Kusche, J., 2007. Approximate decorrelation and non-isotropic smoothing of time-variable GRACE-type gravity field models. *Journal of Geodesy*, **81**(11), pp.733-749.

Kusche, J., Schmidt, R., Petrovic, S. and Rietbroek, R., 2009. Decorrelated GRACE time-variable gravity solutions by GFZ, and their validation using a hydrological model. *Journal of geodesy*, **83**(10), pp.903-913.

Liu, X., Thayer, J.P., Burns, A., Wang, W. and Sutton, E., 2014. Altitude variations in the thermosphere mass density response to geomagnetic activity during the recent solar minimum. *Journal of Geophysical Research: Space Physics*, **119**(3), pp.2160-2177.

Mallat, S., 1999. A wavelet tour of signal processing. Academic Press, New York.

Matsuo, K. and Heki, K., 2011. Coseismic gravity changes of the 2011 Tohoku-Oki earthquake from satellite gravimetry. *Geophysical Research Letters*, **38**(7).

McCarthy, D. (ed.), 1996. IERS Conventions (1996), International Earth Rotation Service Technical Note 21, Observatoire de Paris.

Milne, G.A., Mitrovica, J.X. and Davis, J.L., 1999. Near-field hydro-isostasy: the implementation of a revised sea-level equation. *Geophysical Journal International*, **139**(2), pp.464-482.

Moldwin, M., 2008. *An introduction to space weather*. Cambridge University Press.

Naeimi, M.; Flury, J. Global Gravity Field Modeling from Satellite-to-Satellite Tracking Data. In Lecture Notes in Earth System Sciences; Springer: Berlin, Germany, 2017.

Nakanishi, K., Iyemori, T., Taira, K. and Lühr, H., 2014. Global and frequent appearance of small spatial scale field-aligned currents possibly driven by the lower atmospheric phenomena as observed by the CHAMP satellite in middle and low latitudes. *Earth, Planets and Space*, **66**(1), p.40.

Nishijima, Y. and Oster, G., 1964. Moiré patterns: their application to refractive index and refractive index gradient measurements. *JOSA*, *54*(1), pp.1-5.

Pagiatakis, S., 1999. Stochastic significance of peaks in the least-squares spectrum. *Journal of Geodesy*, 73(2):67–78.

Pail, R., 2018. Mass variation observing system by high-low inter-satellite links (MOBILE)—A mission proposal for ESA Earth Explorer 10. EGU, EGU2018-1972.

Pail, R., Bruinsma, S., Migliaccio, F., Förste, C., Goiginger, H., Schuh, W.D., Höck, E., Reguzzoni, M., Brockmann, J.M., Abrikosov, O. and Veicherts, M., 2011. First GOCE gravity field models derived by three different approaches. *Journal of Geodesy*, **85**(11), p.819.

Panet, I., Pajot-Métivier, G., Greff-Lefftz, M., Métivier, L., Diament, M., and Mandea, M., 2014. Mapping the mass distribution of Earth’s mantle using satellite-derived gravity gradients. *Nature Geoscience*, **7**(2), 131.

Patorski, K., Pokorski, K., and Trusiak, M., 2011. Fourier domain interpretation of real and pseudo-moiré phenomena. *Optics Express*, *19*(27), pp.26065-26078.

Peidou, A.C., Fotopoulos, G., and Pagiatakis, S., 2018. On the feasibility of using satellite gravity observations for detecting large-scale solid mass transfer events. *Journal of Geodesy,* **92**(5), pp.517-528.

Peidou, A. and Pagiatakis, S., 2019. Gravity Gradiometry with GRACE Space Missions: New opportunities for the Geosciences. *Journal of Geophysical Research: Solid Earth*, **124**(8), pp.9130-9147.

Peidou, A. and Pagiatakis, S., 2020. Stripe mystery in GRACE geopotential models revealed. *Geophysical Research Letters*, doi:10.1029/2019GL085497.

Petit, G. and Luzum, B., 2010. *IERS conventions (2010)* (No. IERS-TN-36). BUREAU INTERNATIONAL DES POIDS ET MESURES SEVRES (FRANCE).

Reigber, C., Lühr, H. and Schwintzer, P., 2002. CHAMP mission status. *Advances in space research*, **30**(2), pp.129-134.

Reigber, C., Lühr, H., Schwintzer, P. and Wickert, J., 2004. Earth Observation with CHAMP. *Results from Three Years*.

Richardson, J.D. and Paularena, K.I., 1998. The orientation of plasma structure in the solar wind. *Geophysical research letters*, **25**(12), pp.2097-2100.

Rodell, M., Velicogna, I. and Famiglietti, J.S., 2009. Satellite-based estimates of groundwater depletion in India. *Nature*, **460**(7258), p.999.

Rostoker, G., 1972. Geomagnetic indices. *Reviews of Geophysics*, **10**(4), pp.935-950.

Rummel, R., 2003. How to climb the gravity wall. *Space Science Reviews*, **108**(1-2), pp.1-14.

Rummel, R., Balmino, G., Johannessen, J., Visser, P. N. A. M., and Woodworth, P., 2002. Dedicated gravity field missions—principles and aims. *Journal of Geodynamics*, **33**(1-2).

Rummel, R., Yi, W., and Stummer, C., 2011. GOCE gravitational gradiometry. *Journal of Geodesy*, **85**(11), 777.

Ruppert, M.G., Harcombe, D.M., Ragazzon, M.R., Moheimani, S.R. and Fleming, A.J., 2017. A review of demodulation techniques for amplitude-modulation atomic force microscopy. *Beilstein journal of nanotechnology*, **8**(1), pp.1407-1426.

Sasgen, I., Klemann, V. *and* Martinec, Z., 2012. Towards the inversion of GRACE gravity fields for present-day ice-mass changes and glacial-isostatic adjustment in North America and Greenland. *Journal of Geodynamics*, **59**, *pp.*49–63.

Save, H., Bettadpur, S. and Tapley, B.D., 2016. High-resolution CSR GRACE RL05 mascons. *Journal of Geophysical Research: Solid Earth*, **121**(10), pp.7547-7569.

Schelkle, M., 2000, December. The GRACE cold gas attitude and orbit control system. In *Spacecraft Propulsion* (Vol. **465**, p. 769).

Seo, K.W., Wilson, C.R., Chen, J. and Waliser, D.E., 2008. GRACE's spatial aliasing error. Geophysical Journal International, **172**(1), pp.41-48.

Seo, K.W., Wilson, C.R., Han, S.C. and Waliser, D.E., 2008. Gravity Recovery and Climate Experiment (GRACE) alias error from ocean tides. *Journal of Geophysical Research: Solid Earth*, **113**(B3).

Sheard, B.S., Heinzel, G., Danzmann, K., Shaddock, D.A., Klipstein, W.M. and Folkner, W.M., 2012. Intersatellite laser ranging instrument for the GRACE follow-on mission. *Journal of Geodesy*, **86**(12), pp.1083-1095.

Sneeuw, N., Sharifi, M.A. and Keller, W., 2008. Gravity recovery from formation flight missions. In VI Hotine-Marussi Symposium on theoretical and computational geodesy (pp. 29-34). Springer, Berlin, Heidelberg.

Stone E, Frandsen A, Mewaldt R, Christian E, Margolies D, Ormes J and Snow F., 1998. The advanced composition explorer. The Advanced Composition Explorer Mission. Springer, 1–22.

Stummer, C., Siemes, C., Pail, R., Frommknecht, B., and Floberghagen, R., 2012. Upgrade of the GOCE Level 1B gradiometer processor. *Advances in Space Research*, **49**(4), 739-752.

Swarm Level 2 Processing Facility, 2018. Validation of Swarm Level 2 Product. Doc. no: SW-DS-BGS-GS-0051.

Swenson, S. and Wahr, J., 2006. Post-processing removal of correlated errors in GRACE data. *Geophysical Research Letters*, **33**(8).

Tapley, B. D., Bettadpur, S., Ries, J. C., Thompson, P. F., and Watkins, M. M., 2004. GRACE measurements of mass variability in the Earth system. *Science*, **305**(5683), 503-505.

Tapley, B.D., Ries, J., Bettadpur, S., Chambers, D., Cheng, M., Condi, F., Poole, S., 2007. The GGM03 Mean Earth Gravity Model from GRACE; Eos Trans, Vol AGU 88(52), Fall Meet. Suppl., Abstract G42A-03.

Theocaris, P.S., 1969. Moiré fringes in strain analysis (pp. 233-278). Oxford: Pergamon press.

Thompson, P.F., Bettadpur, S.V. and Tapley, B.D., 2004. Impact of short period, non-tidal, temporal mass variability on GRACE gravity estimates. Geophysical research letters, **31**(6).

Touboul, P., Foulon, B., Rodrigues, M., and Marque, J. P., 2004. In orbit nano-g measurements, lessons for future space missions. *Aerospace Science and Technology*, **8**(5), 431-441.

Touboul, P., Willemenot, E., Foulon, B. and Josselin, V., 1999. Accelerometers for CHAMP, GRACE and GOCE space missions: synergy and evolution. Boll. Geof. Teor. Appl, **40**(3-4), pp.321-327.

Tregoning, P., Watson, C., Ramillien, G., McQueen, H. and Zhang, J., 2009. Detecting hydrologic deformation using GRACE and GPS. *Geophysical Research Letters*, **36**(15).

Vaníček, P., 1969. Approximate spectral analysis by least-squares fit. *Astrophysics and Space Science*, **4**(4), pp.387-391.

Velicogna, I. and Wahr, J., 2005. Greenland mass balance from GRACE. *Geophysical Research Letters*, **32**(18).

Velicogna, I., Wahr, J. and Van den Dool, H., 2001. Can surface pressure be used to remove atmospheric contributions from GRACE data with sufficient accuracy to recover hydrological signals?. *Journal of Geophysical Research: Solid Earth*, **106**(B8), pp.16415-16434.

Vishwakarma, B., Devaraju, B. and Sneeuw, N., 2018. What Is the Spatial Resolution of grace Satellite Products for Hydrology?. *Remote Sensing*, **10**(6), p.852.

Wagner, C., McAdoo, D., Klokočník, J. and Kostelecký, J., 2006. Degradation of geopotential recovery from short repeat-cycle orbits: application to GRACE monthly fields. *Journal of Geodesy*, **80**(2), pp.94-103.

Wang, L., Davis, J.L., Hill, E.M. and Tamisiea, M.E., 2016. Stochastic filtering for determining gravity variations for decade-long time series of GRACE gravity. *Journal of Geophysical Research: Solid Earth*, **121**(4), pp.2915-2931.

Watkins, M.M., Wiese, D.N., Yuan, D.N., Boening, C. and Landerer, F.W., 2015. Improved methods for observing Earth's time variable mass distribution with GRACE using spherical cap mascons. *Journal of Geophysical Research: Solid Earth*, **120**(4), pp.2648-2671.

Weigelt, M., Sideris, M.G. and Sneeuw, N., 2009. On the influence of the ground track on the gravity field recovery from high–low satellite-to-satellite tracking missions: CHAMP monthly gravity field recovery using the energy balance approach revisited. *Journal of Geodesy*, *83*(12), pp.1131-1143.

Weygand, J.M., Amm, O., Viljanen, A., Angelopoulos, V., Murr, D., Engebretson, M.J., Gleisner, H. and Mann, I., 2011. Application and validation of the spherical elementary currents systems technique for deriving ionospheric equivalent currents with the North American and Greenland ground magnetometer arrays. *Journal of Geophysical Research: Space Physics*, **116**(A3).

Wen, H.Y., Kruizinga, G., Meegyeong, P., Landerer, F., Bertinger, W. and Sakumura, C., 2018. Gravity Recovery and Climate Experiment (GRACE) Follow-On (GRACE-FO) Level-1 Data Product User Handbook.

Wiese, D.N., 2011. Optimizing two pairs of GRACE-like satellites for recovering temporal gravity variations (Doctoral dissertation). Retrieved from University of Colorado at Boulder (https://scholar.colorado.edu/asen_gradetds/28/).

Williams, G.L., 2000. Sub-Nyquist Sampling and Moire-Like Waveform Distortions. 47th International Instrumentation Symposium, Denver, CO, USA, 20020027355.

Wouters, B. and Schrama, E.J.O., 2007. Improved accuracy of GRACE gravity solutions through empirical orthogonal function filtering of spherical harmonics. *Geophysical Research Letters*, **34**(23).

Yermolaev, Y.I., Zelenyi, L.M., Kuznetsov, V.D., Chertok, I.M., Panasyuk, M.I., Myagkova, I.N., Zhitnik, I.A., Kuzin, S.V., Eselevich, V.G., Bogod, V.M. and Arkhangelskaja, I.V., 2008. Magnetic storm of November, 2004: Solar, interplanetary, and magnetospheric disturbances. *Journal of Atmospheric and Solar-Terrestrial Physics*, **70**(2), pp.334-341.

Zenner, L., Gruber, T., Jäggi, A. and Beutler, G., 2010. Propagation of atmospheric model errors to gravity potential harmonics impact on GRACE de-aliasing. *Geophysical Journal International*, **182**(2), pp.797-807.

Zhang, S. P., Goncharenko, L. P., Salah, J. E., Roble, R. G., and Shepherd, G. G., 2003. Climatology of neutral winds in the lower thermosphere over Millstone Hill (42.6 N) observed from ground and from space. *Journal of Geophysical Research: Space Physics*, **108**(A1).

Appendix I

The Advanced Composition Explorer (ACE) was launched in August, 1997 (Stone et al., 1998) and designed to observe energetic particles coming from the Sun and other sources. ACE data have been used to improve solar storm forecasting and warning. Communication with ACE satellite which is located at about 1.5 million km away from the Earth is performed via microwave (S-band). Its location is about 148.5 million km from the Sun.

In this research, we use interplanetary magnetic and electric fields as well as plasma flow velocity that are retrieved from different measurements measured by different sensors on-board ACE.

ACE provides observations of the magnetic field on Geocentric Solar Ecliptic (GSE) and on Geocentric Solar Magnetospheric (GSM) reference systems. The ACE observations are referred on the L1 Lagrange point and are reduced to the bow-shock nose (Hapgood, 1992). GSE serves as reference system for various space applications and is defined as follows:

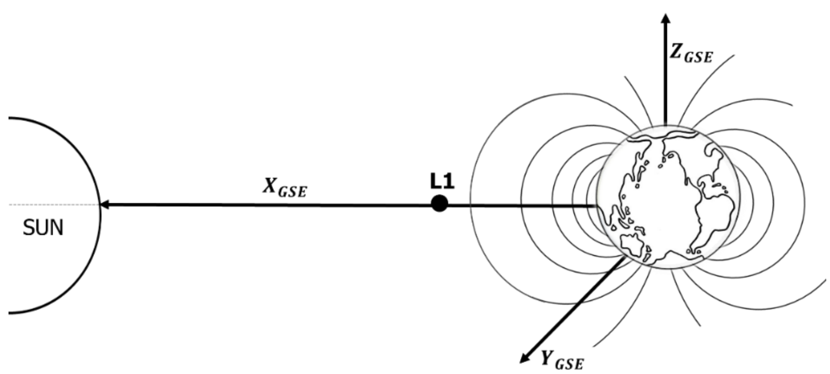

L1 Lagrange Point and other Lagrange Points. B_x, B_y, and B_z shows the Interplanetary Magnetic Field Component directions in the GSE Coordinate System.

In order to correlate ACE magnetic field's observations to GRACE accelerometer observations the two datasets should be referred on the same reference system. Thus, transformations between the two systems are applied. The two systems are not connected directly emerging the need to use intermediate steps. The following figure displays the succeeding steps of the transformation process. It is worth mentioning that we are more interested in the features and variations of the signals (e.g., electric field, plasma flow velocity) rather than their exact magnitude at the satellite positions. Accordingly, we do not need to worry about the distance and attenuation of the signal from the measured point (or the bowshock nose) to the Earth's surface, which is a very complex transformation process.

The first transformation takes place between GSE and an Earth Fixed Reference Frame (EFRF).

A detailed description regarding the transformation of the two datasets follows:

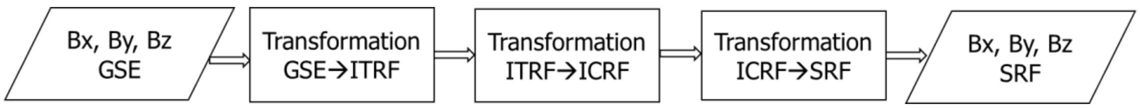

From GSE to ITRF

There are two transformations involved between the GSE and EFRF (e.g., International Terrestrial Reference Frame). It is worth mentioning that the International Terrestrial Reference Frame (ITRF) is commonly mentioned as Earth Fixed Reference Frame in the recent publications. The first rotation is in the plane of the Earth's geographic equator from the first point of Aries (Vernal Equinox) to Greenwich. The second one is the rotation from the Earth's Equator to the plane of the ecliptic and rotation in the place of the ecliptic from vernal equinox to the Earth-Sun direction (Hapgood, 1992). The transformation steps can be described as follows:

GSE-ITRF Transformation steps

$$T_1 = R_3(\theta), \quad (1)$$

$$T_2 = R_3(\lambda_s)R_1(\varepsilon), \quad (2)$$

where R_1 and R_3 are the rotation matrices of X and Z axis, respectively and

$$\theta = 100.461^o + 3600.77^o T_o + 15.04107^o UT, \quad (3)$$

$$\lambda_s = \lambda + (1.915 - 0.0048T_o)\sin(M) + 0.02\sin(2M), \quad (4)$$

$$\lambda = 280.460 + 36000.772^o T_o + 0.04107^o UT, \quad (5)$$

where M, ε and T_o are given as follows

$$T_o = \frac{MJD - 515544.5}{36525}, \quad (6)$$

$$\varepsilon = 23.439 - 0.013\mathrm{T_o}, \tag{7}$$

$$\mathrm{M} = 357.52^{\mathrm{o}} + 35999.05\mathrm{T_o} + 0.04107\mathrm{UT}, \tag{8}$$

with UT being the Universal Time and MJD the Modified Julian Date.

Finally, the transformation takes place as:

$$\begin{bmatrix} \mathrm{X_{ITRF}} \\ \mathrm{Y_{ITRF}} \\ \mathrm{Z_{ITRF}} \end{bmatrix} = \mathrm{T_1 T_2} \begin{bmatrix} \mathrm{X_{GSE}} \\ \mathrm{Y_{GSE}} \\ \mathrm{Z_{GSE}} \end{bmatrix}. \tag{9}$$

From ITRF to ICRF

The ITRF to ICRF transformation is realized as:

$$\overline{\mathrm{R}}(\mathrm{t}) = \mathrm{P(t)N(t)}, \tag{10}$$

$$\hat{R}(\mathrm{t}) = \mathrm{R_3(-GAST)}, \tag{11}$$

$$\breve{\mathrm{R}}(\mathrm{t}) = \mathrm{R_1}(\mathrm{y_p})\mathrm{R_2}(\mathrm{x}_p), \tag{12}$$

Where P and N are given as:

$$\mathrm{P(t)} = \mathrm{R_3}(\zeta)\mathrm{R_2}(-\theta)\mathrm{R_3}(\mathrm{z}), \tag{13}$$

$$\mathrm{N(t)} = \mathrm{R_1}(-\varepsilon)\mathrm{R_3}(\Delta\psi)\mathrm{R_1}(\varepsilon + \Delta\varepsilon), \tag{14}$$

with

$$\zeta = 2306''.2181\mathrm{t} + 0''.30188\mathrm{t}^2 + 0''.017988\mathrm{t}^3, \tag{15}$$

$$\mathrm{z} = 2306''.2181\mathrm{t} + 1''.09468\mathrm{t}^2 + 0''.018203\mathrm{t}^3, \tag{16}$$

$$\theta = 2004''.3109\mathrm{t} - 0''.42665\mathrm{t}^2 - 0''.0041833\mathrm{t}^3, \tag{17}$$

$$\Delta\psi = -17''.1996\sin(\Omega) + 0''.2062\sin(2\Omega) - 1''.3187\sin(2F - 2D + 2\Omega) + \cdots + d\psi, \quad (18)$$

$$\Delta\varepsilon = 9''.2025\cos(\Omega) - 0''.0895\cos(2\Omega) + 0''.5736\cos(2F - 2D + 2\Omega) + \cdots + d\varepsilon, \quad (19)$$

$$\varepsilon = 84381''.448 - 46''.815t - 0''.00059t^2 - 0''.001833t^3, \quad (20)$$

where t is the time to J2000.0 expressed in Julian centuries of 36525 days. Terms F, D and Ω are used for Nutation periods.

$$F = 93^o.27209062 + 17395277262''.8478t - 12''.7512t^2 - 0''.001037t^3, \quad (21)$$

$$D = 297^o.85019547 + 1602961601''.209t - 6''.3706t^2 + 0''.006593t^3, \quad (22)$$

$$\Omega = 125^o.04455501 - 6962890''.26665t + 7''.4722t^2 + 0''.007702t^3. \quad (23)$$

The Greenwich apparent sidereal time (GAST) is estimated as follows:

$$\mathrm{GMST}_{0^h\mathrm{UT1}} = 6^h41^m50.54841 + 8640184^s.812866T_U + 0.093104T_U^2 - 6^s.2 \times 10^{-6}T_U^3, \quad (24)$$

$$\mathrm{GMST} = \mathrm{GMST}_{0^h\mathrm{UT1}} + r\big((\mathrm{UT1} - \mathrm{UTC}) + \mathrm{UTC}\big), \quad (25)$$

$$r = 1.002737909350795 + 5.9006 \times 10^{-11}T_U - 5.9 \times 10^{-15}T_U^2, \quad (26)$$

$$\mathrm{GAST} = \mathrm{GMST} + \Delta\psi\cos\varepsilon + 0''.00264\sin(\Omega) + 0''.000063\sin(2\Omega), \quad (27)$$

where

$$T_U = \frac{d_u}{36525}, \quad (28)$$

and d_u denotes the number of day elapses since January first 2000, 12^hUT1.

Finally, the ICRF coordinates are given as:

$$\begin{bmatrix} X_{ICRF} \\ Y_{ICRF} \\ Z_{ICRF} \end{bmatrix} = \overline{R}(t)\widehat{R}(t)\breve{R}(t) \begin{bmatrix} X_{ITRF} \\ Y_{ITRF} \\ Z_{ITRF} \end{bmatrix} \quad (29)$$

From ICRF to SRF

$$\begin{bmatrix} X_{SRF} \\ Y_{SRF} \\ Z_{SRF} \end{bmatrix} = \begin{bmatrix} q_o^2 + q_1^2 - q_2^2 - q_3^2 & 2q_1q_2 - 2q_0q_3 & 2q_1q_3 + 2q_0q_2 \\ 2q_1q_2 + 2q_0q_3 & q_o^2 - q_1^2 + q_2^2 - q_3^2 & 2q_2q_3 - 2q_0q_1 \\ 2q_1q_3 - 2q_0q_2 & 2q_2q_3 + 2q_0q_1 & q_o^2 - q_1^2 - q_2^2 + q_3^2 \end{bmatrix} \begin{bmatrix} X_{ICRF} \\ Y_{ICRF} \\ Z_{ICRF} \end{bmatrix}, \qquad (30)$$

where q_0, q_1, q_2, q_3 are the quaternions provided in the SCA1B data files.